



저작자표시-비영리-변경금지 2.0 대한민국

이용자는 아래의 조건을 따르는 경우에 한하여 자유롭게

- 이 저작물을 복제, 배포, 전송, 전시, 공연 및 방송할 수 있습니다.

다음과 같은 조건을 따라야 합니다:



저작자표시. 귀하는 원저작자를 표시하여야 합니다.



비영리. 귀하는 이 저작물을 영리 목적으로 이용할 수 없습니다.



변경금지. 귀하는 이 저작물을 개작, 변형 또는 가공할 수 없습니다.

- 귀하는, 이 저작물의 재이용이나 배포의 경우, 이 저작물에 적용된 이용허락조건을 명확하게 나타내어야 합니다.
- 저작권자로부터 별도의 허가를 받으면 이러한 조건들은 적용되지 않습니다.

저작권법에 따른 이용자의 권리는 위의 내용에 의하여 영향을 받지 않습니다.

이것은 [이용허락규약\(Legal Code\)](#)을 이해하기 쉽게 요약한 것입니다.

[Disclaimer](#)

Multiscale and Hybrid Manufacturing Processes
Using a Large Pulsed Electron Beam Irradiation
on Engineering Materials

Jisoo Kim

Department of Mechanical Engineering

Graduate School of UNIST

Multiscale and Hybrid Manufacturing Processes
Using a Large Pulsed Electron Beam Irradiation
on Engineering Materials

A thesis/dissertation
submitted to the Graduate School of UNIST
in partial fulfillment of the
requirements for the degree of
Doctor of Engineering

Jisoo Kim

08/10/2018

Approved by



Advisor

Hyung Wook Park

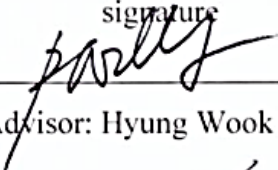
Multiscale and Hybrid Manufacturing Processes Using a Large Pulsed Electron Beam Irradiation on Engineering Materials

Jisoo Kim

This certifies that the thesis/dissertation of Jisoo Kim is approved.

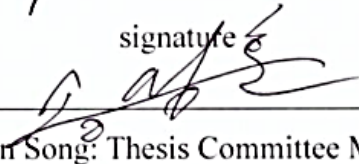
08/10/2018

signature



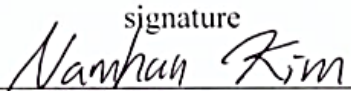
Advisor: Hyung Wook Park

signature



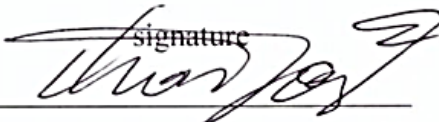
Myoung Hoon Song: Thesis Committee Member #1

signature



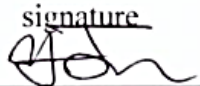
Namhun Kim: Thesis Committee Member #2

signature



Hae-Jin Choi: Thesis Committee Member #3

signature



Yongho Jeon: Thesis Committee Member #4;

three signatures total in case of masters

Abstract

Surface qualities including topography, texture, mechanical, and chemical stabilities have become an essential requirement in manufacturing along with a new paradigm of industrial revolution. The electron beam irradiation is a special technique for surface modification. Especially, the energy transfer through electrons with rapid thermal gradient inducing phase transformation and re-solidification of materials is the unique characteristics of large pulsed electron beam (LPEB) irradiation, which makes it a potential candidate for surface manufacturing. Despite the previous studies have revealed that the LPEB irradiation could reduce surface roughness and modify surface properties, the application of LPEB in manufacturing processes is rather limited as the mechanisms of LPEB irradiation and corresponding surface modifications are yet to be explored. In order to expand the application area of the LPEB irradiation, the dissertation aims at (1) predictive modeling of the LPEB irradiation to firmly establish the irradiating mechanisms, (2) fundamental understandings on surface modification factors specifying the modification mechanisms, and (3) applying the LPEB irradiation for multiscale and hybrid manufacturing processes based on the modification mechanisms.

The first part of the dissertation will be temperature prediction using a numerical model during the LPEB process. The absorptance of electron beam was estimated considering electron scattering, backscattering, and transmission to adopt the natural interactions of electrons with substrates. The model predicts temperature distributions and molten depths depending on the irradiation conditions. The effects of considerations of absorptance containing natural interactions such as scattering, backscattering, and transmission on prediction accuracy were explored by comparing the predictive results between constant and calculated absorptance versus depth. The estimation of absorptance and energy transfer mechanisms resulted in more accurate predictions of molten depths.

The experimental investigations of LPEB irradiation were mainly performed on mold steels (KP1 and KP4) and biomedical alloys (Ti-6Al-7Nb) in the second part. The nano-hardness of mold steels increased by 316% (KP1), 144% (KP4), and 154% (Ti-6Al-7Nb), respectively under optimized experimental parameters, which is affected by the increased dislocations in the re-solidified layer and a decreased fraction of the pre-dominant slip plane. Contact angle variations and oxides formation in the re-solidified layer projected that the surface became stable. Corrosion resistance of the irradiated surface was increased, as evidenced from the improved corrosion parameters. Based on the mechanisms of surface hardening, the nitriding process of Ti-6Al-7Nb using the LPEB irradiation was also explored. The atomic concentration of nitrogen atoms at the re-solidified layer could be achieved up to ~18% by LPEB nitriding. Nano-hardness in the re-solidified layer was improved further by ~75% following the LPEB nitriding process, as a result of the formation of TiN. The nitrided layer induced by the LPEB nitriding, consisted of TiN, TiO₂, and TiO_xN_y, which modified the corrosion resistance as evidenced from the improved electrochemical parameters. An increase in the fraction of TiN at the re-solidified

layer was considered responsible for the remarkable improvement of surface properties embedding uniformly noble and stable characteristics at the top surface.

Based on the fundamental mechanisms of LPEB irradiations specified in the first and second parts, multiscale and hybrid manufacturing processes using the LPEB will be discussed in the last part.

The patterned metal masks fabricated by a laser and drilled CFRP composites were selected as a microscale application of the LPEB irradiation as a deburring process based on the melting mechanism. The generated burrs were tried to be eliminated by a LPEB-assisted hybrid deburring process on metal masks. The size of burrs after the process was decreased about 81% from 38.01 μm to 7.2 μm comparing to the results of abrasive deburring alone. The distribution of burr size also decreased about 85% and surface roughness (R_a) was modified from 640 nm to 121 nm, indicating the formation of a uniform surface texture. The optimized irradiation also improved the accuracy of the shapes of the holes, and reduced the sizes of the burrs by 97% on drilled CFRP composites. This modified the deviations of hole accuracy by 93%. The unique deburring mechanisms started with evaporation of the resin that coats the carbon fibers was revealed through experimental observations.

Moreover, superhydrophobic transformation of patterned metal surfaces was also investigated as one of the microscale applications of LPEB based on the surface modification. The Wenzel-to-Cassie transition occurred at 140° with a groove depth of 250 μm after the WEDM fabrication which indicated the development of a hydrophobic surface. However, the contact angle increased to 166.7° with the Cassie state after the LPEB irradiation at a lower depth of groove (200 μm). The modification of surface roughness following the LPEB irradiation on the patterns resulted in a decreased the critical angle for Wenzel-to-Cassie transition. FT-IR spectroscopy acquired at the ATR mode specified the elimination of hydrophilic functional groups on the surface following LPEB irradiation.

Finally, silver nanowires (AgNWs) were selected as a nanoscale application of LPEB irradiation based on the energy transfer mechanism. The welding of silver nanowires to form percolation networks using the LPEB irradiation was investigated. The welded AgNWs showed modified electrical and mechanical characteristics with a low contact resistance at junctions. Therefore, the LPEB-welded AgNW electrode exhibited modified sheet resistance of 12.63 Ω/sq and higher transmittance of 93% (at 550 nm). Furthermore, the outstanding mechanical flexibility was obtained than other AgNW electrodes prepared by thermal annealing. The feasibility of LPEB-welded AgNW electrodes were proved by the fabrication of polymer light-emitting diodes (PLEDs). The result supported that the LPEB-welded AgNWs could become an alternative to indium tin oxide (ITO).

The dissertation will explore a comprehensive approach on the LPEB irradiation encompassing materials selection, understanding of the underlying multi-physical phenomena, surface modification mechanisms, surface qualities, and applications of LPEB irradiation for multiscale and hybrid manufacturing processes. This unique research approach will overcome the limitations of conventional finishing processes, incorporate subdivided finishing processes into a single step, and bring a new

paradigm of finishing systems. It should be anticipated that the outcome of the dissertation will expand the application areas of the LPEB irradiation in the overall manufacturing industries including automotive, aerospace, biomedical, and semi-conductors in multiscale from macro- to nano-levels.

Contents

CONTENTS	v
LIST OF FIGURES	vii
LIST OF TABLES	xi
NOMENCLATURE	xii
1. INTRODUCTION	1
1.1 Research objectives	2
1.2 Research outline	3
2. LITERATURE REVIEW	5
2.1 Conventional surface finishing and treatment processes	5
2.2 Surface modification processes using an electron beam irradiation	8
2.3 Theoretical backgrounds on an electron beam irradiation	9
3. PREDICTIVE MODEL OF THE LARGE PULSED ELECTRON BEAM (LPEB) IRRADIATION	11
3.1 Interactions between electrons and substrates	11
3.2 Absorptance of the electrons	14
3.3 Temperature predictive model of the LPEB irradiation	15
3.4 Prediction of molten depths and experimental validations	20
4. FUNDAMENTAL UNDERSTANDINGS ON THE EFFECTS INDUCED BY LPEB IRRADIATIONS	25
4.1 Surface modification of engineering alloys – Macroscale applications	25
4.1.1 Design of experiments and materials	25
4.1.2 Formation of the re-solidified layer	26
4.1.3 Mechanical properties	28
4.1.4 Chemical properties	31
4.1.5 Microstructure	38
4.2 Surface modification of biomedical alloys	41
4.2.1 Formation of the re-solidified layer	42

4.2.2 Mechanical properties	44
4.2.3 Chemical properties	44
4.2.4 Microstructure	49
4.3 Nitriding process assisted by the LPEB irradiation	51
4.3.1 Design of experiments and materials	51
4.3.2 Microstructure and chemical components	52
4.3.3 Mechanical properties	60
4.3.4 Chemical properties	61
4.4 Summary	64
5. APPLICATIONS OF LPEB IRRADIATIONS ON MANUFACTURING PROCESSES	66
5.1 LPEB manufacturing based on melting mechanisms	66
5.1.1 LPEB deburring process on stainless steels	66
5.1.2 LPEB deburring process on CFRP composites	73
5.2 LPEB manufacturing based on surface modification mechanisms	84
5.2.1 Superhydrophobic transformation of metallic patterns	84
5.3 LPEB manufacturing based on charge transfer mechanisms	94
5.3.1 Design of experiments and materials	94
5.3.2 Nanostructures of welded AgNWs	96
5.3.3 Electrical properties of welded AgNWs	99
5.3.4 Performance of welded AgNWs	106
6. CONCLUSIONS AND RECOMMENDATIONS	108
6.1 Conclusions	108
6.2 Recommendations	110
REFERENCES	113
ACKNOWLEDGEMENT	124

LIST OF FIGURES

Figure 1. Research outline

Figure 2. Optical images on the surfaces before and after the LPEB irradiation on (a) carbon steels and (b, c) mold steels [51]

Figure 3. Backscattering coefficients of materials as a function of incident energies

Figure 4. Total transmission of the accelerated electrons of different materials at different depths when irradiated with incident energies of (a) 25 keV and (b) 30 keV

Figure 5. Schematic diagram of the energy transfer from the LPEB to the substrate, illustrating backscattering, transmission, and energy absorption

Figure 6. Fractional absorptance of the LPEB as a function of depth for different materials at incident energies of (a) 25 keV and (b) 30 keV

Figure 7. Gaussian-distributed beam intensity

Figure 8. 3D temperature distributions and cross-sectional analyses of molten depth as a function of incident energy and material

Figure 9. Schematic diagram of the experimental set-ups for the LPEB irradiation

Figure 10. Cross-sectional SEM images indicating molten depth of the investigated materials as a function of energy density

Figure 11. Comparisons of predicted and experimentally measured molten depths of different materials obtained at incident energies of (a) 25 keV and (b) 30 keV

Figure 12. Cross-sectional SEM images of KP1 and KP4 samples before and after the LPEB irradiation

Figure 13. Surface roughness as a function of the number of LPEB irradiation cycles

Figure 14. Electron probe micro-analysis on a cross-sectional area of the samples containing manganese sulfide inclusions

Figure 15. Crater densities generated on the surface of KP1 and KP4 after the LPEB irradiation

Figure 16. Nano-hardness and elastic modulus as a function of depth on the LPEB-irradiated KP1 and KP4 samples

Figure 17. Normalized weight loss following pin-on-disc wear tests on the LPEB-irradiation KP1 and KP4 samples

Figure 18. 3D surface profiles and optical microscopy images of the wear tracks formed on (a and b) untreated KP1, (c and d) LPEB-treated KP1, (e and f) untreated KP4, and (g and h) LPEB-treated KP4

Figure 19. Potentiodynamic polarization curves of the LPEB-treated surface on (a) KP1 and (b) KP4

Figure 20. Contact angle before and after the LPEB irradiation on both the KP1 and KP4 samples with an energy density of (a) 7 J/cm² and (b) 10 J/cm²

Figure 21. EPMA results showing the distribution of oxygen on the cross-sectional area of (a) KP1 and (b) KP4 following the LPEB irradiation

Figure 22. Nyquist plots for (a) KP1 and (b) KP4 before and after the LPEB irradiation

Figure 23. Optical micrographs of the corrosion-damaged surface morphology of the bare and LPEB-treated surfaces

Figure 24. Illustration of the corrosion mechanism on the surface: (a) untreated, (b) following the LPEB irradiation, and (c) progressive pitting corrosion around the crater on the LPEB-irradiated surface

Figure 25. IQMs from the EBSD analysis on the cross-sectional area: (a) untreated KP1, (b) LPEB-treated KP1, (c) untreated KP4, and (d) LPEB-treated KP4

Figure 26. XRD patterns obtained from the surface of mold steels before and after the LPEB irradiation

Figure 27. Optical photographs showing the surface texture of Ti-6Al-7Nb before (left) and after (right) the LPEB irradiation

Figure 28. Cross-sectional SEM images of the Ti-6Al-7Nb after the LPEB irradiation at (a) 7 J/cm² for 5 pulses, (b) 7 J/cm² for 10 pulses, (c) 10 J/cm² for 5 pulses, and (d) 10 J/cm² for 10 pulses

Figure 29. Nano-hardness as a function of depth for the LPEB-treated Ti-6Al-7Nb samples

Figure 30. Potentiodynamic polarization curves of the LPEB-irradiated Ti-6Al-7Nb

Figure 31. EPMA representing the distribution of chemical components on the cross-sectional area of Ti-6Al-7Nb following the LPEB irradiation with (a) 7 J/cm² and (b) 10 J/cm²

Figure 32. XPS spectra of untreated and LPEB-treated Ti-6Al-7Nb for (a) titanium and (b) aluminum

Figure 33. (a) Nyquist plots and (b) $\log(f)-|Z|$ plots of Ti-6Al-7Nb before and after the LPEB irradiation

Figure 34. Cross-sectional SEM images showing twinning traces induced by the LPEB irradiation with an energy density of (a) 7 J/cm² and (b) 10 J/cm²

Figure 35. XRD patterns obtained from Ti-6Al-7Nb before and after the LPEB irradiation

Figure 36. Schematic diagram of the experimental set-up for the LPEB nitriding

Figure 37. SEM images on Ti-6Al-7Nb surfaces (a) before and after LPEB irradiations with (b) 0 V-biased in Ar gas, (c) 0 V-biased in N₂ gas, and (d) -100 V-biased in N₂ gas

Figure 38. White-interference micrographs on the surface of Ti-6Al-7Nb after the LPEB irradiations

Figure 39. A SEM image and EDS result near the crater-generated region corresponding to FIGURE

Figure 40. Cross-sectional SEM images of LPEB-irradiated Ti-6Al-7Nb with (a) Ar plasma gas and (b) N₂ plasma gas

Figure 41. Atomic concentration of nitrogen after the LPEB irradiation in terms of the (a) negative DC bias and (b) number of pulses

Figure 42. (a) Schematic diagram of nitrided layers and (b) cross-sectional SEM images following plasma, gas, and solid nitriding processes

Figure 43. Cross-sectional SEM images after the plasma nitriding process on mold steels at two randomly selected regions

Figure 44. XPS spectra of Ti-6Al-7Nb after the LPEB nitriding with the negative DC bias

Figure 45. Variations in nano-hardness at re-solidified layer as a function of depth

Figure 46. (a) Potentiodynamic polarization curves of LPEB-irradiated Ti-6Al-7Nb and (b) corresponding corrosion parameters

Figure 47. Chronoamperometry of Ti-6Al-7Nb before and after the LPEB irradiation

Figure 48. Illustration of a patterned metal mask

Figure 49. Schematic diagrams of (a) abrasive deburring and (b) LPEB irradiation

Figure 50. SEM images of the surface of patterned metal masks after fiber laser cutting

Figure 51. SEM images of the surface of patterned metal masks after abrasive deburring

Figure 52. SEM images of the surface of patterned metal masks after the LPEB deburring

Figure 53. Variation in predicted molten depth as a function of acceleration voltage and corresponding experimental results

Figure 54. SEM images of a generated burr after fiber laser cutting viewed from (a) above and (b) side

Figure 55. Schematic diagram of the LPEB-assisted hybrid deburring process

Figure 56. SEM images of the surface of patterned metal masks after the LPEB-assisted hybrid deburring

Figure 57. Scatter of the burr size generated and remaining after the fiber laser cutting and deburring processes

Figure 58. Schematic diagram of the experimental setups for the large pulsed electron beam irradiations

Figure 59. Optical images of the generated burrs after the drilling process on CFRP composites

Figure 60. Variations of the burr sizes before and after the LPEB irradiations in terms of (a) acceleration voltage, (b) the number of pulses, and (c) solenoid voltage

Figure 61. Schematic diagram and mechanisms of the deburring process for drilled CFRP composites using the large pulsed electron beam irradiations

Figure 62. Optical images of the generated and remaining burrs on CFRP composites after the LPEB irradiations in terms of V_a , V_s , and the number of pulses (N)

Figure 63. Representative 3D scanned geometrical features and diameter deviations of the drilled CFRP holes before and after the LPEB irradiations

Figure 64. The diameter deviations of the drilled CFRP holes comparing to the ideal circle before and after the LPEB irradiations in terms of (a) acceleration voltage, (b) the number of pulses, and (c) solenoid voltage

Figure 65. Schematic diagram of wire electric-discharge machining (WEDM) and variables corresponding to pattern structures

Figure 66. Cross-sectional optical microscopy images of WEDM-fabricated patterns before and after large pulsed electron beam (LPEB) irradiation

Figure 67. Measured (a) groove depth, d and (b) land width of WEDM-fabricated patterns before and after LPEB irradiation as a function of tool path groove depth

Figure 68. SEM images of WEDM-fabricated patterns (a) before and (b) after LPEB irradiation

Figure 69. Contact angles of WEDM-fabricated patterns as a function of groove depth before and after LPEB irradiation

Figure 70. Variation of droplet shape as a function of groove depth before and after LPEB irradiation

Figure 71. Quantitative comparisons between theoretical descriptions and experimental contact angles for Wenzel-to-Cassie transition

Figure 72. Comparison of liquid spread along the grooves of a WEDM-fabricated surface before and after LPEB irradiation ($d = 200 \mu\text{m}$)

Figure 73. Attenuated total reflection infrared (ATR-IR) spectra of WEDM-fabricated patterns (a) before and (b) after LPEB irradiation

Figure 74. (a) Transient CA ratios to initial CA on WEDM-fabricated patterns before and after LPEB irradiation and (b) optical microscopy images of droplets during two hours of CA measurements ($d = 250 \mu\text{m}$)

Figure 75. Photograph of spin-coated flexible AgNW electrode fabricated on a polyethylene terephthalate (PET) film

Figure 76. Schematics of thermal annealing and LPEB welding on AgNWs

Figure 77. SEM images of AgNW junctions on percolation networks following (a) spin-coating, (b) thermal annealing, (c) LPEB welding and (d) bubbles generated on the edges of AgNWs after the LPEB welding process at acceleration voltage over 5 kV

Figure 78. XRD peaks of as-prepared, thermally annealed, and LPEB-welded AgNWs

Figure 79. (a) Transmittance and (b) haze of the as-prepared, thermally annealed, and LPEB-welded AgNWs fabricated on a PET film

Figure 80. SEM images on AgNWs at five different points following (a) thermal annealing and (b) LPEB welding

Figure 81. Experimental setup for the nano-scratch tests

Figure 82. Optical micrographs on the scratch tracks after tests on (a) as-prepared, (b) thermal-annealed, and (c) LPEB-welded AgNW percolation networks

Figure 83. Penetrating depths of the nano-indentation tip in terms of the scratching distance

Figure 84. Experimental set-ups for cyclic bending tests and corresponding (b) trend lines of relative changes in a sheet resistance and (c) relative changes of sheet resistance after each individual bending

Figure 85. Fabrication of resistive touch-screen panels using LPEB-welded AgNWs and corresponding performance evaluation

Figure 86. Series of photograph of PLEDs with (a) as-prepared, (b) thermally annealed, and (c) LPEB-welded AgNWs electrodes under bending stress following different bending radius

Figure 87. Schematic describing the contributions of the dissertation in manufacturing applications

Figure 88. White-interference micrographs and corresponding surface roughness before and after the hybrid surface treatment using HPDL and LPEB

LIST OF TABLES

Table 1. Literature reviews on conventional surface finishing methods

Table 2. Thermal properties of engineering alloys

Table 3. Parameters of the LPEB irradiation

Table 4. Chemical composition (wt. %) and thermal properties of KP1 and KP4

Table 5. Corrosion potentials, corrosion current densities, and corrosion rates for KP1 and KP4 before and after the LPEB irradiation

Table 6. Chemical composition of Ti-6Al-7Nb

Table 7. Polarization electrochemical parameters of Ti-6Al-7Nb before and after the LPEB irradiation

Table 8. Parameters of the LPEB nitriding process

Table 9. Energy dispersive X-ray spectroscopy of Ti-6Al-7Nb before and after the LPEB irradiation and nitriding process in term of the negative DC bias

Table 10. Energy dispersive X-ray spectroscopy of Ti-6Al-7Nb after the LPEB nitriding process in term of the number of pulses

Table 11. Polarization electrochemical parameters before and after the LPEB nitriding process

Table 12. Roughness factors, radius of droplets, and $w2/d$ of WEDM-fabricated patterns before and after the LPEB irradiation

Table 13. EDX chemical compositions of bare and WEDM-fabricated patterns before and after the LPEB irradiation

NOMENCLATURE

Abbreviations

EB	Electron beam
EBM	Electron beam manufacturing
SEM	Scanning electron microscope
TEM	Transmission electron microscope
EBSD	Electron backscatter diffraction
LPEB	Large pulsed electron beam
EUV	Extreme ultraviolet
2D	Two-dimensional
FEM	Finite element model
3D	Three-dimensional
SS	Stainless steel
PDP	Potentiodynamic polarization
SCE	Standard calomel electrode
OCP	Open circuit potential
IQM	Image quality map
IQF	Image quality factor
XRD	X-ray diffraction
EDS	Energy-dispersive X-ray spectroscopy
CA	Chronoamperometry
LED	Light emitting diode
EDM	Electric discharge machining
WEDM	Wire-electric discharge machining
ATR-IR	Attenuated total reflectance infrared spectroscopy
NW	Nanowire
PLED	Polymer-based light emitting diode
IPA	Isopropyl alcohol
PET	Polyethylene terephthalate
FCC	Face-centered cubic
FWHM	Full width at half maximum
HPDL	High power diode laser

List of symbols

2. LITERATURE REVIEW

F	Lorentz force vector	
E	Electric field	
B	Magnetic field	
q	Charge of the electrons (-1.6110×10^{-19})	[C]
v	Velocity vector of the electron	
m_e	rest mass of the electron ($\sim 9.11 \times 10^{-31}$)	[kg]
γ	relativistic factor	
c	speed of light ($\sim 3.00 \times 10^8$)	[m/s]
\hat{z}	Uniform magnetic field directed to the emitter or the collector	
μ_0	Magnetic constant	[N/A ²]
n	Number of turns	
I	Current	[A]

3. PREDICTIVE MODEL OF THE LARGE PULSED ELECTRON BEAM (LPEB) IRRADIATION

E_0	Incident energy	[keV]
$m_1, m_2, \text{ and } m_3$	Experimental constants	
z	Depth	[m]
R	Penetration depth	[m]
m_A	Atomic mass of the solid target	[kg]
N_A	Avogadro's number	[atoms/mole]
ρ	Density of the solid target	[kg/m ³]
φ	Incident angle	[deg]
η_A	Total fraction of absorbed energy	
η_B	Fraction of backscattered electrons	
η_T	Fraction of transmitted electrons	
$d\eta_A'$	Fractional absorptance	
T	Temperature	[K] and/or [°C]
t	time	[sec]

C	Specific heat	$[J/kg\ K]$
k	Thermal conductivity	$[W/m\ K]$
q	Heat flux	$[W/m^2]$
P	Maximum power at the beam center	$[W]$
n	Concentrating factor	
$a, b, \text{ and } c$	Characteristic parameters corresponding to $x, y, \text{ and } z$ -axis	
r	Radius	$[m]$
σ	Effective radius	$[m]$
$I(x,y)$	Two-dimensional heat source intensity	$[W/m^2]$
α	Thermal diffusivity	$[m^2/s]$
τ	Temporal variable	
$d\tau$	Infinitesimal time	
Z_{\max}	Depth with the maximum absorptance	$[m]$
E_d	Energy density	$[J/cm^2]$

4. FUNDAMENTAL UNDERSTANDINGS ON THE EFFECTS INDUCED BY LPEB IRRADIATIONS

E_{corr}	Corrosion potential	$[V/SCE]$
i_{corr}	Corrosion current density	$[A/m^2]$
k	Constant factor	
M	Molar mass	$[g/mol]$
d	Density of material	$[kg/m^3]$
A	Area of working electrode	$[m^2]$
β_c	Cathodic tafel slope	$[V/dec]$
β_A	Anodic tafel slope	$[V/dec]$
R_p	Polarization resistance	$[\Omega\ cm^2]$
f	Frequency	$[Hz]$
Z	Impedance	$[\Omega\ cm^2]$

5. APPLICATIONS OF LPEB IRRADIATIONS ON MANUFACTURING PROCESSES

V_a	Acceleration voltage	$[kV]$
V_s	Solenoid voltage	$[kV]$

N	Number of pulses	
d	Depth of grooves	[m]
w	Width of patterns	[m]
p	Pitch of patterns	[m]
δ	Penetration depth of droplet into patterns	[m]
R	Radius of droplet	[m]
dE	Change of surface energy	
γ_{LA}	Surface energy of the liquid/air interface	
r	roughness factor	
θ_c	Critical angle of Wenzel-to-Cassie transition	[deg]
R_s	Sheet resistance	[Ω/sq]
τ	Size of ordered crystalline domains	
K	Dimensionless shape factor	
λ	X-ray wavelength	[nm]
β	FWHM	
θ_{tip}	Angle of the nano-indentation tip	[deg]
r_b	Bending radius	[m]

1. INTRODUCTION

Manufacturing is one of the oldest and most important aspects of engineering in our machine-based civilization after the industrial revolution [1]. At the first, most of manufacturing techniques were highly focused on achieving outstanding cost-effectiveness and productivity [2, 3]. However, most recently, the quality of products becomes an essential aspect in manufacturing along with the productivity [4]. Thus, a lot of researches on manufacturing have emphasized surface qualities including accuracy, surface mechanical/chemical properties, and surface finishes, all of which are important factors determining the quality of products. However, conventional machining processes, which are the most widely used manufacturing process, have clear limitations in the production of high-quality products because they can only cut materials into desired shapes, without imparting any quality modification effects on products. These increasing demands for high quality products are not only for massive and bulk manufacturing processes but also for micro/meso-scale parts, biomedical engineering, and precision manufacturing sectors. Thus, it has stimulated much research on manufacturing processes aiming at surface finishing, resulting in superior surface properties with fine dimensional tolerances regardless of materials.

In this respect, advanced manufacturing processes and surface finishing which are kinds of energy beam-based manufacturing have been highlighted in various industries to satisfy the requirements in high-quality products for various applications. There are various types of energy beams which are applicable for the manufacturing processes such as laser. The laser is a good candidate for the energy beam-based manufacturing due to its high lateral resolution, low heat input, and controllability [5, 6]. It has been used for patterning [7-9], turning [10], grooving [11], welding [12-14], cutting [15], and melting [16, 17]. Also the lasers have been applied for surface modification including mechanical properties modification and surface roughness reduction [18, 19]. However, it is hard to select the proper type of laser as the processing parameters such as f-number and wavelength can critically affect the processing results [20].

Most recently, electron beam (EB)-based manufacturing processes have been introduced as an alternating method of lasers. The electron beam manufacturing (EBM) is based on the melting, vaporizing, and re-solidification of materials converting the kinetic energy of accelerated electrons to thermal energy. In this context, the energy density of EB is one of the most important processing parameters in EBM. Firstly, EBs were used for analyzing microstructures of various materials [21-23] in various fields, such as scanning electron microscope (SEM), transmission electron microscope (TEM), and electron backscattering diffraction (EBSD) devices because those applications only needed low energy densities. Following the enormous advance in energy density of EBs, the application area of EBM has been broadened from machining applications such as cutting [24], drilling [25], and

welding [26], to advanced applications including lithography [27], additive manufacturing [28], and finishing [29]. As the charge-to-mass ratio of electrons is extremely small, EBM is advantageous when it is applied for the accurate and precision manufacturing. Furthermore, the surface modifying factors which can be achieved simultaneously during the irradiation facilitate the EBM simplifies its processing step without post-processing.

Briefly summarizing, the essential requirements for the future manufacturing and finishing systems should be material-independent adoptability, possibility to provide high quality products, and rapid and efficient process. In this perspective, the electron beam-based manufacturing processes could be appropriate substitutes for the conventional manufacturing and finishing processes.

1.1 Research objectives

Among the several types of energy beams available, a large pulsed electron beam (LPEB) is believed to be a good candidate for various conventional manufacturing and finishing processes due to its unique attributes. Despite modifications of the surface roughness [29] and mechanical/chemical properties of various types of materials, the application of the LPEB in industrial fields is rather limited because the improvements in chemical properties and hardening mechanisms for materials remain unclear.

To enlarge the application area of the LPEB in manufacturing, a fundamental understanding of multi-physical mechanisms such as combined energy transfer, temperature elevation, and phase transformation phenomena is essential. Although a ‘classical’ solution for temperature fields induced by energy beams could be provided by previous heat source models, the direct use of another heat source model is not suitable for the LPEB irradiations because such models do not describe the natural interactions between irradiated electrons and substrates. Thus, **the first objective of this dissertation should be a temperature predictive modeling considering the unique interactions between the irradiated electrons and substrates.**

As the LPEB interacts with various materials in different ways, the experimental approach is necessary for optimizing the process parameters to achieve the targeted properties after the finishing process. Furthermore, it is important to evidently specify the mechanisms of surface modification induced by the LPEB irradiation so as to utilize the process for the targeted materials and to achieve the desired mechanical/chemical properties. Thus, **the second objective of this dissertation is experimental approaches on the effects of the LPEB irradiation for engineering materials.** A fundamental understanding of the mechanisms of surface modification induced by the LPEB irradiation will facilitate optimization of process parameters and application of this process on micro/nanoscale manufacturing processes in industrial fields.

Following the basic level of experimental approaches, depending on the type of materials and purpose of the applications such as melting, finishing, and surface modification, the processing parameters could be optimized. Based on the effects investigated from the experimental approaches,

the third objective of this dissertation is to propose manufacturing processes using the LPEB irradiation overcoming the limitations of conventional finishing and surface modification processes. According to the firmly established multi-physical mechanisms induced by the interaction between irradiated electrons and substrates, the surface modification by LPEB irradiation could be selectively adopted, and its processing parameters could be successfully implemented for micro- and nanoscale manufacturing applications.

1.2 Research outline

This dissertation proposes the optimized manufacturing processes on multi-scale applications with various engineering materials such as metallic alloys, polymers, and composites. Based on the fundamental investigation of LPEB irradiation mechanisms by energy transfer and temperature predictive modeling, the optimum conditions are proposed for the surface modification of metallic alloys in terms of surface roughness, mechanical properties, and chemical stabilities. By exploring the surface characteristics such as microstructures and chemical components, the surface modification mechanisms are clearly defined based the inferences made from the experimental approaches. To overcome the limitations of conventional manufacturing processes and a simple LPEB irradiation, the hybrid manufacturing processes assisted by the LPEB irradiation are also developed for micro- and nanoscale applications.

The research outline of this dissertation composed of three main topics for pursuing research objectives as shown in Figure 1:

- 1) Temperature predictive modeling that describes the natural interaction between irradiated electrons and substrates for a better understanding of the mechanisms of the LPEB irradiation
- 2) Experimental approaches to explore the effects of processing parameters on the characteristics of materials after the LPEB irradiation process and propose optimal processing conditions depending on the type of materials and their target properties
- 3) Multiscale and hybrid manufacturing applications of the LPEB irradiation by selectively using proper surface modification techniques by optimally controlling the process parameters

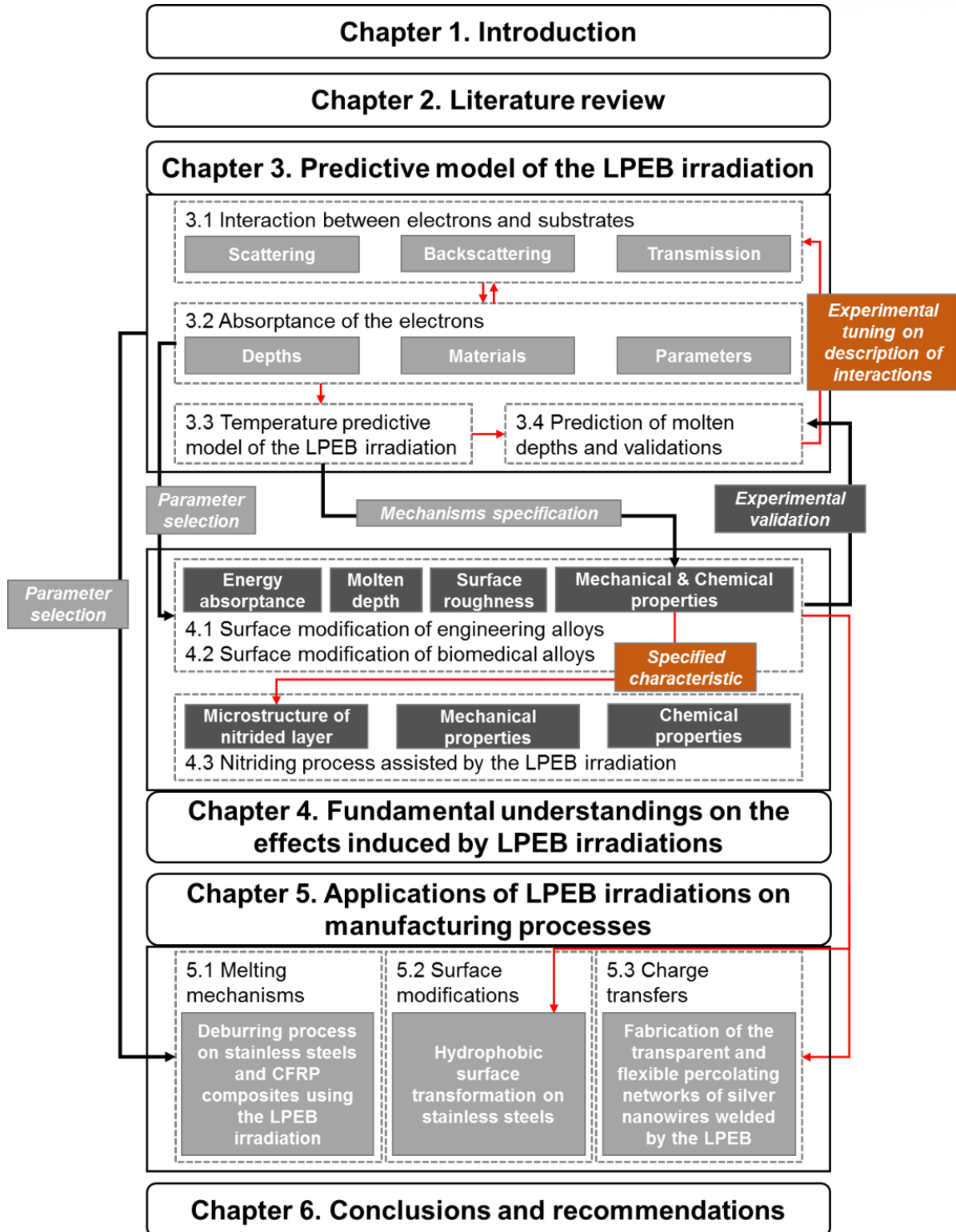


Figure 1. Research outline

2. LITERATURE REVIEWS

2.1 Conventional surface finishing and treatment processes

The surface quality of final products is mainly determined by two main factors: 1) surface textures and 2) surface properties. The conventional surface finishing methods for engineering materials were firstly focused on surface textures. The surface quality can be defined by the surface roughness. Accordingly, a lower surface roughness represents a better surface quality with fine dimensional tolerances of products in the field of manufacturing processes. Although several surface polishing techniques, such as mechanical and chemical polishing [30, 31], are available to achieve finely polished surfaces, these conventional polishing techniques cannot satisfy the recent industrial requirements of surface finishing, as they solely improve the surface roughness without concerning about the surface properties, which are also important factors in determining the surface quality of products.

In this context, there are increasing interests in improving the mechanical and chemical properties of the surface of various products. In most cases, those properties are considered as natural characteristics of alloys themselves and hence, numerous efforts have been made in developing new alloys with superior mechanical and chemical properties [32]. However, the principles to improve mechanical and chemical properties are hugely different. Thus, the previous researches on enhancing surface properties were separated in terms of the purpose they wanted to achieve. Heat treatment [33] and quenching [34] are the most representative manufacturing processes to enhance the mechanical properties of metallic alloys. However, these processes are only suitable to improve the mechanical properties of raw materials and they are hard to be adopted either on large sized products or for a target selective region. Laser irradiations and shock peening processes [35, 36] are relatively new methods to induce surface hardening. The laser-based surface hardening method mainly uses heating, melting, and phase transformation induced by laser radiations. In case of laser shock peening, compressive residual stresses induced on the surface by laser radiations facilitated surface hardening, similar to conventional shock peening processes [36].

In case of the other factor on surface quality, chemical properties, most studies on the chemical properties of metallic alloys have focused on corrosion protection of materials based on surface treatments using organic or inorganic inhibitors [37-39] over the past few decades. It is clear that the corrosion on the metallic materials can be protected by the adsorption of inhibitors as they are generally much nobler than metals. The prevention of metals from dissolution (anodic reaction) has also been studied to modify the corrosion resistance [39]. The metal-inhibitor interactions are the most important factors affecting corrosion inhibition and efficiency of the inhibitor by the adsorption [40]. Moreover, it was revealed that the corrosion properties can be critically affected by the phase of layer from the corrosion inhibition using quantum chemical approaches [41]. Accordingly, quantitative structure–

activity relationships, which mainly relate to the phase of the surface layer, should be considered. Furthermore, surface finishing processes, such as hammer peening [42], electrochemical finishing [43], UV illumination [44], and laser shock peening [45], have shown their own effects on improving corrosion resistance.

Although numerous manufacturing processes are available to improve surface quality including surface roughness, mechanical and chemical properties, those processes studied in previous should be applied independently depending on target properties as shown in Table 1. Moreover, each type of surface treatments has special concerns depending on types of materials; for example, laser types should be carefully selected considering absorptance of materials and adsorbed inhibitors to prevent corrosion reactions can be easily delaminated if mechanical properties of substrates are hugely different from those of inhibitors. There is clear need for a flexible, precise, and effective surface treatment process, which can simultaneously improve the surface quality as well as the mechanical and chemical properties.

Table 1. Literature reviews on conventional surface finishing methods

Target of surface qualities	Method	Materials	Surface roughness	Mechanical properties	Chemical properties	Ref.
Surface roughness	Chemical mechanical polishing	Silicon wafer	42 nm R_a → 0.66 nm R_a (98.4 %)	Not investigated	Not investigated	Zhou et al. [30]
	Ultrasonic vibration-assisted polishing	Tungsten carbide	3.2 nm R_a → 1.2 nm R_a (62.5 %)	Not investigated	Not investigated	Suzuki et al. [46]
	Abrasive fluid machining	Aluminum	1.8 μm R_a → 0.8 μm R_a (55.6 %)	Not investigated	Not investigated	Jain et al. [47]
Mechanical properties	Heat treatment	AISI 304 stainless steel	Not investigated	283 HV → 1,103 HV (290 %)	Corrosion ~ 50 mg → 40.2 mg (19.6 %)	Atik et al. [33]
	Quenching	Dual phase steels	Not investigated	UTS 300~800 MPa → 1,500 MPa	Not investigated	Zhong et al. [34]
	Laser hardening	Carbon steels	Not investigated	240 HV → 820 HV (70.7 %)	Not investigated	Pashby et al. [35]
	Laser shock peening	Aluminum	0.6 μm R_a → 1.3 μm R_a (-116 %)	~ 160 HV → 170 HV (5.9 %)	Not investigated	Montross et al. [36]
Chemical properties	Adsorption of corrosion inhibitor	Carbon steels	Not investigated	Not investigated	Corrosion ~ 40 mg → 5 mg (87.5 %)	Bouklah et al. [37]
	Laser & Shot peening	Stainless steels	0.05 μm R_a → 1.15 μm R_a (-2,200 %)	220 HV → 250 HV (13.6 %)	Corrosion rate 2 $\mu\text{A}/\text{cm}^2$ → 1.6 $\mu\text{A}/\text{cm}^2$ (20 %)	Peyre et al. [48]
	Zinc-Magnesium coating	Carbon steels	Not investigated	Not investigated	Corrosion fraction 79 % → 4 % (94.9 %)	Hosking et al. [49]

2.2 Surface modification processes using an electron beam irradiation

Electron beams have their own superiority in manufacturing processes, especially for heating mechanisms, to other energy sources such as extreme ultraviolet (EUV), X-ray, ion beams, and lasers excepting for its controllability and rapid energy transfer gradient [50].

The LPEB has firstly been introduced for surface finishing method of metal molds with complicated surface shapes [51]. During the repeated melting and re-solidification induced by the LPEB irradiations, tool marks and pitches could be erased. Previous reports on LPEB have revealed modifications to the surface roughness of steels. Uno et al. [51] investigated the modification of surface roughness in terms of glossiness of surfaces as shown in Figure 2. Furthermore, they also reported the possibility of improvement in corrosion resistance following the LPEB irradiation. Moreover, Okada et al. [52] investigated the effect of LPEB irradiation on orthopedic surgical tools having extremely complicated geometrical shapes made of stainless steels. They also reported the modification of surface roughness in terms of energy densities and the number of pulses. The simple experimental observations on liquid repellency was performed using blood droplets. The contact angle of blood droplets was slightly increased, indicating a blood repellency effect. They argued that the change of surface structure can be responsible for the change in contact angles. In the following research conducted by Zhang et al. [53], it was reported that crater-like defects could be obtained on the surface after the LPEB irradiation on carbon steels. Although the generation of craters degraded the surface roughness after irradiation, the density of craters can be reduced when the number of pulses is increased. The numerical simulation performed by Zou et al. [54] revealed that the melting of irradiated material started at several micrometers beneath the surface and this phenomenon can lead a partial evaporation of micro irregularities under the molten materials. Thus, the craters could be generated before the irregularities are fully evaporated during repeated irradiations.

Despite these experimental approaches on LPEB irradiations as a surface polishing method, there are lots of surface modification factors should be examined following the LPEB irradiation. The surface properties could be modified following the phase transformation during the LPEB irradiation as the melting and re-solidification occurs at a rapid rate of the order of 10^7 K/s. Furthermore, the LPEB irradiation possibly improves chemical properties on the re-solidified layer as suggested by Uno et al. [51]. In spite of its huge potential advantages in surface finishing processes, the application area of LPEB irradiation is quite limited to surface polishing of steels as the surface properties and principles of modification in mechanical and chemical properties after the LPEB irradiation remained unclear. Furthermore, the predictive model of LPEB irradiation process describing multi-physical phenomena that could occur during the irradiation process should be firmly established for a fundamental understanding of effects of LPEB irradiation.

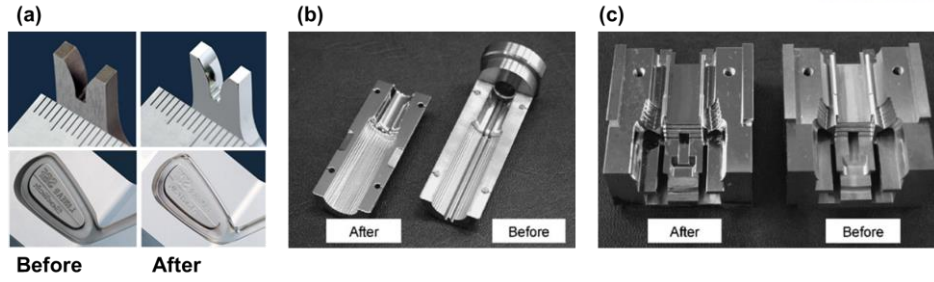


Figure 2. Optical images on the surfaces before and after the LPEB irradiation on (a) carbon steels and (b, c) mold steels [51]

2.3 Theoretical backgrounds on an electron beam irradiation

The primary phenomenon from an electron emission on the cathode is determined by the thermionic emission or field emission [55]. The outer-shell electrons transit to the free-state around the cathode surface when an excessive energy is applied to the cathode. This energy level could be described by the work function [56]. The speed of these electrons can be accelerated continuously to the one- or two-third of light passing the hollow anode. And the solenoid can induce a Lorenz force with the electromagnetic field [57]. The relationship between the electrons and the fields can be expressed as [57]:

$$\mathbf{F} = q[\mathbf{E} + (\mathbf{v} \times \mathbf{B})] \quad (1)$$

$$m_e \gamma (dv / dt) = \mathbf{F} - (qv / c^2)(\mathbf{v} \cdot \mathbf{E}) \quad (2)$$

$$\mathbf{B} = \mu_0 n I \hat{\mathbf{z}} \quad (3)$$

where, \mathbf{F} denotes Lorenz force vector on the electron, \mathbf{E} and \mathbf{B} denote the electric and magnetic field, respectively. From Eq. (1), q is the charge of the electron (-1.6110×10^{-19} C) and \mathbf{v} is the velocity vector of the electron. Eq. (2) is considered as the relativistic equation of motion, written in Newton's form. m_e is rest mass of the electron ($\sim 9.11 \times 10^{-31}$ kg), γ is the relativistic factor ($1/(1-v^2/c^2)^{1/2}$), and c is the speed of light ($\sim 3.00 \times 10^8$ m/s). Then, the uniform magnetic field (\mathbf{B}) directed to the emitter or the collector ($\hat{\mathbf{z}}$) can be expressed with Eq. (3) in terms of the magnetic constant (μ_0), the number of turns (n) and the current (I).

Although the acceleration of electron could be explained simply by thermionic emission, the main interests on EB-based manufacturing processes are energy transfer from electrons to substrates because evaluation of the EB-based manufacturing should be performed on the irradiated substrates and not on the electron beam irradiation equipment. Although surface modification using EB irradiations have been

explored by a few experimental approaches, a numerical approach to estimate the temperature distributions and processing results are still missing. A highly accurate but still simple numerical model of the EBM is needed for the pre-test optimization and post-test performance validation. Furthermore, this approach can provide appropriate processing parameters including energy density before the experiments for the target results such as surface roughness reduction and molten depths needed to eliminate pitches on the machined surfaces. The primary mechanisms of LPEB irradiation composed of energy transfer, elevation of temperature, melting, and re-solidification mechanisms. The heat-diffusion process has been modeled using various methods of heat source modeling [58-61] following a Gaussian heat source distribution. Pavelic et al. [62] firstly suggested a Gaussian-distributed energy source modeling. The corresponding Gaussian-distributed heat source model has been modified to be adopted on moving heat source models predicting molten regions during the electron beam welding processes. A 'classical' solutions for the model on temperature fields were suggested assuming a semi-infinite body [63]. The following researches tried to estimate expanded solutions for a two-dimensional (2D) Gaussian-distributed beam intensity [60]. A finite element model (FEM) for transient temperature fields with a three-dimensional (3D) distributed moving heat source has also been solved [61]. Finally, an analytical solution that can precisely predict transient temperature fields during the energy beam irradiation has been proposed by Nguyen et al. [64] assuming the semi-infinite substrates. The model has been widely adopted to predict temperatures after heat transfer processes. However, those models could not be directly adopted for pulsed electron beams as they cannot describe the unique interactions of accelerated electrons with target substrates. The pulsed electron beam irradiation processes are difficult to control and measure due to the extremely rapid pulse duration. Thus, previous researches on the modeling assumed the constant energy absorptance for the ease of prediction which is not quite accurate approach without considering the natural interactions [65]. Most of previous models have adopted experimentally fitted absorptance values. The basis of moving heat source models with a constant absorptance is too weak to use with pulsed electron beam irradiations as the interaction between electrons and substrates is highly dependent on the intensity of beams and material types. Thus, there is clear need to make more efforts to improve model accuracy following the increase of beam intensity. Although the prediction of molten pools on bulk metallic alloys could be effectively achieved by various simplified models, a numerical model for pulsed electron beam irradiation reflecting the characteristics of accelerated electrons is needed to be developed to replace such impractical concerns on rapid pulse duration and rapid thermal gradient. For example, the only roughly predicted results without specifying the exact absorptance of electron beams cannot describe the melting of micro-sized materials and/or patterns as the beam intensity of the electron beam was modified enormously (100 mA/cm^2) and the molten layer induced by irradiation was extremely thin. As this study ultimately desires for the LPEB to enlarge its application area into micro- and nano-scale applications, the predictive model for the LPEB irradiation with higher predicting accuracy should be developed.

3. PREDICTIVE MODEL OF THE LPEB IRRADIATION

The natural interactions between the accelerated electrons and substrates is influenced by several physical phenomena, such as elastic and inelastic scattering, backscattering, transmission, and absorption. The major factors in determining the absorptance of electron beams can be divided into three categories: scattering, backscattering, and transmission of electrons [66-68]. During LPEB irradiation of a solid target, backscattering of electrons is the main cause of energy loss, which adversely affects the efficiency of the beam [69]. The transmission of electrons also induces a loss of energy at the surface layer when they simply pass, without transferring the energy [70]. In spite of numerous efforts to formulate scattering, backscattering, and transmission of accelerated electrons by a series of experiments as well as by theoretical analyses, prediction of the exact energy absorptance of electron beams is yet to be explored. Thus, a three-dimensional temperature prediction model of the LPEB irradiation including the energy absorptance in the high-intensity range based on the scattering, backscattering, and transmission of electrons has been proposed in this study [71].

3.1 Interactions between electrons and substrates

For electron irradiation on a solid target surface, the backscattering phenomenon of the irradiated electrons is the largest cause of energy loss. The fractional loss of energy is represented by the backscattering coefficient, which is a representative expression for the fraction of backscattered electrons from a bulk solid target [69]. Various theoretical and empirical expressions, including Monte Carlo simulations have been proposed by previous researchers [72, 73] over a wide range of acceleration voltages. To characterize materials with electron beam irradiation techniques, the backscattering coefficient, which was validated experimentally in the incident energy range of $0.5 \leq E_0 \leq 30$ keV, was adopted in the empirical expression for the backscattering phenomenon. A curve fit to the experimental data was given by [69]:

$$B_0 = \beta[1 - \exp(-0.0066\beta^{-5/2}Z)] \quad (4)$$

where

$$\beta = 0.40 + 0.065 \ln(E_0) \quad (5)$$

Note that Eq. (4) shows a significant deviation, especially for high-atomic-number materials, due to the exclusion of incident energy. However, under the sole influence of Eq. (5), the energy term becomes more practical for application to most materials in the periodic table. Figure 3 shows the backscattering

coefficient of different materials, as a function of incident energies. As shown in Figure 3, the backscattering coefficient of materials with a low-atomic-number was significantly lower than that of materials with a high-atomic-number. Furthermore, it decreased exponentially at low incident energy regions. Nevertheless, it converged as the incident energy was increased.

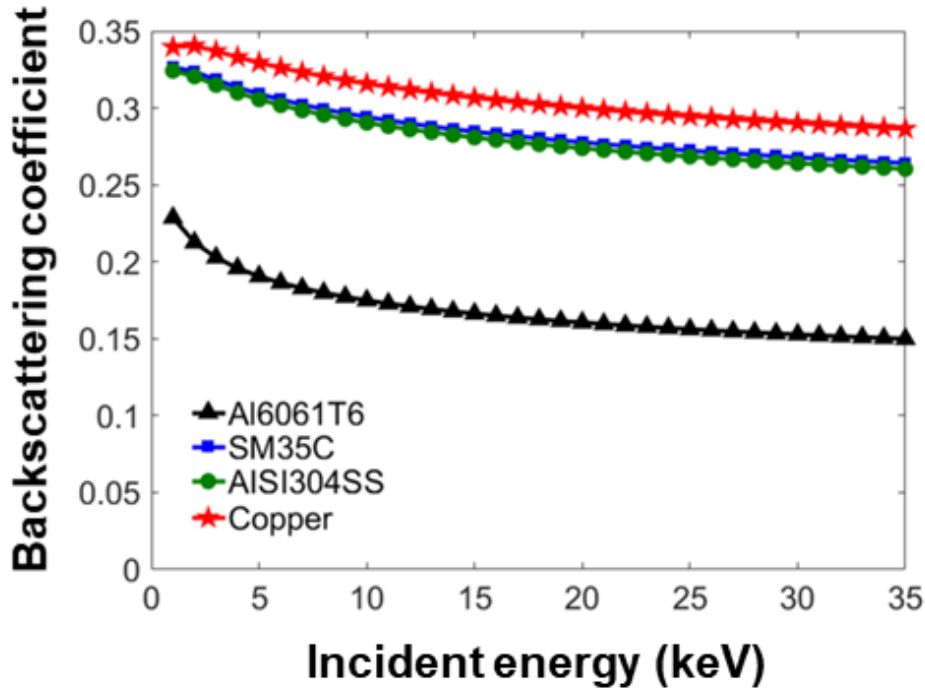


Figure 3. Backscattering coefficients of materials as a function of incident energies

The transmission of striking electrons refers to the penetration depth of accelerated electrons maintaining their energy without energy transfer or loss through scattering and backscattering. Since the possibility of collision increases following penetration, the fraction of transmitted electrons generally declines rapidly with respect to depth. This was established by Neubert et al. [70], using backscattering measurements in the range of 15–60 keV. Then, the total fraction of transmission can be expressed as:

$$\eta_T = \exp \left[-m_1(Z, \rho) \cdot \frac{(z/R)^{m_2(Z, \rho)}}{[1 - (z/R)^{m_3(Z, \rho)}]} \right] \quad (6)$$

where m_1 , m_2 and m_3 are experimental constants, z is the depth, and R is the penetration depth of the accelerated electrons. An inclusive study about electron penetration corresponding to the basis of energy loss included interpretations of the penetration depth of electrons when they were irradiated on a solid target in terms of the incident energy, as follows [74]:

$$R(Z, E_0, \rho) = \frac{2.76 \times 10^{-2} \text{ mol} / \text{m}^2 \times m_A \times N_A \times (E_0 / \text{keV})^{5/3}}{Z^{8/9}} \times \frac{(1 + 0.978 \times 10^{-3} \times E_0 / \text{keV})^{5/3}}{(1 + 1.957 \times 10^{-3} \times E_0 / \text{keV})^{4/3}} \times \frac{1}{\rho} \quad (7)$$

where E_0 is the incident energy, m_A is the atomic mass of the solid target, N_A is Avogadro's number, and ρ is the density. For experimental constants m_1 , m_2 , and m_3 , Klassen et al. [75] introduced a least-squares fit to experimental data using their own ansatz functions, $m_i(Z, \varphi)$, as follows:

$$m_1(Z, \varphi) = 4.17 \cdot Z^{0.04} - 3.28 \cdot (\sin \varphi)^{0.77 \cdot Z^{0.2}} \quad (8)$$

$$m_2(Z, \varphi) = (6.12 / Z^{0.4}) \cdot (\cos \varphi)^{Z^{0.72} / 85} - (10 / Z^{0.7}) \cdot (\sin \varphi)^2 \quad (9)$$

$$m_3(Z, \varphi) = (Z^{0.72} / 72) + 0.72 \cdot Z^{0.14} \cdot (\sin \varphi)^{1.23 \cdot Z^{0.2}} \quad (10)$$

where φ is the incident angle. Figure 4 shows the total fraction of transmitted electrons in terms of material types, incident energy, and depth. The maximum penetration depths of materials were highly dependent on atomic number. Transmission revealed opposite results with respect to backscattering coefficients. For the same incident energy, deeper penetration depth and slower decay of transmission were obtained for materials with a lower atomic number. However, the maximum penetration depth and transmission increased after the incident energy was increased from 25 to 30 keV. This could be attributed to the increased kinetic energy of the accelerated electrons at higher incident energy.

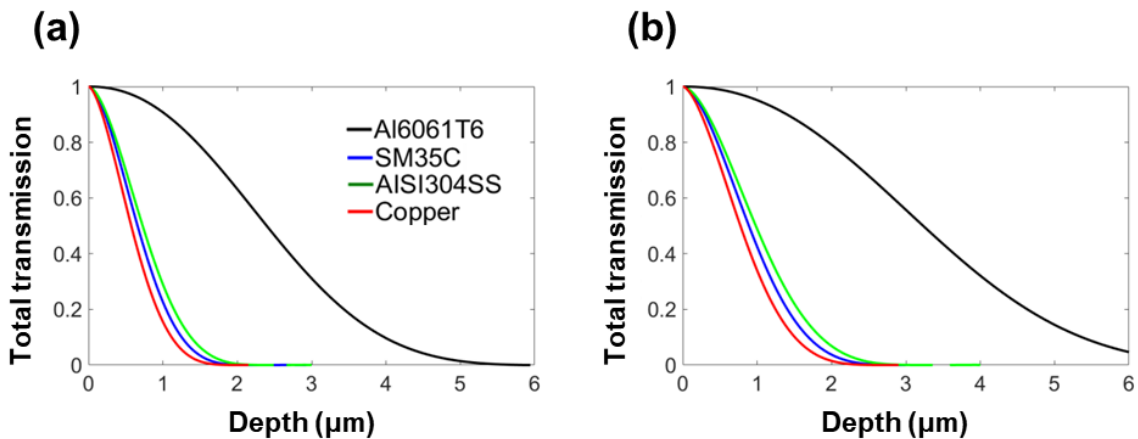


Figure 4. Total transmission of the accelerated electrons of different materials at different depths when irradiated with incident energies of (a) 25 keV and (b) 30 keV

3.2 Absorptance of the electrons

The total fraction of absorbed energy (η_A) by scattering can be determined based on the transmission and backscattering of accelerated electrons, as follows [68]:

$$\eta_A = 1 - (\eta_B + \eta_T) \quad (11)$$

To define the fractional absorptance at a certain depth, it is necessary to assume an imaginary plane on a bulk solid target. As illustrated in Figure 5, backscattered electrons at a certain imaginary plane could be absorbed again at an upper plane. Considering this mechanism of energy transfer, the total transmission of electrons from the top surface to a certain depth can be expressed as:

$$\eta_T' = \eta_T + \eta_T \eta_B^2 + \eta_T \eta_B^4 + \dots + \eta_T \eta_B^{2(n-1)} - (\eta_T \eta_B + \eta_T \eta_B^3 + \dots + \eta_T \eta_B^{2n-1}) = [\eta_T (1 - \eta_B)] / (1 - \eta_B^2) \quad (12)$$

Adopting Eq. (12) into (11) as a form of the total fraction from the top surface up to the certain depth, the total absorptance in terms of depth can be expressed as:

$$\eta_A' = 1 - (\eta_T' + \eta_B) = (1 - \eta_B) \left(\frac{\eta_A + \eta_B (1 - \eta_B)}{1 - \eta_B^2} \right) \quad (13)$$

Finally, the fractional absorptance ($d\eta_A'$) at a certain imaginary layer as a function of depth can be defined as:

$$d\eta_A' = \frac{d(d\eta_A')}{dz} \quad (14)$$

Figure 6 shows the fractional absorptance of energy transferred as a function of depth. The fractional absorptance curves indicate that the atomic number of the material is the most important parameter in determining the maximum penetration depth and absorptance of the LPEB.

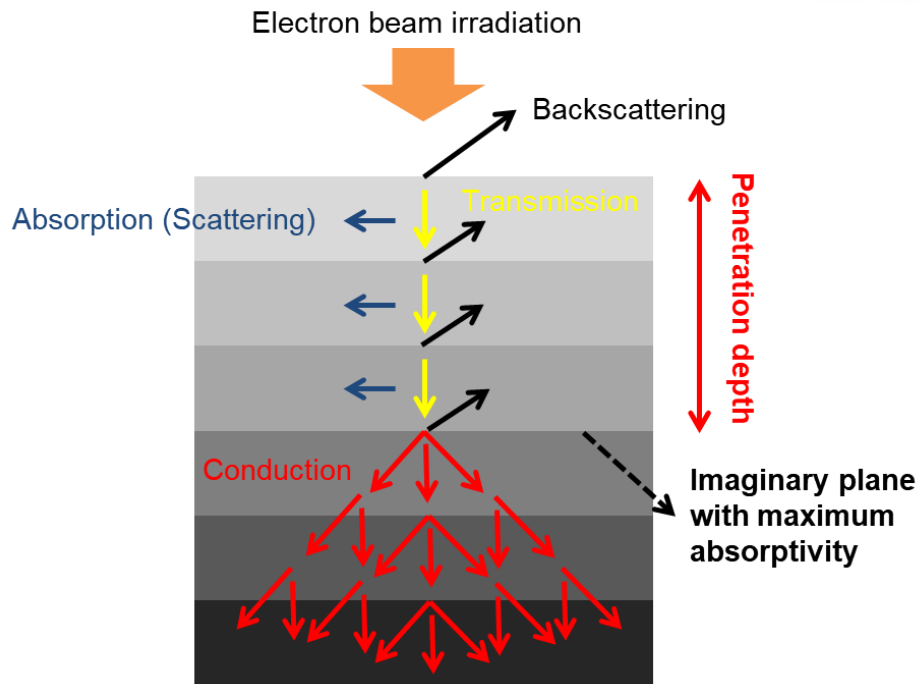


Figure 5. Schematic diagram of the energy transfer from the LPEB to the substrate, illustrating backscattering, transmission, and energy absorption

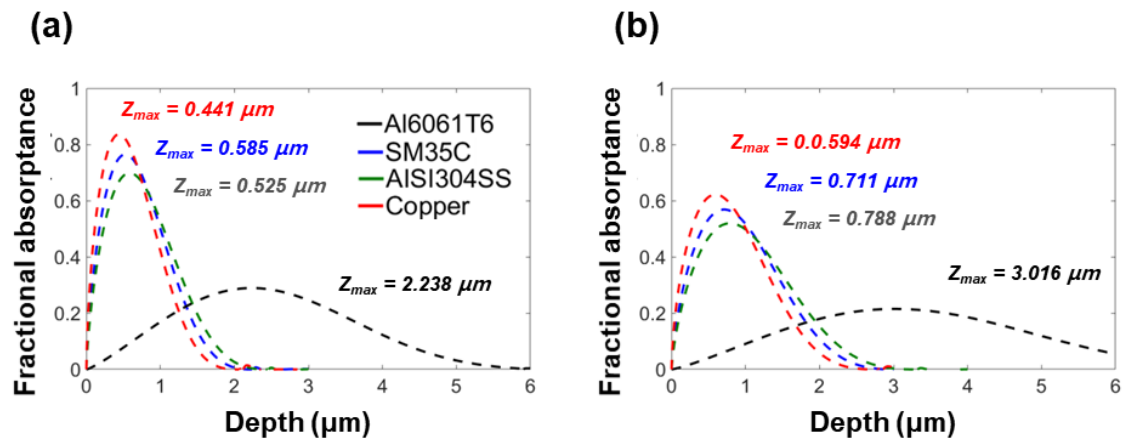


Figure 6. Fractional absorptance of the LPEB as a function of depth for different materials at incident energies of (a) 25 keV and (b) 30 keV

3.3 Temperature predictive model of the LPEB irradiation

LPEB irradiation can be analyzed theoretically by describing the heat transfer process between the electron beam and the solid substrate. A 3D semi-quantitative transient heat-diffusion equation can be used to analyze the heating process of a substrate under LPEB irradiation. The energy transfer and heat diffusion, which is the description of heat transfer in a solid substrate, can be formulated simply using the general heat conduction equation in a 3D Cartesian coordinate system:

$$\rho C \frac{\partial T}{\partial t} = \nabla \cdot (k \nabla T) + \nabla \cdot q \quad (15)$$

where T is temperature, t is time, q is density, C is the specific heat, k is thermal conductivity, and q is heat flux into the target by the LPEB irradiation. This general heat conduction equation directly shows the energy transfer mechanisms of electron beam irradiation with assumptions of no convection. The radiative heat loss can also be ignored due to the extremely short time scale of LPEB pulses and rapid thermal gradient.

The initial and boundary conditions can be expressed as follows:

$$T(x, y, z, 0) = T_0 \quad (16)$$

$$\frac{\partial T}{\partial z} = 0 \quad (\text{at } z = 0) \quad (17)$$

$$T(\infty, t) = T_0 \quad (18)$$

where Eq. (17) accounts for neglecting any types of heat transfers and losses on electron beam-irradiating surface excepting for the heat input transferred by the LPEB irradiation. The boundary condition represented by Eq. (18) can be rationalized on the basis of the size of LPEB equipment, which is large enough to maintain the temperature during the irradiations, thus serving as a thermal reservoir.

Heat source modeling is an important factor because it includes the beam shape and the effective radius of the beam. The most frequently used method for a prescribed beam distribution is using the heat input as a heat flux at the integrating points, which is then transformed to the nodes as temperature fields. A Gaussian distribution is one of the most common heat sources of an energy beam, and is expressed in the general form of [61, 76]:

$$I(x, y, z) = \frac{nP}{\pi abc} \exp[-(nx^2 / a^2)] \exp[-(ny^2 / b^2)] \exp[-(nz^2 / c^2)] \quad (19)$$

where P is the maximum power at the beam center, n is a concentrating factor, and a , b , and c are characteristic parameters of the beam distribution, corresponding to the x , y , and z axes, respectively.

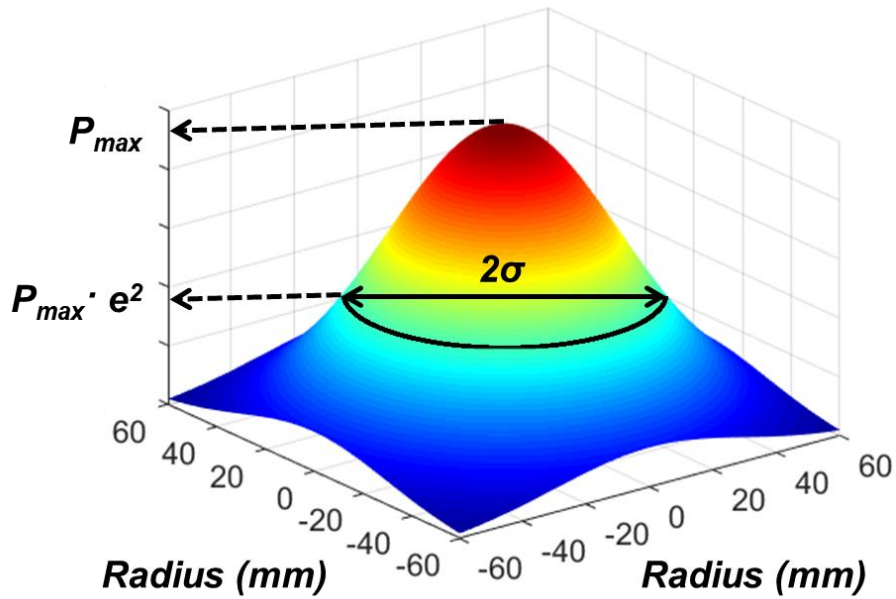


Figure 7. Gaussian-distributed beam intensity

The beam intensity model is as shown in Figure 7, for which parameters were provided for a PF32B electron beam surface finishing machine (Sodick, Japan) from experimental measurements of beam intensities. In Figure 7, the characteristic parameter r , equivalent to the effective beam radius, is taken as $r = \sigma$, of which the distributed power density, P , is 13.5% of the maximum power density, measured at the center of the beam on the target surface. Since the radius of the beam on the surface was relatively large, a plane heat source was assumed to be applied directly to the specimen surface for a short time period. Finally, the Gaussian surface-distributed heat source intensity of the incident electron beam, $I(x,y)$, was modeled as:

$$I(x, y) = \frac{2P}{\pi\sigma^2} \exp\left[-\frac{2(x^2 + y^2)}{\sigma^2}\right] \quad (20)$$

The characteristic parameters, a , b , and c , were taken to be equal to σ and $z = 0$ at the surface in Eq. (19). The heat input originating from the energy absorption of an electron beam pulse during the pulse duration for point-wise calculation can be described as:

$$\delta q = I(x, y)\delta x\delta y \quad (21)$$

The governing equation, Eq. (15), can be solved point-wise, first with an instantaneous Gaussian heat source to provide a point heat source solution. Subsequently, spatial integration over the distributed region is conducted by the superposition of the point solution as:

$$dT' = \frac{4Pd\tau}{\rho C \pi \sigma^2 [4\pi\alpha(t-\tau)]^{3/2}} \int_{-\infty}^{+\infty} dx \int_{-\infty}^{+\infty} dy \times \exp \left[-\frac{2(x^2 + y^2)}{\sigma^2} + \frac{(x^2 + y^2 + z^2)}{4\alpha(t-\tau)} \right] \quad (22)$$

where α is the thermal diffusivity and τ is a temporal variable. The total increase in temperature is then the integration of all contributions with respect to time in a given time interval that is equal to the pulse duration [77]. Thus, the temperature variation during the pulse duration can be expressed as:

$$T - T_0 = \frac{4P}{\rho C \pi \sqrt{4\alpha\pi}} \int_0^t \frac{d\tau (t-\tau)^{-1/2}}{\sigma^2 + 8\alpha(t-\tau)} \times \exp \left[-\frac{2(x^2 + y^2)}{\sigma^2 + 8\alpha(t-\tau)} - \frac{z^2}{4\alpha(t-\tau)} \right] \quad (23)$$

where $d\tau$ is an infinitesimal time, t is the pulse duration, and z is the heat penetration depth. Assuming uniformity of the radial irradiation of the electron beam and homogeneity of the material properties involved, the domain of Eq. (23) can be simplified as a two-dimensional ($x^2 + y^2 = r^2$) coordinate. The consequent temperature fields could be approximated adopting the absorptance calculated considering backscattering and transmission of electrons by multiplying absorptance to P in Eq. (23).

With numerical approximations, an investigation was conducted primarily on temperature distributions on the material surface and heat penetration into the material depth to determine the melting zone during the LPEB irradiation period. The predicted results of molten depths were compared, assuming constant absorptance and absorptance corresponding to electron-materials interactions, and the effects of the unique relationships between accelerated electrons and substrates were evaluated. Finally, numerical models for absorptance and temperature prediction induced during LPEB irradiation were validated by directly comparing the molten depths of different metallic alloys, including Al6061T6, SM35C, AISI 304 stainless steel (SS), and copper.

As shown in Figure 6, the depth absorbing the maximum fraction of energy from the accelerated electrons can be determined by calculating fractional absorptance versus depth. Then, it is possible to define the major imaginary plane of energy absorption to which the governing equation of heat conduction could be applied, at the depth with the maximum absorptance (indicated as Z_{\max} in Figure 6). Consequently, conduction of heat starts from the plane of maximum absorptance to the upper and/or lower regions of solid substrates. The most accurate prediction on the temperature fields can be obtained by the superposition of the point solutions at each depth considering the depth-dependent absorptance. However, for the simplicity of numerical predictions, it is reasonable to assume a symmetric conduction of the heat absorbed at Z_{\max} to the upper and/or lower regions as the absorptance distributions are highly concentrated at Z_{\max} and symmetrically decreased following the increasing distance from Z_{\max} (shown in Figure 6). The temperature fields induced in substrates were solved numerically using Eq. (23) for

the representative engineering metals at different incident energy densities and a 2- μ s irradiation period which is the same period with the experimental pulse duration. As the maximum temperature and molten depth could be obtained at the end of pulse duration, the temperature fields were analyzed at 2 μ s among transient temperature responses. The energy absorption of the substrates and temperature distributions were calculated with a normal incident only. The molten depths of materials were evaluated by the standard of melting points.

Table 2 summarizes the thermal properties of engineering metals. Figure 8 shows the 3D and cross-sectional temperature distributions of materials in terms of incident energy. As the maximum absorption of energy was calculated at a certain depth, the maximum temperature in the irradiated substrates was not observed on the top surface but at a certain depth, which is simply near the depth of the maximum absorptance. Also, the temperature was reduced slightly in the radial directions because the intensity of the LPEB follows a Gaussian distribution. The highest and lowest temperatures were observed for AISI 304 SS and copper, respectively. The thermal diffusivity and specific heat are the most important parameters in determining the temperature distribution after LPEB irradiation. When compared with other materials, AISI 304 SS has a relatively low thermal diffusivity. This means that the energy transferred from the LPEB could not be spread within an extremely short pulse duration. Also, the temperature is elevated readily with its low specific heat. Furthermore, this also caused a large temperature gradient versus depth, as indicated by the rapid variation in colors. In contrast, copper has a much higher thermal diffusivity, although its specific heat is slightly lower than that of the AISI 304 SS. This induced rapid thermal dissipation in the energy absorbing layer before temperature elevation. Thus, the lowest temperature was obtained for copper and the temperature gradient versus depth obtained for copper was also much lower than those obtained for other materials.

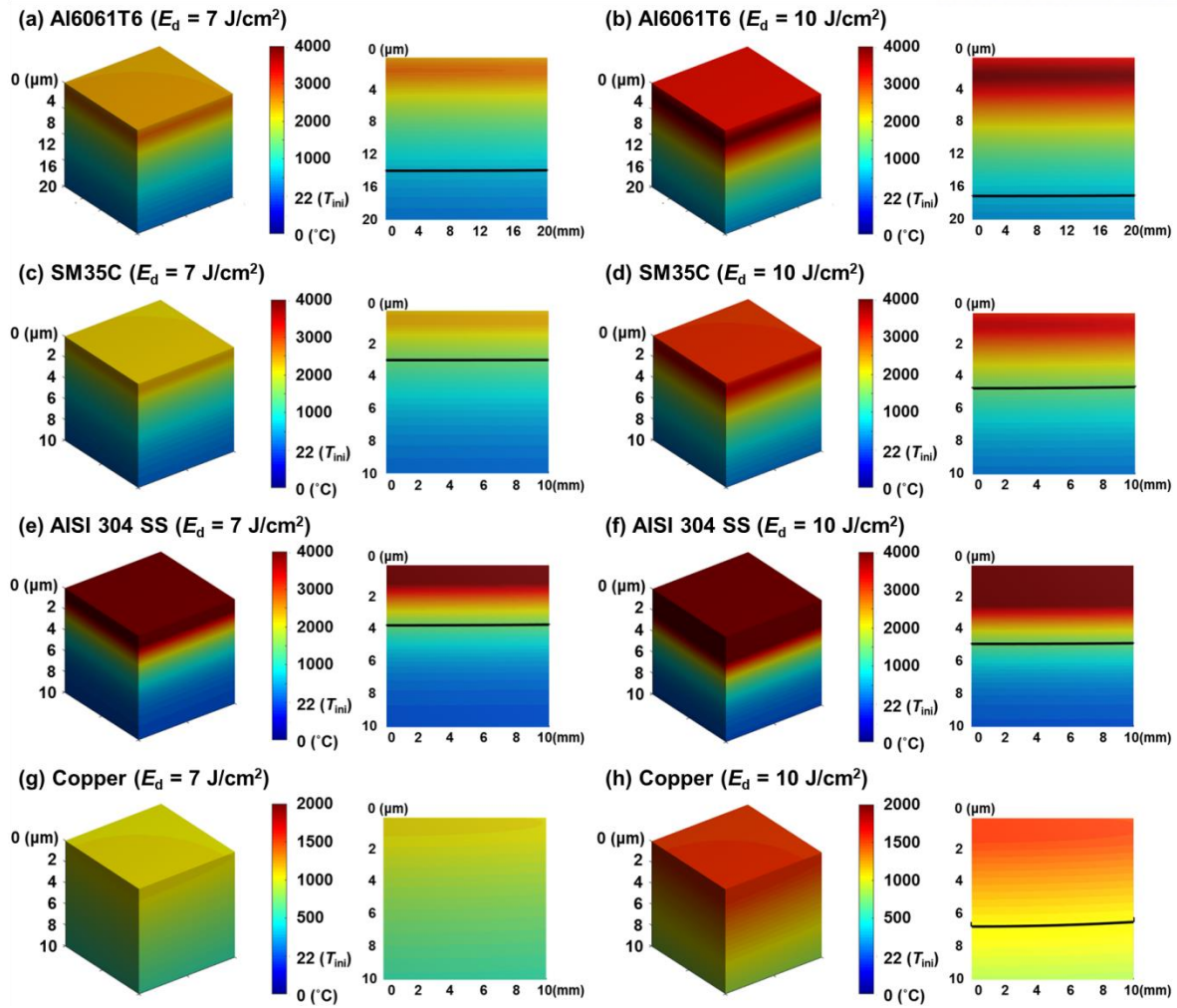


Figure 8. 3D temperature distributions and cross-sectional analyses of molten depth as a function of incident energy and material

Table 2. Thermal properties of engineering alloys

Materials	Density (kg/m ³)	Specific heat (J/kg-K)	Thermal diffusivity (mm ² /s)	Melting point (°C)
Al6061T6	2700	1100	58.8	660
SM35C	8000	647.2	5.05	1455
AISI304SS	8000	598	6.36	1400
Copper	8960	503.5	63.9	1085

3.4 Prediction of molten depths and experimental validations

The molten depths were also evaluated and are indicated by the black line on the cross-sectional temperature distribution (Figure 8). The molten depths were increased with an increase in the incident energy from 7 to 10 J/cm². The maximum molten depth was predicted for Al6061T6 because its melting point was the lowest among the materials considered. In the case of copper, the temperature induced by LPEB irradiation with an incident energy of 7 J/cm² was predicted to be insufficient to melt the material. However, a 6.4 μm-thick molten layer was predicted for the incident energy of 10 J/cm². Following the

tendency of temperature, the molten depths were also reduced along the radial direction, affected by the Gaussian-distributed beam intensity.

Several experiments were conducted with four different materials to validate the numerical approximations. Specimens having a dimension of 20 x 20 x 10 mm were prepared by mechanical machining. LPEB irradiations were performed with conditions equivalent to those used for the numerical predictions. Figure 9 shows the schematic diagram of the experimental set-ups and Table 3 summarizes the details of the experimental parameters of LPEB irradiation. After LPEB irradiation, the specimens were cut at the center to analyze the molten depth in cross-sections. Because the molten layers were difficult to observe without a grain structural investigation, the specimens were ground using 180, 320, 600, and 1200-grit SiC coated abrasive papers and polished using a 1- μm diamond suspension. Finally, all specimens were etched with suitable etchants, depending on the material type.

Table 3. Parameters of the LPEB irradiation

Parameter	Value
Effective beam radius (σ)	30 mm
Incident energy (E_0)	25 / 30 keV
Energy density (E_d)	7 / 10 J/cm ²
Pulse duration	2 μs

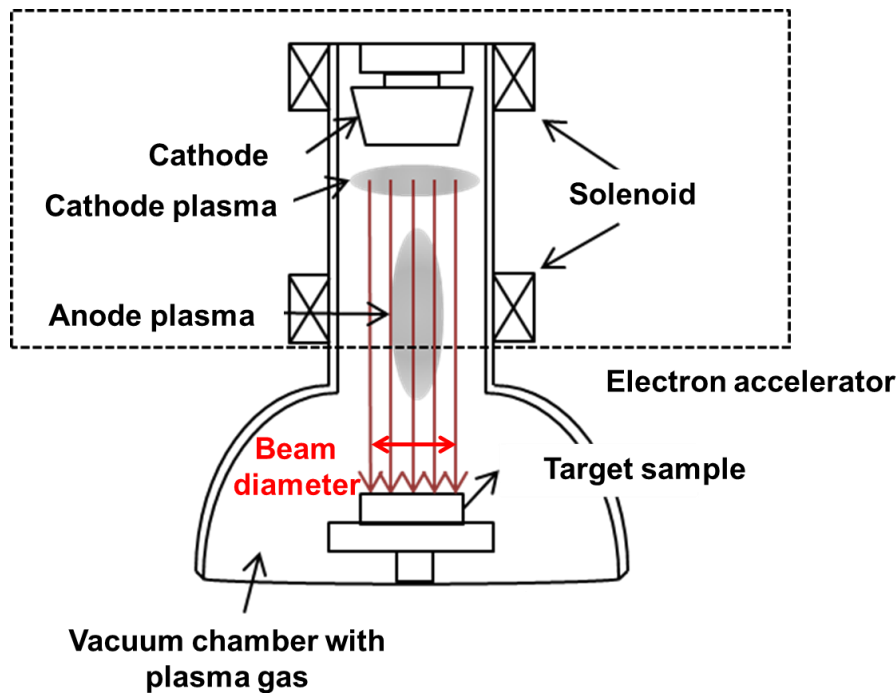


Figure 9. Schematic diagram of the experimental set-ups for the LPEB irradiation

Figure 10 shows the cross-sectional scanning electron microscopy (SEM) images of materials after LPEB irradiation as a function of the incident energy. The molten depths were measured at five different points on each specimen to minimize measurement errors, and the range of the molten depth distribution

was indicated in Figure 10. Molten layers that could be recognized by phase transformation were observed clearly in Figure 10. The tendencies in molten thickness matched well with the numerical predictions; the molten depth was increased with an increase in incident energy; the maximum and minimum molten depths were obtained for Al60601T6 and copper, respectively. Figure 11 shows a direct comparison of molten depth in each material depending on the incident energy. To clearly identify the importance of absorptance investigations, numerical predictions of molten depth were carried out with two different assumptions in absorptance: perfect absorption on the top surface (represented by blue triangle in Figure 11) and a calculated absorptance, considering scattering, backscattering, and transmission (represented by red circle in Figure 11). With the assumption of perfect absorption, the accuracy of the molten depth prediction was highly variable, depending on the incident energies and material types. Most predictions were out of range when compared with the experimentally measured molten depths at an incident energy density of 7 J/cm^2 . In fact, only the predicted molten depth of Al6061T6 was within the experimental error bounds. In the case of 10 J/cm^2 incident energy, the predictions were relatively accurate; however, the predicted molten depth of copper was 45% larger than the averaged experimental measurement.

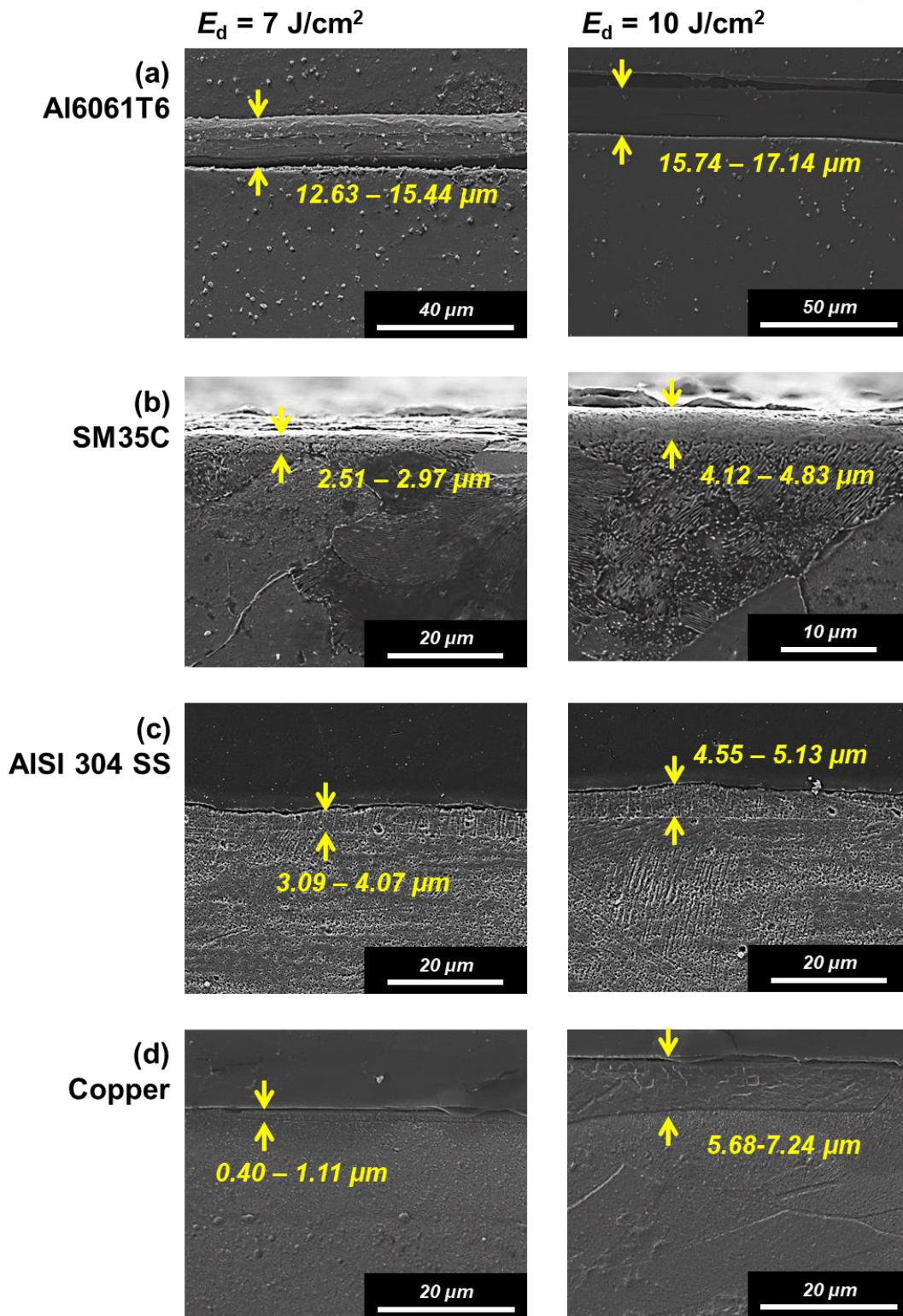


Figure 10. Cross-sectional SEM images indicating molten depth of the investigated materials as a function of energy density

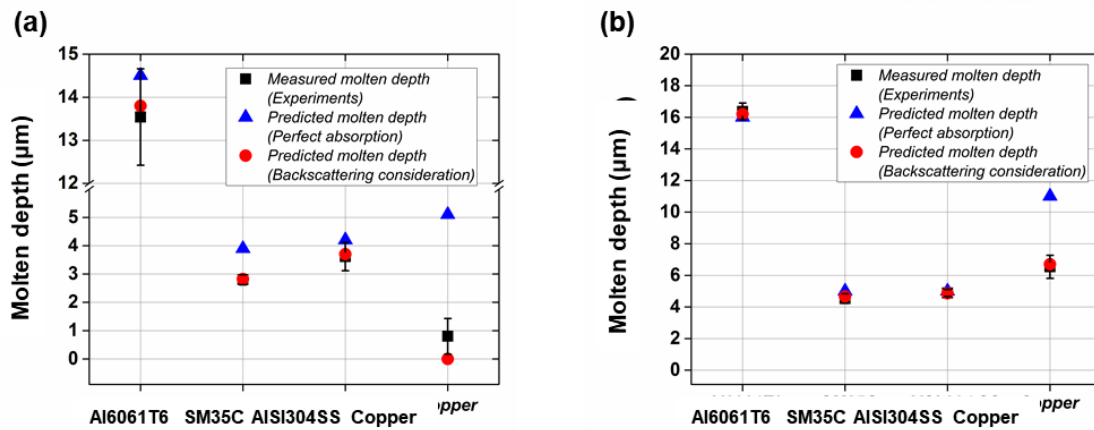


Figure 11. Comparisons of predicted and experimentally measured molten depths of different materials obtained at incident energies of (a) 25 keV and (b) 30 keV

The adoption of calculated absorptance versus depth resulted in predictions of thinner molten depths than those predicted by assuming perfect absorption. Unlike the values assuming perfect absorption, the molten depth predictions agreed well with the experimentally measured molten depths regardless of the incident energy and material. Consequently, it can be concluded that the proposed numerical model for absorptance, temperature field, and molten depth prediction, corresponding to scattering, backscattering, and transmission, can simply and accurately describe natural interactions of LPEB irradiation on solid substrates. Furthermore, the model is trustworthy in providing numerical predictions of temperature fields and molten depths.

4. Fundamental understandings on the effects induced by LPEB irradiations

4.1 Surface modification of engineering alloys

As described in the previous chapter, the surface of substrates briefly melts, erasing tool marks and pitches, and then rapidly re-solidify. Due to the extremely rapid heating and cooling of the surface, which occurs at a rate of 10^7 K/s, a phase transformation of the re-solidified layer can occur, causing variations in the structural properties of the surface. Despite the several experimental approaches were explored on the adoption of LPEB irradiation as finishing and surface modification process as discussed in Chapter 2, improvements in surface chemical properties and hardening mechanisms for metallic alloys following the LPEB irradiation still remains unclear. It is important to understand the modification mechanisms of surface properties following the LPEB irradiation on metallic alloys. In addition, the processing parameters should be properly optimized to achieve the targeted properties by inducing appropriate effects on the irradiated surface.

4.1.1 Design of experiments and materials

The LPEB surface finishing and modification process is adopted on the KP1 and KP4 mold steels to investigate the surface modification factors [78]. The surface quality of mold steels is an important factor to produce high quality products as the defects on the mold surface might generate imperfections such as shrinkage cavities on the final products. The surface of molds can be easily degraded due to corrosion and wear. Thus, the surface modification process on mold steels is essential to provide improved surface properties. KP1 and KP4 mold steels have been widely used especially in injection molding industries. KP1 is a low-carbon steel used to produce large molds and has good machinability. KP4 is also a low-carbon steel and is used for core and cavities of molds because of its large hardness, which is achieved by the use of relatively high chromium and molybdenum contents. Although KP4 has favorable corrosion resistance and wear resistance, it is less amenable for machining than KP1. The chemical components and thermal properties of these steels are summarized in Table 4.

Table 4. Chemical composition (wt. %) and thermal properties of KP1 and KP4

	Fe	Mn	C	Ni	Mo	Cr	S	P	k_c (W/m K)	C_p (J/g C°)	α (mm ² /s)
KP1	98	0.65	0.5	0.4	-	-	0.03	0.025	49.8	0.486	13.05
KP4	97	0.85	0.3	0.4	0.3	1.1	0.035	0.025	37.7	0.519	9.25

The LPEB assembly consisted of an electron acceleration system, a solenoid, and a two-dimensional (2D) translation stage enclosed within a vacuum chamber. The chamber was filled with argon gas at 0.05 Pa, which was used to form plasma. The electron beam was transmitted through the low-pressure

argon gas to the surface of the sample. The distance from the electron gun to the surface of the substrate was kept constant at 30 mm. During LPEB irradiation, the electrons were accelerated in a spiral path using the electric and magnetic fields induced by the solenoid. The energy density used for LPEB irradiation was in the range 7 to 10 J/cm². The spatial cross-section of the beam followed a Gaussian distribution, and the diameter of the beam was 60 mm. The size of the KP1 and KP4 substrates was 40 mm x 40 mm x 5 mm. Each irradiation cycle consisted of 9 pulses, with the translation stage moving by 20 mm following each pulse to provide a 3 x 3 grid of irradiation sites to achieve a uniform surface coverage with a homogeneous surface finish.

4.1.2 Formation of the re-solidified layer

The incident electron beam induced a short-lived thermal gradient at the surface of the substrates. During this process, the surface of the target gets melted and then re-solidified. The morphology and surface properties were therefore varied. The LPEB irradiates the substrate for a pulse duration of 2 μs, after which the substrate cools, with a relatively long dwell time of 10 s between irradiations. It follows that the LPEB irradiations are independent of each pulse, so that the depth of the re-solidified layer following the LPEB irradiation does not significantly vary between irradiations.

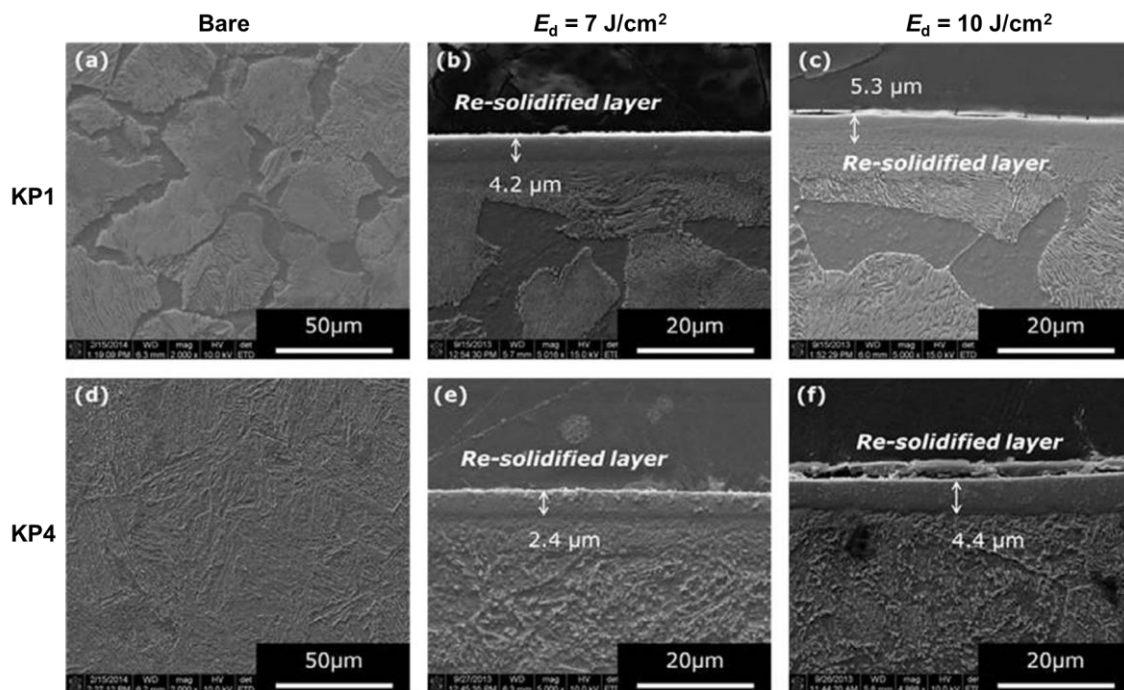


Figure 12. Cross-sectional SEM images of KP1 and KP4 samples before and after the LPEB irradiation

Figure 12 shows cross-sectional SEM images of the untreated and LPEB-irradiated KP1 and KP4. The formation of re-solidified layers was clearly observed, and the crystal phases of the re-solidified layers differed significantly from those of the initial materials. The depth of the re-solidified layer of

KP1 was $4.2 \mu\text{m}$ at an energy density of 7 J/cm^2 and it increased to $5.3 \mu\text{m}$ when the energy density is increased to 10 J/cm^2 . The depth of the re-solidified layer at the surface of KP4 was $2.4 \mu\text{m}$ at an energy density of 7 J/cm^2 and it increased to $4.4 \mu\text{m}$ when the energy density is increased to 10 J/cm^2 .

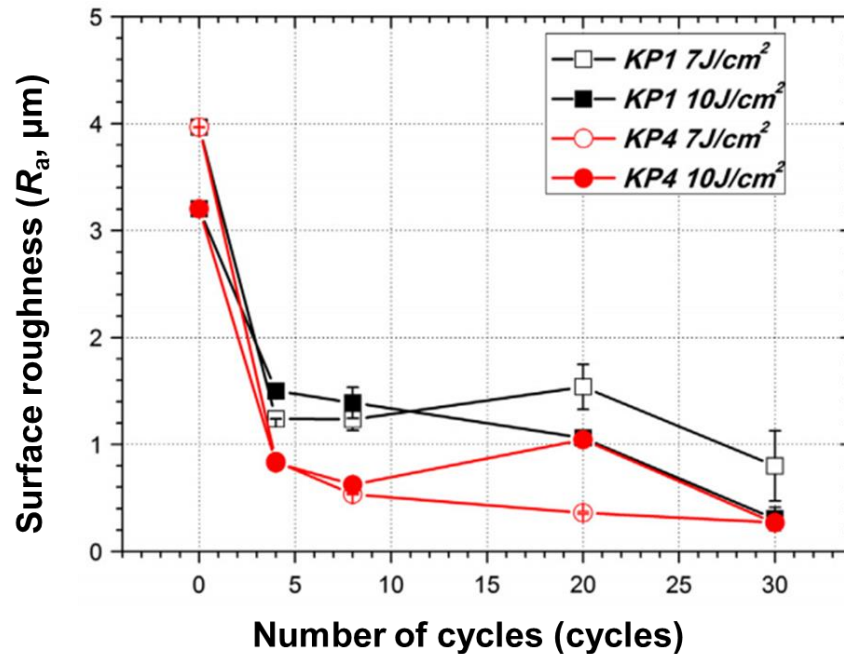


Figure 13. Surface roughness as a function of the number of LPEB irradiation cycles

As the formation of re-solidified layers was induced by the repeated melting and re-solidification, the surface defects such as tool marks and scratches could be effectively eliminated by the LPEB irradiations. The average surface roughness (R_a), shown in Figure 13, is decreased with an increase in the number of irradiation cycles at both energy densities (i.e., 7 J/cm^2 and 10 J/cm^2). The average surface roughness decreased the most from $R_a = 4 \mu\text{m}$ to $R_a = 0.271 \mu\text{m}$ for the KP1 sample at an energy density of 10 J/cm^2 for 30 irradiation cycles. The average surface roughness of the KP4 sample is changed from $R_a = 3.2 \mu\text{m}$ to $R_a = 0.267 \mu\text{m}$ following 30 irradiation cycles of LPEB at an energy density of 10 J/cm^2 .

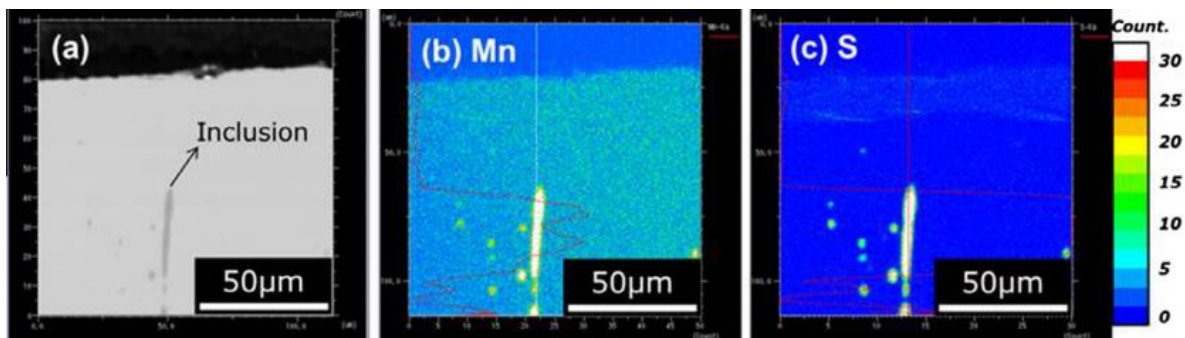


Figure 14. Electron probe micro-analysis on a cross-sectional area of the samples containing manganese sulfide inclusions

Although the overall surface roughness is decreased following LPEB irradiations following the removal of tooling marks, the presence of the eruptive craters on the surface served as artifacts that has led to a large surface roughness especially for the KP1 and KP4. During the LPEB irradiation, craters may form following eruptions and partial evaporation of non-metallic inclusions, such as manganese sulfide (MnS) and carbides [53]. Both KP1 and KP4 contain MnS inclusions, as shown in Figure 14, and craters were observed on the surface of the samples following the LPEB irradiation. Figure 15 shows the crater density on the surface after the LPEB irradiation as a function of the number of irradiation cycles. The density of the craters was larger on the surface of the KP4 sample since KP4 contains more manganese and sulfur than KP1 (see Table 4). During repeated irradiations, the non-metallic inclusions near the surface could be fully evaporated and decomposed. Thus, the density of craters is decreased as the number of irradiation cycles is increased. For the KP1 and KP4 samples investigated here, the removal of the tooling marks had a large impact on the surface roughness while the eruptive craters had a much smaller effect. Thus, the average surface roughness (R_a) is decreased significantly following the LPEB irradiations.

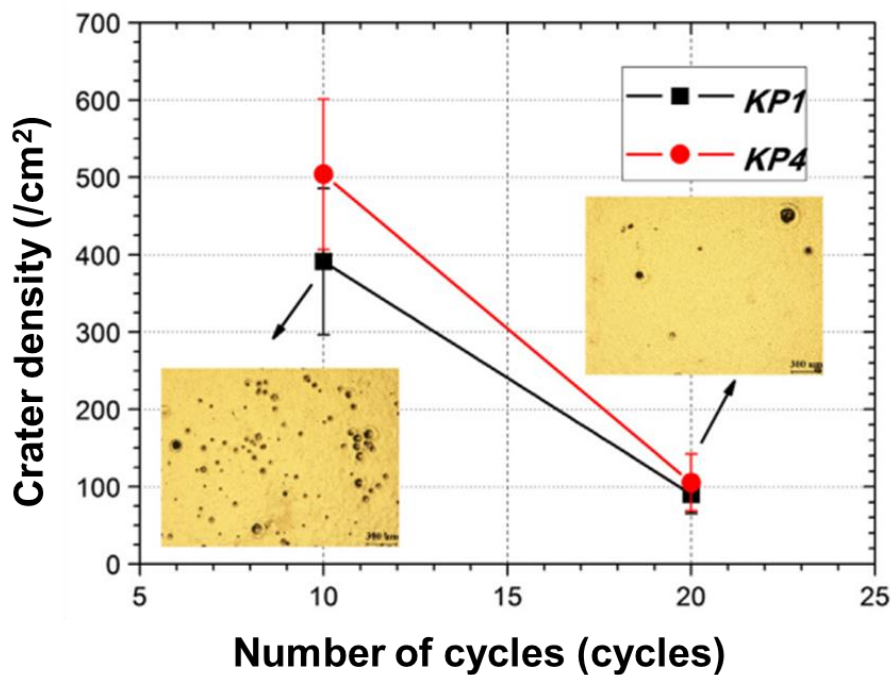


Figure 15. Crater densities generated on the surface of KP1 and KP4 after the LPEB irradiation

4.1.3 Mechanical properties

During the LPEB irradiation process, the rapid thermal gradient could cause phase transformation and modification of surface mechanical properties. Figure 16 shows the nano-hardness and elastic modulus as a function of the depth from the irradiated surface of KP1 and KP4 samples at an energy density of 10 J/cm². It can be clearly seen that both the nano-hardness and elastic modulus are

significantly increased on the LPEB-irradiated surface. The nano-hardness was increased from 3.75 GPa on the untreated surface to 15.4 GPa on the re-solidified layer for the KP1 sample. Under the same irradiation conditions, the elastic modulus was increased from 205.64 GPa to 298.66 GPa following LPEB irradiation. For the KP4 sample, under similar irradiation conditions, the nano-hardness on the re-solidified layer was increased from 4.9 GPa to 12 GPa, and the elastic modulus was increased from 222.84 GPa to 271.02 GPa. It is clear that the LPEB irradiation was more effective on the KP1 sample than on the KP4 sample. The initial surface hardness and elastic modulus of KP1 were slightly lower than those of KP4; however, following LPEB irradiations, both the surface hardness and elastic modulus of KP1 were larger than those of KP4.

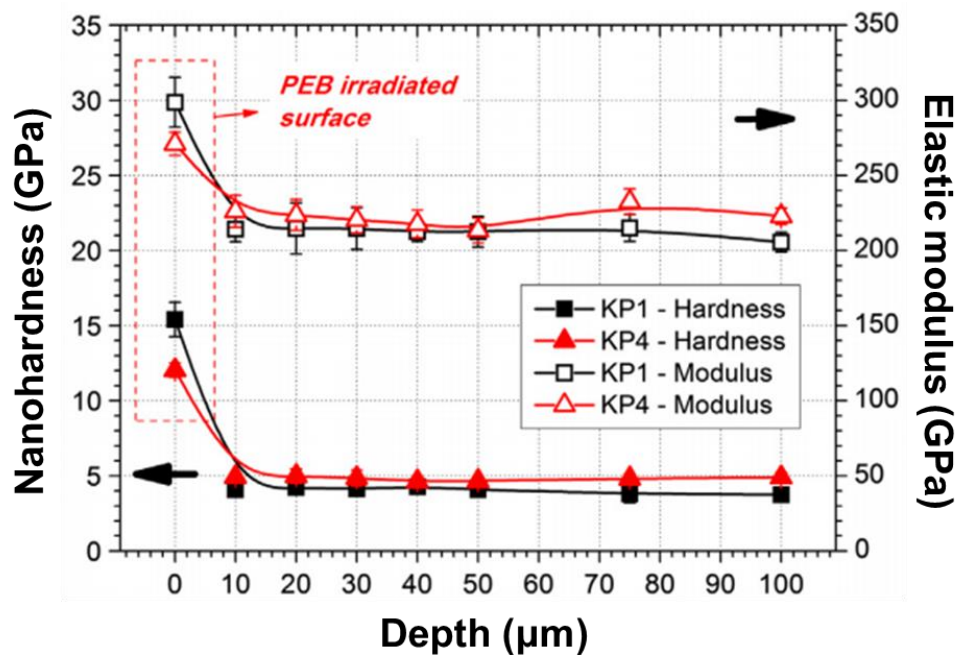


Figure 16. Nano-hardness and elastic modulus as a function of depth on the LPEB-irradiated KP1 and KP4 samples

An increase in the hardness and elastic modulus are expected to result in a change in the wear resistance. Figure 17 shows the normalized weight loss following wear tests on the surface of the KP1 and KP4 samples before and after LPEB irradiations. The weight loss was decreased significantly for both KP1 and KP4 following the LPEB irradiation. The weight loss of the untreated KP1 sample was 0.01 g, whereas the weight loss was 0.009 g following LPEB at an energy density of 7 J/cm², and 0.002 g at an energy density of 10 J/cm². The weight loss of the untreated KP4 sample was 0.014 g, which decreased to 0.003 following LPEB at an energy density of 7 J/cm² or 10 J/cm².

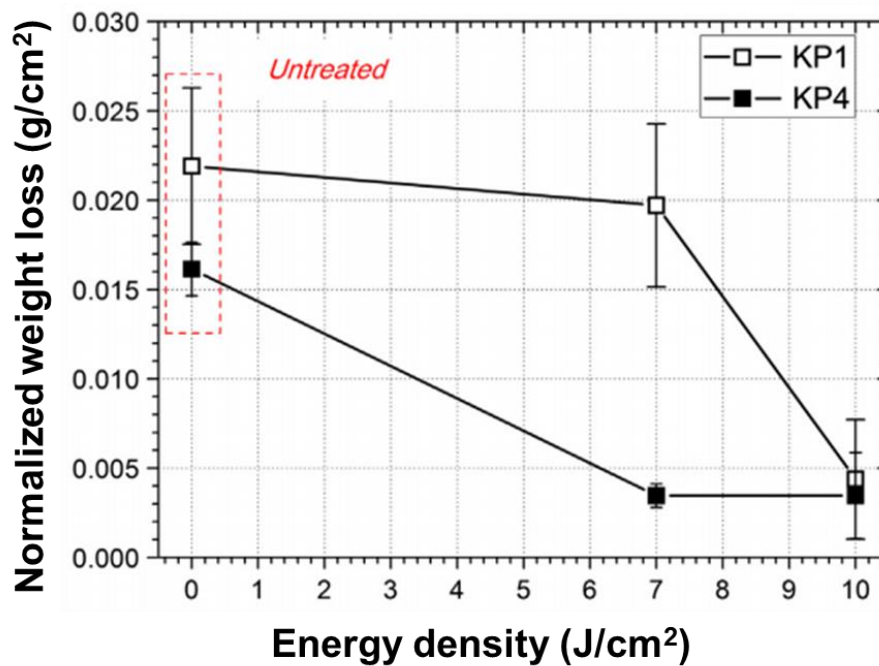


Figure 17. Normalized weight loss following pin-on-disc wear tests on the LPEB-irradiation KP1 and KP4 samples

The 3D profile and optical microscopy images of the wear track at the surface following the wear tests are shown in Figure 18. On the surface of the untreated KP1 sample, the rotating pin has created a 43- μm -deep wear track, whereas the wear track was only 2 μm deep following LPEB irradiation. The untreated KP4 sample exhibited a 125- μm -deep wear track, whereas the KP4 sample that had undergone LPEB had a wear track that was only 3.35 μm deep. Additionally, it appears that the wear mechanism was changed following the LPEB irradiation. Following sliding wear tests, materials can be deformed both elastically and plastically under shear stress. On the untreated samples (with a lower hardness and elastic modulus), attachment of wear debris to the wear track was observed (see Figure 18(b) and (f)), indicating an adhesive wear mechanism. However, following LPEB irradiations, as shown in Figure 18(d) and (h), some areas of the surface were not worn out or deformed at all. It follows that the wearing pin did not overcome the yield strength of the LPEB-treated KP1 and KP4 samples due to the increased hardness and elastic modulus. Thus, the wear mechanism of the LPEB-treated surface was dominantly abrasive. Furthermore, since the hardness of the LPEB-treated surfaces was large, the SKD11 pin might have been worn out during the wear test, as evidenced by the wide scars observed on the LPEB-treated KP1 sample shown in Figure 18(d).

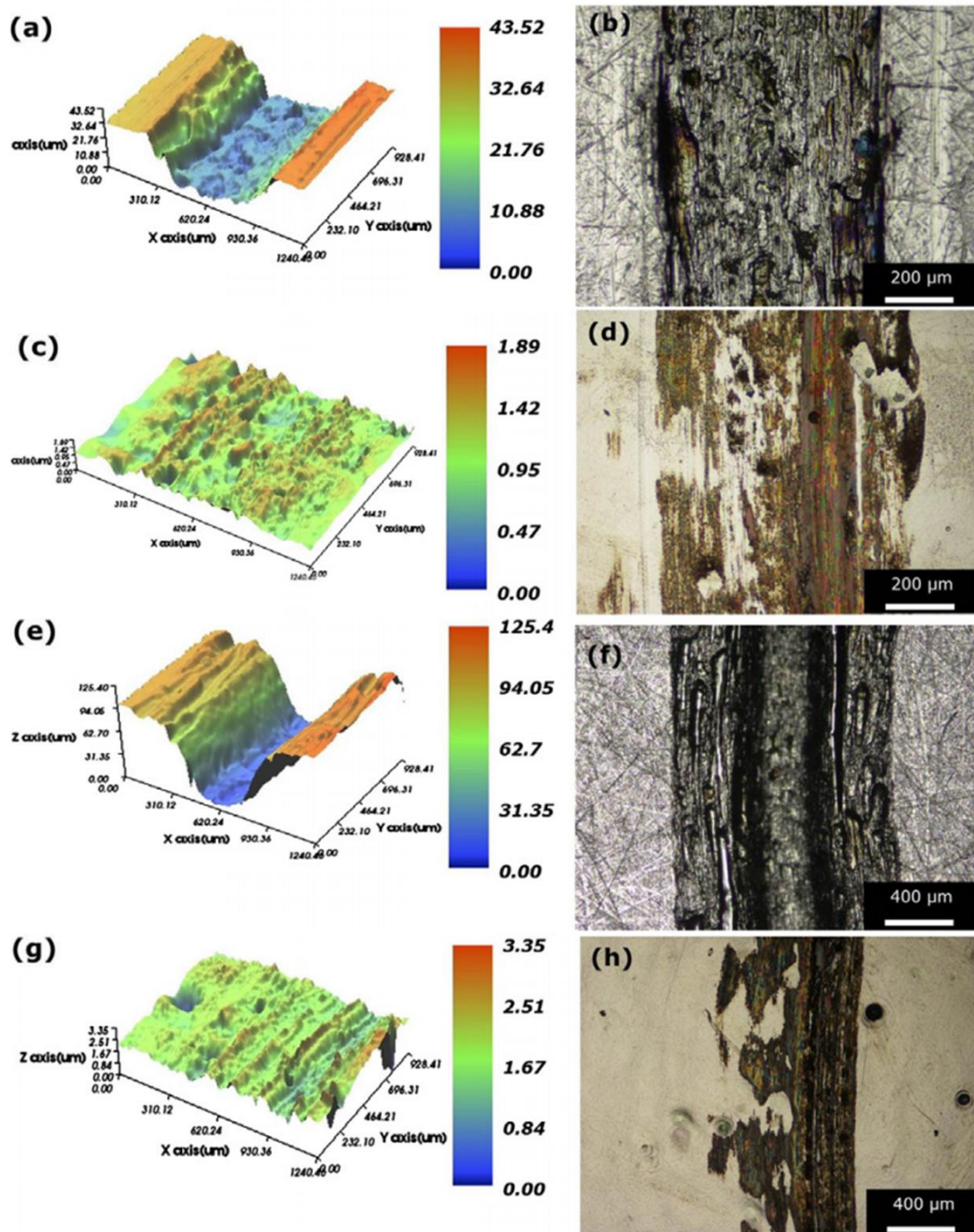


Figure 18. 3D surface profiles and optical microscopy images of the wear tracks formed on (a and b) untreated KP1, (c and d) LPEB-treated KP1, (e and f) untreated KP4, and (g and h) LPEB-treated KP4

4.1.4 Chemical properties

The chemical stabilities on the LPEB-irradiated surface could be simply represented by the corrosion resistance as the corrosion reaction is one of the most representative electrochemical reactions. Electrochemical analyses were carried out by potentiodynamic polarization (PDP) test using a standard three-electrode cell in 1% NaCl solution to investigate the effects of the re-solidified layer on corrosion

resistance of the LPEB-irradiated KP1 and KP4 samples. A standard calomel electrode (SCE) was used as the reference electrode, and a platinum electrode was used as the counter electrode. The exposed area of the surface of the working electrode was 1 cm². The surface of each sample was exposed to the solution for 30 min prior to the commencement of potentiodynamic polarization test to achieve a stable open-circuit potential (OCP). The potentiodynamic polarization tests were then carried out at a scan rate of 1 mV/s and in the range of ± 400 mV/SCE with respect to the OCP.

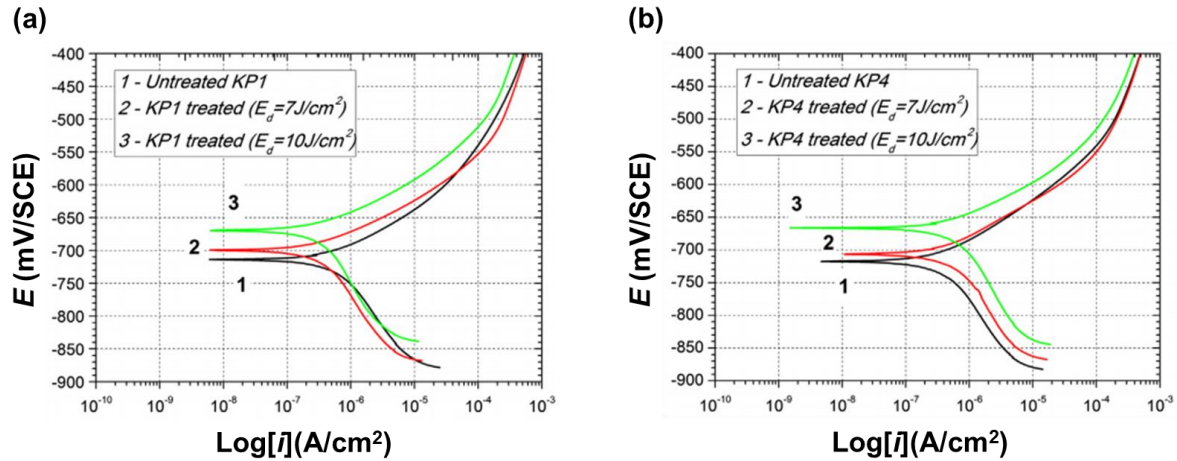


Figure 19. Potentiodynamic polarization curves of the LPEB-treated surface on (a) KP1 and (b) KP4

Table 5. Corrosion potentials, corrosion current densities, and corrosion rates for KP1 and KP4 before and after the LPEB irradiation

Materials	Energy density (J/cm ²)	E_{corr} (mV/SCE)	i_{corr} ($\mu\text{A}/\text{cm}^2$)	Corrosion rate (mm/y)
KP1	Bare	-725.4 ± 5.2	0.8122 ± 0.12	0.01873
	7	-685.8 ± 14.6	0.5145 ± 0.13	0.01153
	10	-661.0 ± 11.8	0.2394 ± 0.09	0.00552
KP4	Bare	-681.8 ± 11.5	0.7320 ± 0.09	0.01688
	7	-664.1 ± 7.4	0.4877 ± 0.17	0.01125
	10	-656.0 ± 9.8	0.3510 ± 0.02	0.00809

Figure 19 shows the potentiodynamic polarization curves of KP1 and KP4 before and after the LPEB irradiation. The Tafel extrapolation method was used on the curves to calculate the corrosion potentials E_{corr} and corrosion current densities i_{corr} . The corresponding corrosion potentials and current densities are shown in Table 5. The corrosion resistance of the irradiated surfaces was modified, as indicated by the shift in E_{corr} towards more noble potentials and a decrease in i_{corr} . The corrosion potential is strongly related to the activation energy for corrosion, and the active region of the corrosion process occurs at a nobler potential than the equilibrium potential [79]. Thus, a nobler corrosion potential following the LPEB, when compared to that of bare materials, is indicative of an increase in corrosion resistance. The

shift in the corrosion potential towards more noble potentials following the LPEB irradiations was larger, with an energy density of 10 J/cm² when compared to those obtained at 7 J/cm². The largest change in the corrosion potential was observed for the KP1 sample at an energy density of 10 J/cm² for 20 irradiation cycles, which caused the corrosion potential to shift from -725 mV/SCE to -661 mV/SCE. This improvement in corrosion resistance was almost twice as larger for the KP1 sample than for the KP4 sample. Prior to LPEB irradiations, the KP4 sample exhibited a nobler corrosion potential than KP1. However, following the LPEB irradiation, the corrosion potentials of the two treated samples were almost identical.

The corrosion current density was decreased following LPEB; the larger the energy density of the irradiating beam, the lower is the corrosion current density. The corrosion rate can be calculated using the equation (24) [80]:

$$v = \frac{i_{corr} k M}{2dA} \tag{24}$$

where k is a constant, M is the molar mass, d is the density, and A is the area of the electrode. With the exception of the corrosion current, the other parameters were constant in all tests. The corrosion rates calculated from different potentiodynamic polarization data are summarized as a function of energy density applied in Table 5. It is evident from Table 5 that the corrosion rate is decreased following the LPEB irradiation because the corrosion rate is proportional to the corrosion current density.

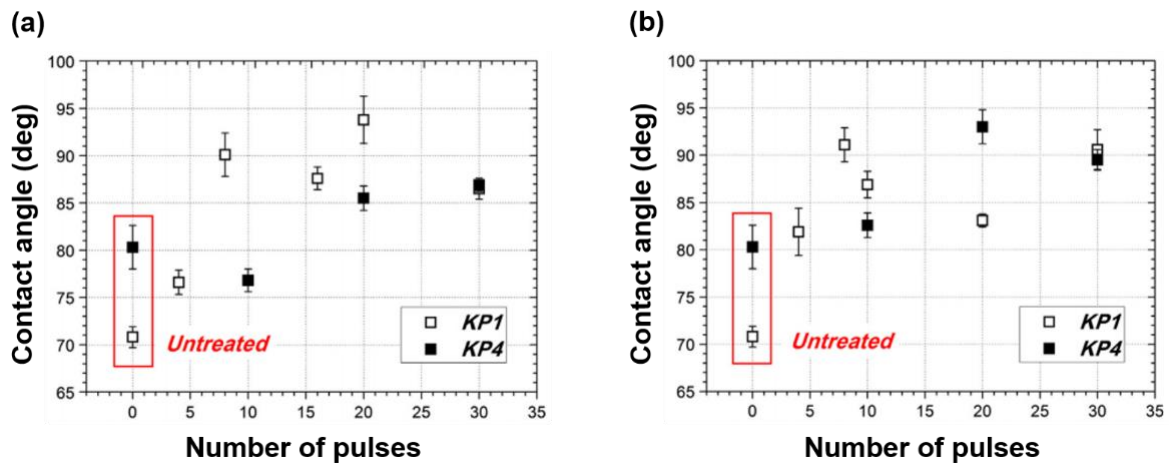


Figure 20. Contact angle before and after the LPEB irradiation on both the KP1 and KP4 samples with an energy density of (a) 7 J/cm² and (b) 10 J/cm²

This modification of the corrosion resistance is related to the surface energy. A larger activation energy for corrosion corresponds to better corrosion resistance. The surface energy can be characterized

using contact angle measurements [81]. Typically, a large contact angle corresponds to a low surface energy and also indicates a low reactivity at the surface [82]. Figure 20 shows the change in the contact angles of deionized water on the samples before and after the LPEB irradiation. With an energy density of 7 J/cm^2 , the contact angle of the KP1 sample was increased markedly following irradiation; however, the change in the contact angle of the KP4 sample was much smaller than KP1. This is in good overall agreement with the variation in the corrosion potential before and after the LPEB irradiation. The corrosion potential of KP1 was initially lower than that of KP4, and the two became similar following LPEB irradiations, as shown in Table 5. Similarly, the contact angle of the KP1 sample was initially smaller than that of the KP4 sample; however, the two became more or less similar following the LPEB irradiation. Considering these results, it can be concluded that the surfaces of both the KP1 and KP4 samples (and especially the KP1 sample) were stabilized following the LPEB irradiation.

Another possible explanation for the improvement in corrosion resistance is the production of an established metal oxide on the re-solidified surface [83, 84]. It has been established that passivating films, such as metal oxides on the surface of a bulk metal, may inhibit corrosion, since the oxidation process cannot readily progress on the oxidized layer [85]. Thus, the potential at which the passive films became unstable, as indicated by an increase in the current density, which occur at a nobler potential when compared with the bare material [86]. The elevated temperatures during the formation of the re-solidified layer may lead to a stable oxide layer [87, 88]. Figure 21 shows EPMA data for the cross-sectional area of the KP1 and KP4 samples following the LPEB irradiation. The fraction of oxygen on the re-solidified layer was significantly increased, as indicated by the higher counts for the corresponding electrons from the EPMA measurements. This is consistent with the results of the potentiodynamic polarization tests, contact angle measurements, and EIS results. An increase in the fraction of oxygen on the re-solidified layer after the LPEB irradiation may induce a more passive film composed of metal oxides. The re-solidified layer on the LPEB-treated surface exhibited a nobler corrosion potential than the untreated surface.

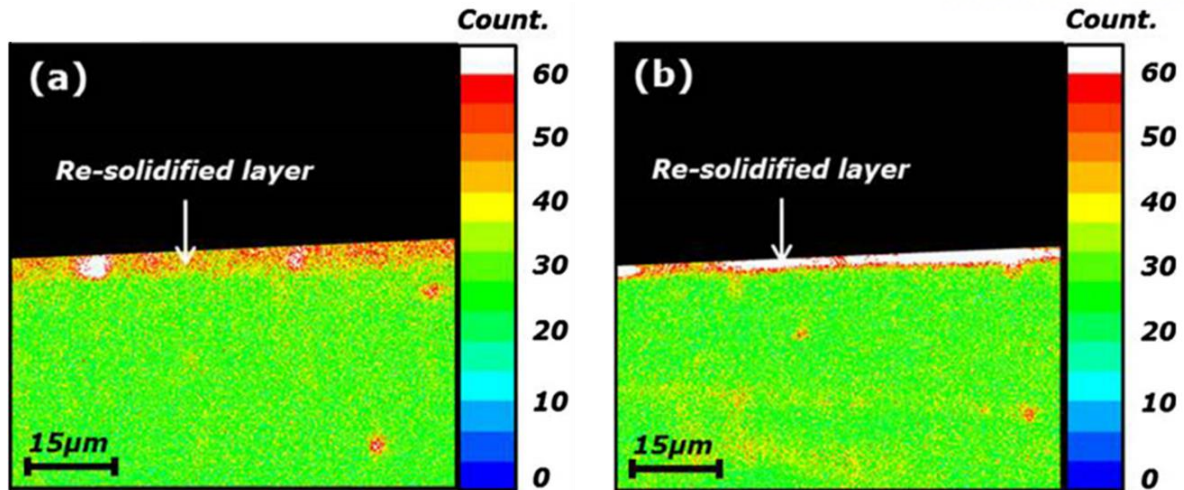


Figure 21. EPMA results showing the distribution of oxygen on the cross-sectional area of (a) KP1 and (b) KP4 following the LPEB irradiation

The EIS spectra were plotted from electrochemical impedance measurements at frequencies in the range of 100 kHz–100 MHz at the OCP. The amplitude of the signal was 10 mV. The result was plotted in Nyquist plots to compare the charge transfer resistance among samples treated by LPEB. Nyquist plots resulting from the EIS measurements strongly indicate an increase in corrosion resistance of the LPEB-treated surface. Based on the semi-circular Nyquist plots, we could infer the Ohmic behavior. The difference between the real and imaginary impedance components at low and high frequencies represents the charge transfer resistance. Thus, the corrosion resistance of the passive re-solidified layer can be compared based on the diameter of the semi-circles on the Nyquist plots.

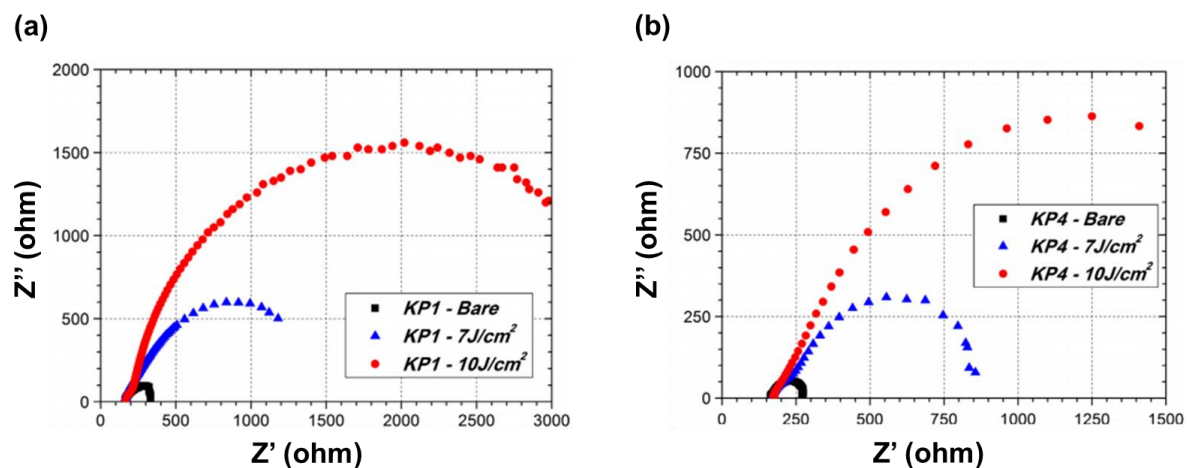


Figure 22. Nyquist plots for (a) KP1 and (b) KP4 before and after the LPEB irradiation

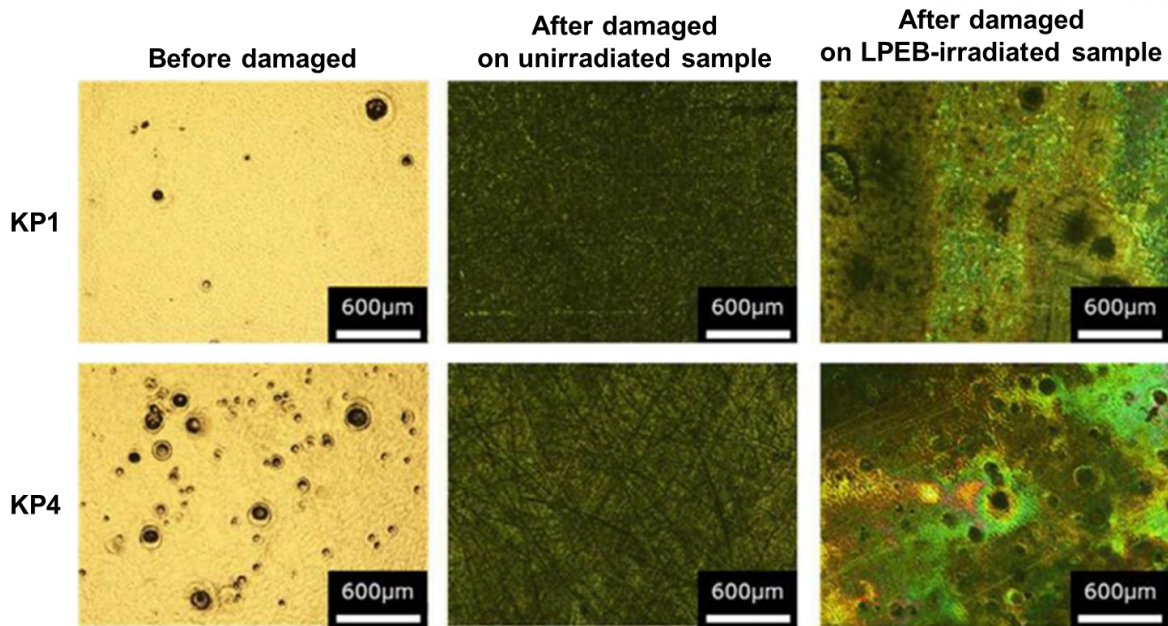


Figure 23. Optical micrographs of the corrosion-damaged surface morphology of the bare and LPEB-treated surfaces

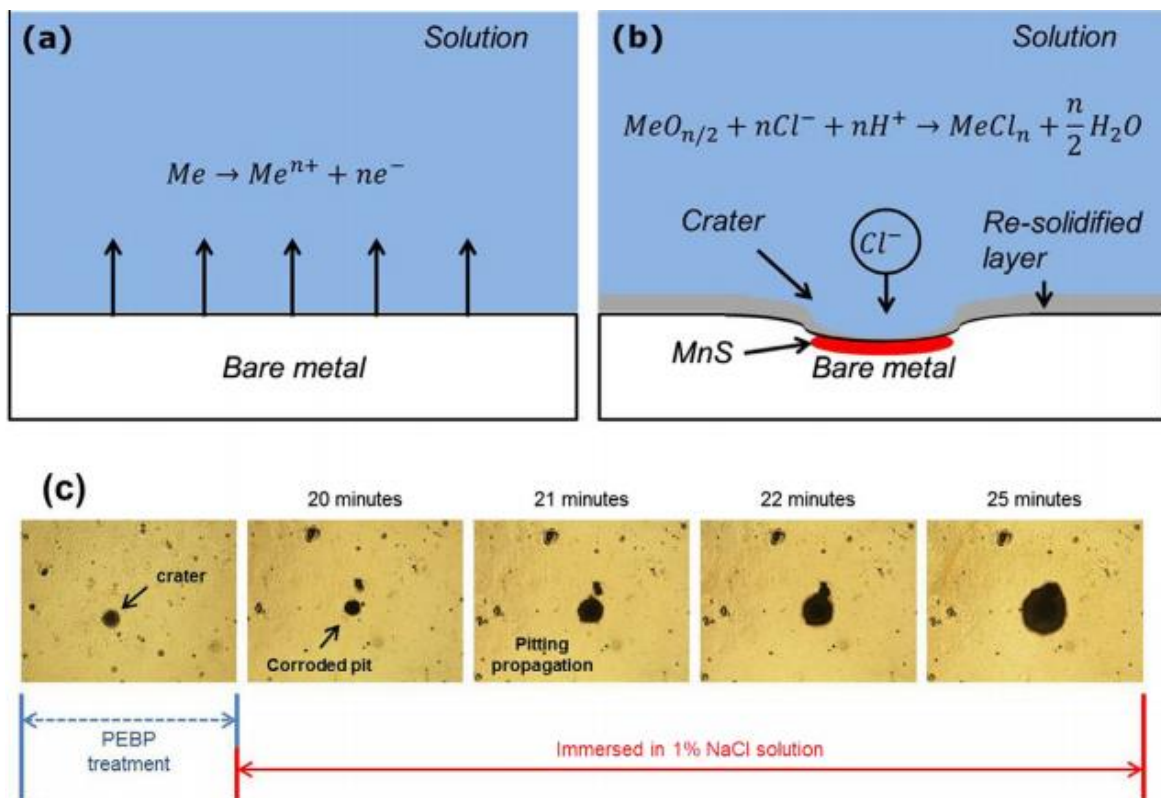


Figure 24. Illustration of the corrosion mechanism on the surface: (a) untreated, (b) following the LPEB irradiation, and (c) progressive pitting corrosion around the crater on the LPEB-irradiated surface

Figure 22 shows the Nyquist plots of the KP1 and KP4 steels before and after the LPEB irradiation. A comparison of the diameters of semi-circles in the Nyquist plots indicates that LPEB irradiations

dramatically increased the charge transfer resistance of the surfaces of both the KP1 and KP4 samples. The increase in the charge transfer resistance was larger, at an energy density of 10 J/cm² when compared to those obtained at 7 J/cm². It follows that the LPEB irradiation induces a passive re-solidified layer on the surface of KP1 and KP4 samples, thereby increasing their corrosion resistance in NaCl solution. The improvement in corrosion resistance can also be clearly seen in the optical microscopy images shown in Figure 23. As the number density of craters on the surface of KP4 was larger than that of KP1 (see Figure 15), more corroded pits were observed on the LPEB-treated surface of KP4 than KP1. Rust resulting from corrosion was significantly reduced following the LPEB irradiations for both steels. In addition, the corrosion that occurred on the LPEB-treated surface was concentrated around the craters. As shown in Figure 24, corrosion was initiated around the crater and propagated from there. The re-solidified layer above the craters was generally much thinner than in other areas because LPEB irradiations creates molten pools around non-metallic precipitates due to partial melting and evaporating processes. This thin film can readily be degraded chemically, particularly in a solution that contains chloride ions [89]. Once a localized region of the re-solidified layer on the LPEB-treated surface has been destroyed by corrosion, this site becomes an anode, and the areas around it becomes a cathode. Around the craters, therefore, the remaining MnS inclusions are much more susceptible for corrosion than steel, and hence the corrosion becomes concentrated around the breaks in the re-solidified layer near craters in this film, while the other areas are under cathodic protection [90]. Thus, the corrosion mechanism is governed by pitting corrosion around the craters, which can be described as [91]:



The corrosion mechanism is summarized in Figure 24 [92]. This is consistent with the difference in the density of pits observed on the surface of KP1 and KP4 samples. Because the density of the surface craters was higher for the KP4 sample, more pits were observed on the surface of the KP4 sample following the LPEB irradiation and corrosion reaction, as shown in Figure 23. Increasing the energy density and number of irradiation cycles induced a greater level of corrosion resistance. This behavior may be attributed to oxidation of the surface, resulting in the formation of a passivation layer. Furthermore, a large number of irradiation cycles could eliminate the craters and harmful inclusions, such as MnS and carbides, which facilitates corrosion, due to repeated melting and evaporation.

4.1.5 Microstructure

The modifications on mechanical and chemical properties following the LPEB irradiations are highly related to the possible phase transformation on the re-solidified layer. As the heating and cooling rates during the irradiation are extremely rapid, a phase transformation and amorphization of steels might occur at the surface. Thus, the microstructural analysis on the re-solidified layers were performed to clearly specify the surface modification mechanisms on mold steels.

There are a number of competing factors that can affect the hardness after the LPEB irradiation. One of the them is the residual tensile stress [92]. If a martensitic transformation occurs below the surface, it could induce tensile residual stress at the surface and reduces the hardness of the material [93]. In contrast, a large dislocation density generated at the surface of a material after the LPEB irradiation may lead to hardening of the surface [94]. To investigate the presence of such phase behavior, image quality maps (IQMs) of EBSD data were collected; the resulting images are shown in Figure 25.

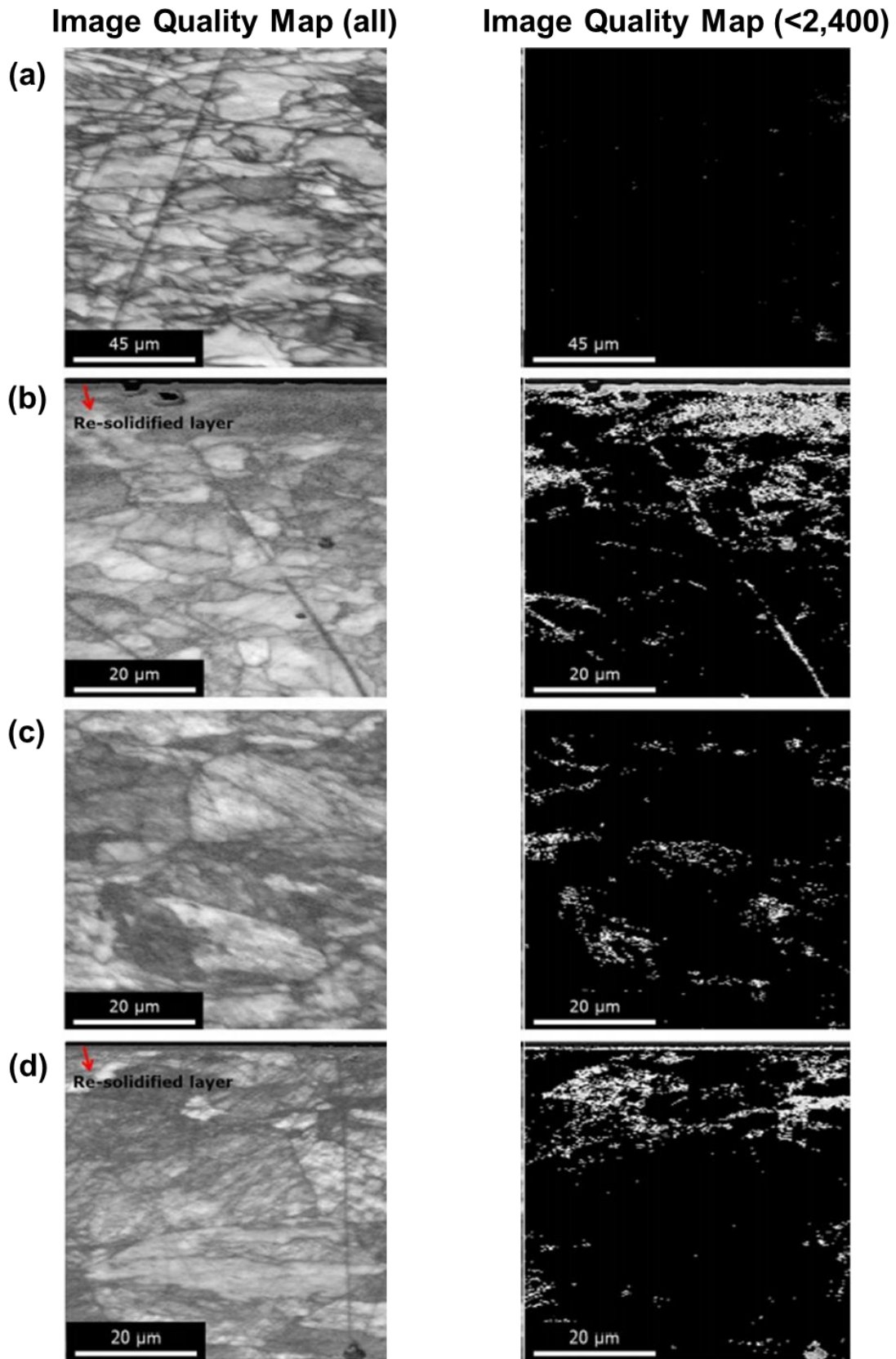


Figure 25. IQMs from the EBSD analysis on the cross-sectional area: (a) untreated KP1, (b) LPEB-treated KP1, (c) untreated KP4, and (d) LPEB-treated KP4

During rapid cooling, carbon atoms cannot diffuse out of the crystal structure, and the resulting shear deformation produces condensed dislocations; this is a primary strengthening mechanism for steels. The quality of the electron diffraction patterns was defined using the ‘image quality factor’ (IQF) of the region; it was lower on the LPEB-treated samples. It is possible to specify the dislocation density using the IQF. The left column in Figure 25 shows all the IQMs, and the right column shows only images that are characterized by an IQF less than the average IQF of other areas of the sample. Condensed dislocations emerged on the LPEB-treated surface of both the KP1 and KP4 samples. However, phase transformations in the sub-surface were not observed. Thus, residual tensile stress is not expected at the surface following the LPEB irradiation. The lower IQF of the LPEB-treated surfaces corresponds to a larger density of dislocations, and therefore we may expect that the hardness of a specific region is proportional to the density of the dislocations [94]. Comparing Figure 25(b) and (d), the thicker regions contain a larger density of dislocations on the LPEB-treated surface and the density of dislocations were higher for the KP1 sample than on the KP4 sample. An increased carbon fraction in the KP1 sample might have contributed to a higher dislocation density. Carbon atoms that did not diffuse during the rapid cooling have led to the formation of a distorted matrix combined with metal atoms, resulting in a large density of dislocations at the surface. Accordingly, the larger fraction of carbon in the KP1 sample could have caused a larger density of dislocations at the surface. The thermal diffusivity of KP1 is larger than that of KP4, which leads to a more rapid cooling rate of KP1 during the LPEB irradiation, and consequently, only a shorter time was available for carbon atoms to diffuse. The results of the nano-indentation tests are consistent with the IQM analysis of the EBSD data. The hardness of the KP1 surface was greater than that of the KP4 surface following the LPEB irradiation, even though the converse relationship was observed prior to the LPEB irradiation. Thus, it can be concluded that the major factor leading to the increased hardness of both KP1 and KP4 steels following LPEB irradiations is due to an increase in dislocation density following the phase transformation during re-crystallization.

To investigate the phase transformation, which can affect the corrosion resistance, X-ray diffraction (XRD) patterns were obtained following the LPEB irradiation. Figure 26 shows the XRD patterns of KP1 following LPEB irradiations as a function of irradiation cycles. The peaks corresponding to α -phase and γ -phase steel were identified on each peak [95]. The XRD pattern of bare KP1 showed peaks all indicating α -phase. After the LPEB irradiation for 5 irradiation cycles, the strongest peaks were still α -phase steel. However, with more than 10 irradiation cycles, the largest peak for KP1 was changed to a γ -phase peak. The fraction of the α -phase peak was continuously decreased with an increase in the number of irradiation cycles. Due to rapid melting and re-solidification during the LPEB irradiation, phase transformation to γ -phase could occur with undissolved carbon atoms in the matrix. It has been established that the corrosion resistance could be effectively modified with an austempering process by increasing the fraction of retained austenite in the material [96]. Also, the effect of the α/γ -phase ratio on the corrosion resistance has been studied, and results proved that increasing the γ -phase could

improve the corrosion resistance [95, 97]. Thus, the increased fraction of retained austenite in the matrix may be responsible for the modification of the corrosion resistance of the LPEB-treated surface of KP1 and KP4.

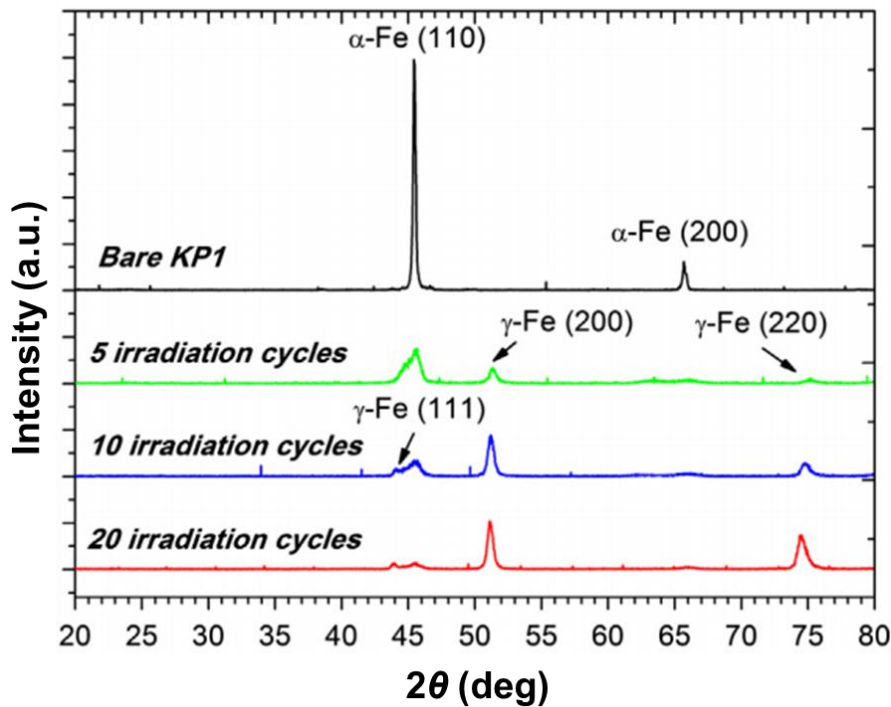


Figure 26. XRD patterns obtained from the surface of mold steels before and after the LPEB irradiation

4.2 Surface modification of biomedical alloys

In addition to the engineering metallic alloys, the LPEB irradiation is also applied on the surface modification of a biomedical material, Ti-6Al-7Nb, which is one of the most superior materials in the field of dental and orthopedic implant surgery [50]. In early generations of implants, Co-Cr alloys and Ti-6Al-4V (Grade 5) were the most commonly used materials due to their favorable hardness, strength, and resistance to wear and corrosion. However, their limitations were clear that Co-Cr alloys are prone to fracture as they are brittle, and Ti-6Al-4V leads a formation of vanadium oxide in simulated body fluid, which makes it cytotoxic [98]. Ti-6Al-7Nb is similar to Grade 5 in terms of its mechanical properties including hardness and modulus. However, replacing vanadium with niobium is expected to enhance biocompatibility since niobium oxide is non-toxic and non-allergic [99]. Despite the potential benefits of Ti-6Al-7Nb in biomedical applications, there has been very little investigations of possible surface modifications to improve the biocompatibility and mechanical properties. In this context, the LPEB irradiation could be a good candidate for the biomedical material that it is highly purified process only using electrons as the power source without generating any types of cytotoxic chemicals and/or byproducts. The extruded rod of Ti-6Al-7Nb is used for the LPEB surface modification process. The

diameter of the rod is 25 mm, which is cut into 5-mm-thick slices. The chemical composition of Ti-6Al-7Nb is summarized in Table 6.

Table 6. Chemical composition of Ti-6Al-7Nb

	Ti	Al	Nb	Fe	Ta	O	N
Fraction (wt. %)	85.5	6	7	0.25	0.5	0.2	0.05

The conditions of LPEB irradiations were set to be the same that applied on the mold steels. In case of Ti-6Al-7Nb, the irradiation was carried out at the center of the samples as the diameter of the circular samples was 25 mm, which is sufficient to provide a uniform coverage by the 60-mm-diameter electron beam.

4.2.1 Formation of the re-solidified layer

Figure 27 shows the optical images of the surface of Ti-6Al-7Nb before and after the LPEB irradiation. As shown in the Figure 27, the glossiness of the surface was enhanced further with reduced surface roughness erasing surface scratches following the repeated melting and re-solidification processes. Figure 28 shows the cross-sectional SEM images of the untreated and LPEB-irradiated Ti-6Al-7Nb alloy samples obtained using various energy densities and number of pulses. As shown in Figure 28(a) and (b), at an energy density of 7 J/cm², the depth of the re-solidified layer was 5.83 μm after five pulses, and 6.41 μm after ten pulses. At an energy density of 10 J/cm², the depth of the re-solidified layer was 7.45 μm after five pulses, and 7.99 μm after ten pulses, as shown in Figure 28(c) and (d). The depth of the re-solidified layer was more strongly dependent on the pulse energy than on the number of pulses.

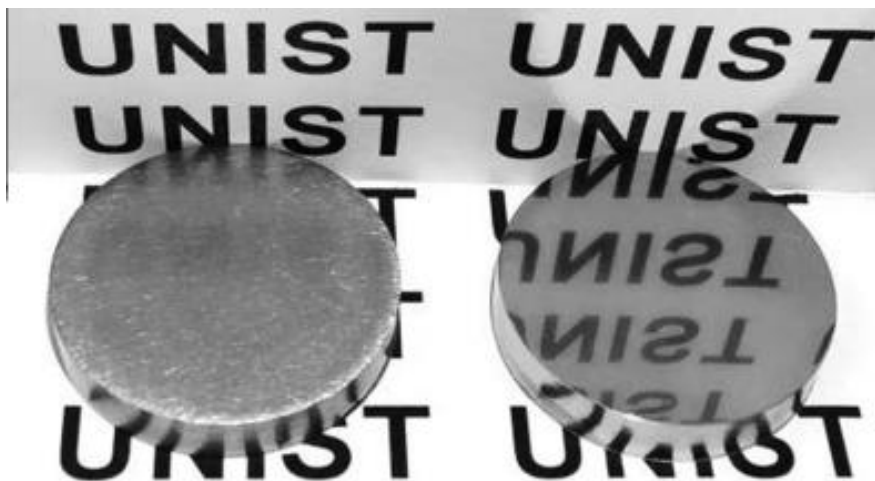


Figure 27. Optical photographs showing the surface texture of Ti-6Al-7Nb before (left) and after (right) the LPEB irradiation

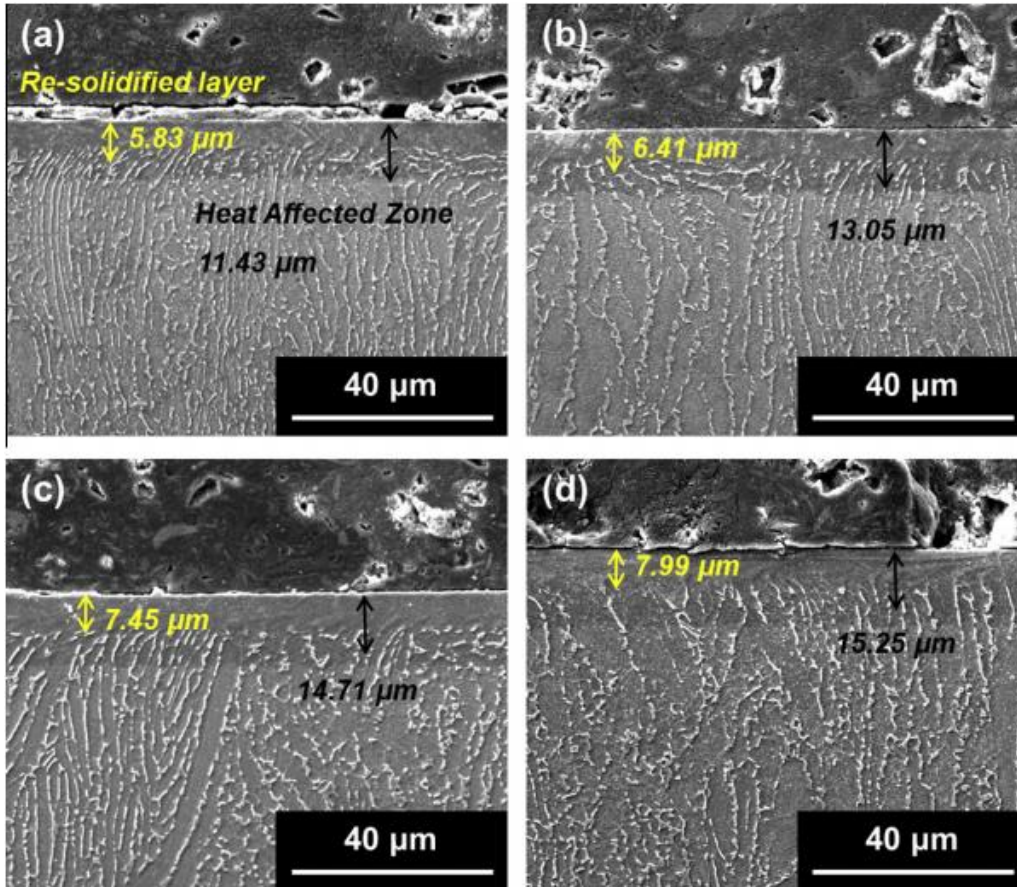


Figure 28. Cross-sectional SEM images of the Ti-6Al-7Nb after the LPEB irradiation at (a) 7 J/cm² for 5 pulses, (b) 7 J/cm² for 10 pulses, (c) 10 J/cm² for 5 pulses, and (d) 10 J/cm² for 10 pulses

4.2.2 Mechanical properties

Figure 29 shows the nano-hardness of LPEB-treated Ti-6Al-7Nb samples as a function of the depth from the surface to the bulk. The surface nano-hardness was 4 GPa for the bare surface, which increased to 10.14 GPa after LPEB irradiation at an energy density of 7 J/cm². With an energy density of 10 J/cm², the nano-hardness at the surface was 8.37 GPa. For the LPEB-irradiated samples, the nano-hardness was greatest near the surface, and approached that of the untreated alloy further from the surface.

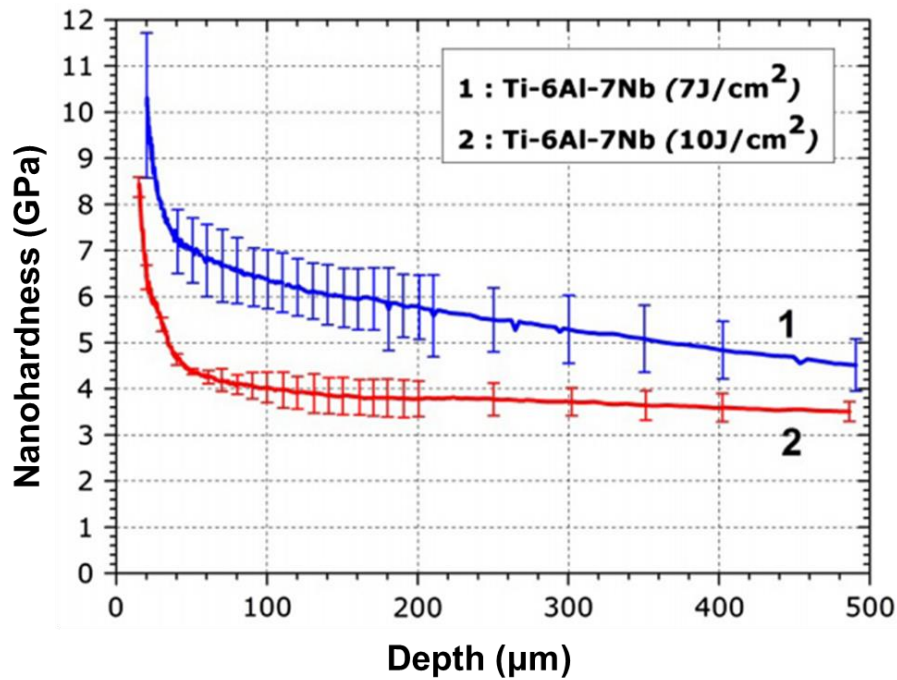


Figure 29. Nano-hardness as a function of depth for the LPEB-treated Ti-6Al-7Nb samples

4.2.3 Chemical properties

Similar to the investigation on mold steels, the chemical stabilities on re-solidified layers with Ti-6Al-7Nb were also specified by the corrosion resistance. Figure 30 shows the representative potentiodynamic polarization curves of the untreated and LPEB-irradiated Ti-6Al-7Nb alloy. The corrosion potential and the corrosion current density were calculated using the potentiodynamic polarization curves by Tafel extrapolation method. The corresponding electrochemical parameters, including the polarization resistance and corrosion rate, are listed in Table 7 as a function of the irradiation energy density. The corrosion potential of the LPEB-treated surface was nobler than the bare surface. Among the treated ones, it was nobler for the samples treated at an energy density of 10 J/cm² than 7 J/cm². As listed in Table 7, the largest increase in the corrosion potential was obtained for the Ti-6Al-7Nb alloy sample treated at an energy density of 10 J/cm².

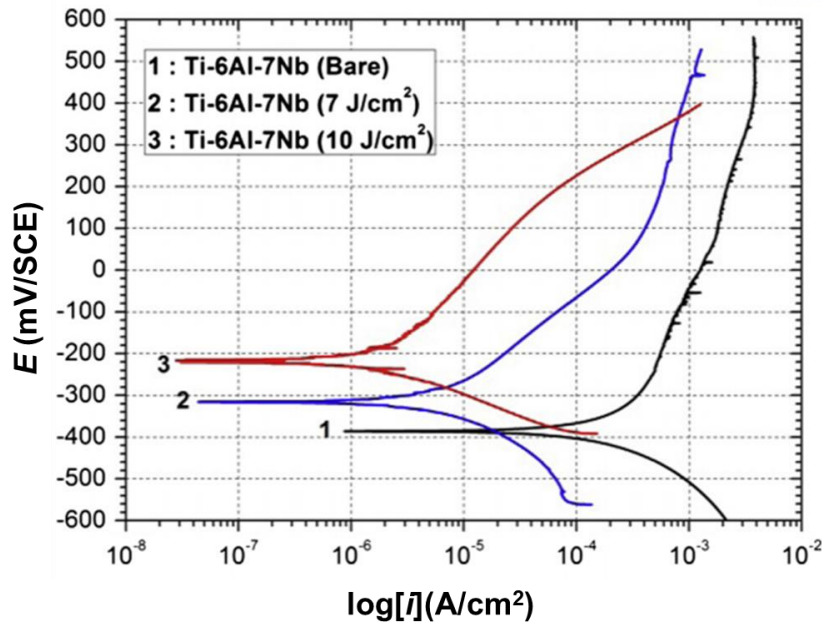


Figure 30. Potentiodynamic polarization curves of the LPEB-irradiated Ti-6Al-7Nb

Table 7. Polarization electrochemical parameters of Ti-6Al-7Nb before and after the LPEB irradiation

Energy density (J/cm ²)	E_{corr} (mV/SCE)	i_{corr} (nA/cm ²)	β_c (mV/dec)	β_a (mV/dec)	R_p (M Ω cm ²)	Corrosion rate (mm/y)
Bare	-386.7 ± 9.34	80.07 ± 5.67	90 ± 10	84 ± 16	0.252 ± 0.005	1.3857
7	-337.7 ± 30.6	5.36 ± 1.78	125 ± 9	210 ± 7	4.805 ± 2.226	0.0928
10	-218.1 ± 3.82	1.08 ± 0.76	75 ± 9	127 ± 11	26.683 ± 13.241	0.0187

The corrosion current density is decreased significantly following LPEB treatment. Furthermore, the corrosion resistance may also be characterized from the variation of the polarization resistance following LPEB treatment. The polarization resistance is given by [100]

$$R_p = \left(\frac{\Delta E}{\Delta i} \right)_{\Delta E \rightarrow 0} \quad (28)$$

where ΔE is the variation in the applied potential around the corrosion potential and Δi is the change in the polarization current. The polarization resistance can be used as a measure of the corrosion resistance of the surface. The polarization resistance on the untreated surface of Ti-6Al-7Nb was 0.252 M Ω cm² and it was increased to 4.805 M Ω cm² following LPEB irradiation at an energy density of 7 J/cm² and increased further to 26.683 M Ω cm² at an energy density of 10 J/cm². Based on these electrochemical measurement, it can be concluded that the corrosion resistance of Ti-6Al-7Nb alloy is

increased following LPEB treatment.

Modifications to the corrosion resistance are related to the chemical composition of the surface. Similar to the mold steel, stable and passive oxide layers formed at the surface following LPEB irradiation might be responsible for the improvement in the corrosion resistance [101]. Under atmospheric conditions, the thickness of the native TiO_2 layer that forms at the surface of titanium alloys is several angstroms [102]. Such layers passivate the surface, protecting the underlying metal from dissolution and corrosion [103]. Figure 31 shows the spatial variation of the chemical composition of the Ti-6Al-7Nb samples following LPEB irradiation measured using EPMA. At the LPEB-irradiated surface, the total number of counts for electrons corresponding to oxygen almost doubled compared with the untreated surface, regardless of the energy density. The fraction of Ti and Al decreased at the LPEB-irradiated surface, and the fraction of Nb did not vary significantly. It follows that titanium oxide and aluminum oxide were formed in the re-solidified layer, and Nb was not significantly affected. The depth of the re-solidified layer containing the metal oxides was similar to the depth of the melted layer induced by the LPEB irradiation.

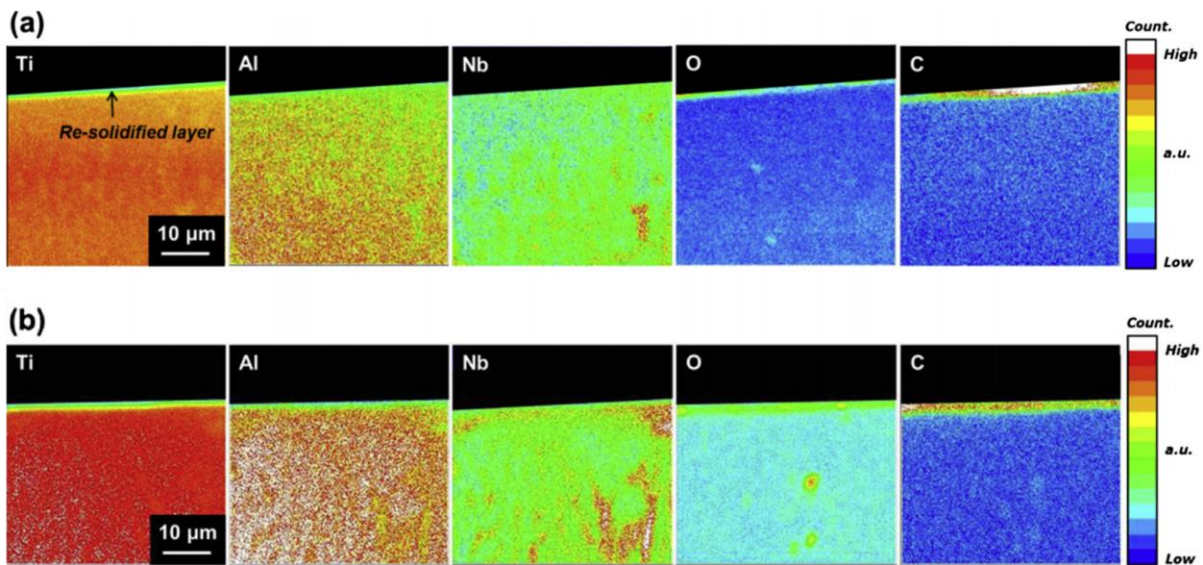


Figure 31. EPMA representing the distribution of chemical components on the cross-sectional area of Ti-6Al-7Nb following the LPEB irradiation with (a) 7 J/cm^2 and (b) 10 J/cm^2

Figure 32 shows XPS spectra of titanium and aluminum acquired at the surface of untreated and LPEB-irradiated Ti-6Al-7Nb alloy. The peaks for titanium and aluminum indicate the formation of TiO_2 and Al_2O_3 , both of which are passive metal oxides. One interesting observation is the formation of titanium nitride (TiN), which is widely used in surface treatments to improve the mechanical and chemical properties of titanium alloys [104]. During irradiation with the LPEB, nitrogen was used to flush the chamber between pulses to remove the evaporated gases. Some of these gases may be expected to remain in the chamber during the following pulse, and hence the nitrogen gas may react with the

liquid metal during melting and re-solidification. The formation of TiN at the surface following LPEB irradiation could be responsible for the improvement in corrosion resistance of LPEB-irradiated Ti-6Al-7Nb alloy.

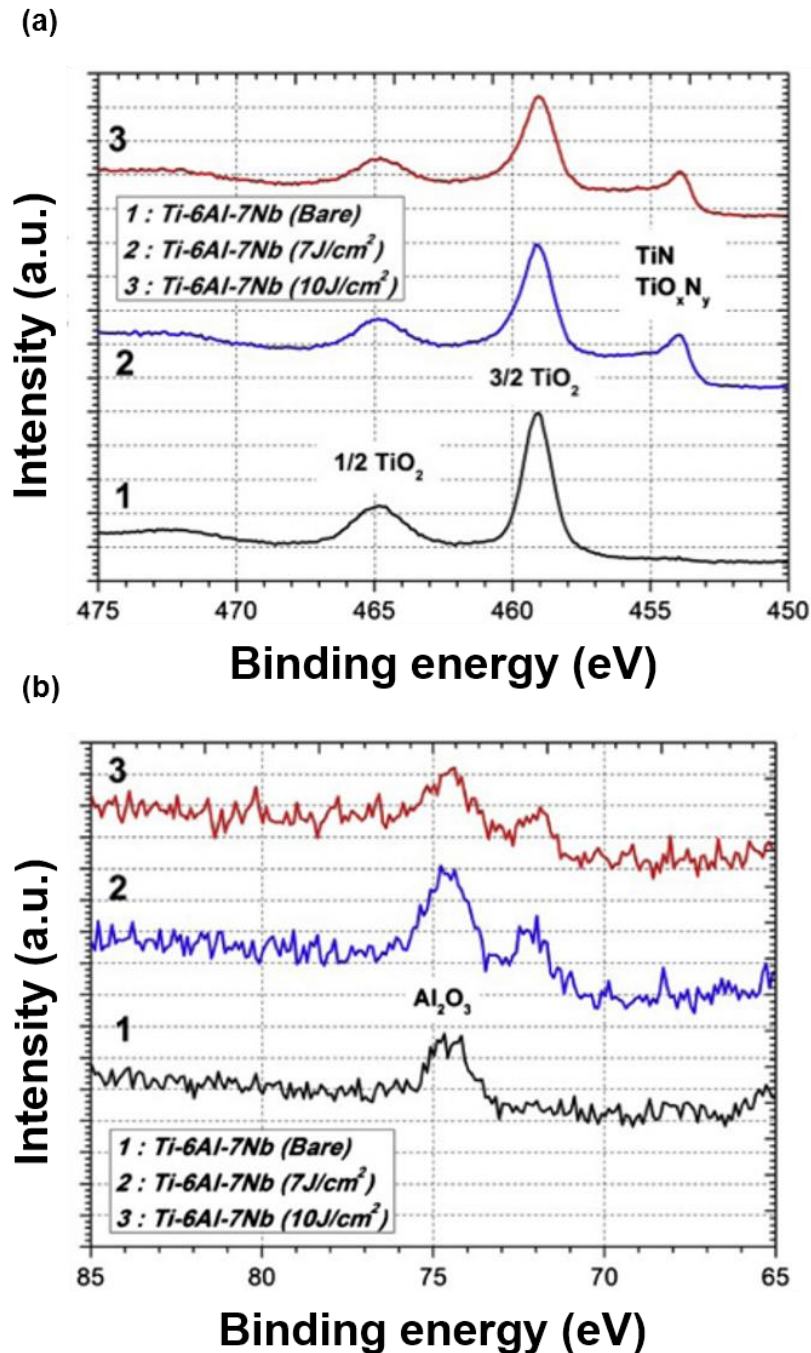


Figure 32. XPS spectra of untreated and LPEB-treated Ti-6Al-7Nb for (a) titanium and (b) aluminum

The corrosion-inhibiting effect of the passivation layer can be characterized by the charge transfer resistance obtained from a Nyquist plot of the EIS spectra [92]. The $\log(f)-|Z|$ plots of the EIS spectra

can be used to characterize the resistance to chemical reactions at the surface as a function of frequency. Figure 33(a) shows Nyquist plots and Figure 33(b) shows the $\log(f)-|Z|$ plots of the Ti-6Al-7Nb samples before and after irradiation with the LPEB. It is clear that the LPEB treatment increased the impedance of the surface, and that the increase in the impedance is larger at an energy density of 10 J/cm² than at an energy density of 7 J/cm². However, at an energy density of 7 J/cm², there was a reduction in the impedance at low frequencies when compared with that of the untreated sample. Hence, it can be concluded that the LPEB treatment enables the formation of a more chemically stable and nobler Ti-6Al-7Nb surface that is more resistant to corrosion than the untreated surface.

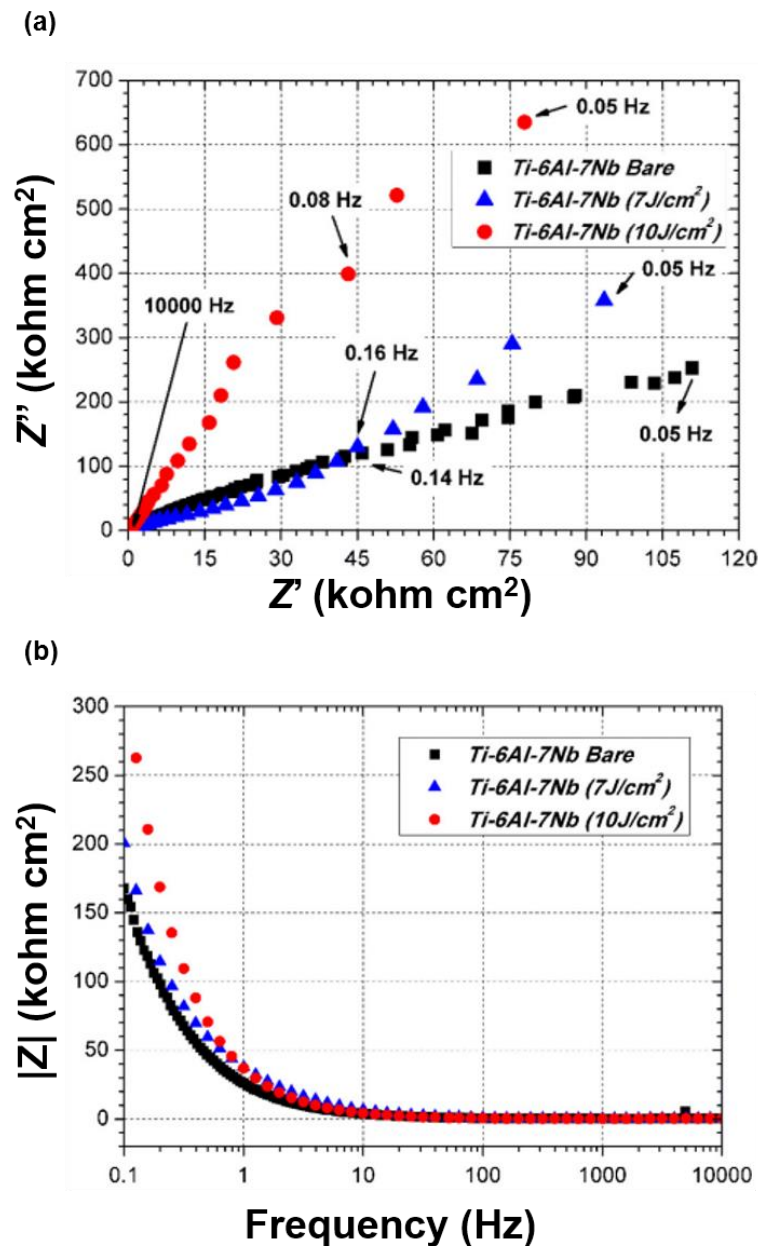


Figure 33. (a) Nyquist plots and (b) $\log(f)-|Z|$ plots of Ti-6Al-7Nb before and after the LPEB irradiation

4.2.4 Microstructure

The phase changes and microstructural modifications at the LPEB irradiated surface were investigated using XRD and SEM as they could influence the mechanical and chemical properties. During the LPEB irradiation process, the crystal matrix at the surface could become distorted, resulting in surface dislocations and twinning, both of which are well-known hardening mechanisms of metal alloys [94]. Figure 34 shows the magnified cross-sectional SEM images of the irradiated surfaces, which exhibited twin traces at the re-solidified region, both for energy densities of 7 J/cm^2 and 10 J/cm^2 . These twin traces are the evidence for the occurrence of a large density of dislocations at the surface following LPEB irradiation, which may be expected to lead to hardening of the surface. This is in good overall agreement with the distribution of carbon atoms at the surface following LPEB treatment, as shown in Figure 31: the carbon fraction at the re-solidified layer increased compared with the untreated material.

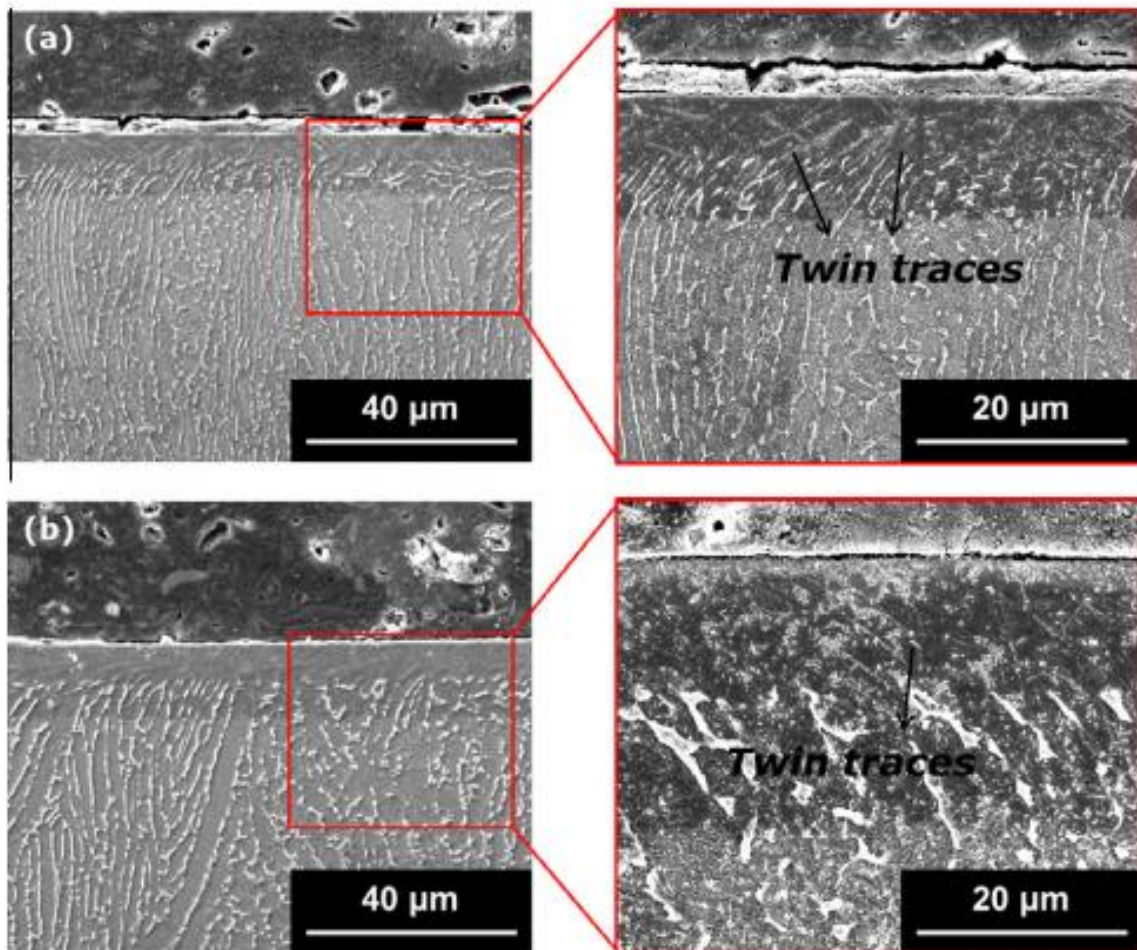


Figure 34. Cross-sectional SEM images showing twinning traces induced by the LPEB irradiation with an energy density of (a) 7 J/cm^2 and (b) 10 J/cm^2

In addition to the increased density of dislocations at the surface, the crystal planes were rearranged. The orientation of the crystal planes is strongly related to the hardness, and materials with crystalline

structures can be plastically deformed by slip processes. The XRD peaks shown in Figure 35, exhibit a significant decrease in the intensity of (100) and (101) planes following LPEB irradiation. The (101) plane is one of the dominant slip planes [105], and hence a reduction in the intensity of the (101) plane following LPEB treatment could lead to hardening of the surface, making it less easy for the material to be plastically deformed.

The change in intensity of the XRD peaks following LPEB treatment was also highly related to the variation in corrosion resistance. The intensity of the XRD peaks was more or less similar, irrespective of the electron beam irradiation conditions. Following the irradiation, a loss in crystallinity was observed, supported by the broadening of the diffraction peaks. Furthermore, there was a reduction in the intensity of the peaks corresponding to the β -phase. It is well known that the corrosion resistance of α -phase titanium is greater than that of the β -phase [106]. Hence, the phase transformation to α -phase may be responsible for the increased corrosion resistance. However, the fraction of β -phase in this alloy was very small prior to the LPEB irradiation, and so it does not expect that this phase transformation would have significantly affected the corrosion resistance.

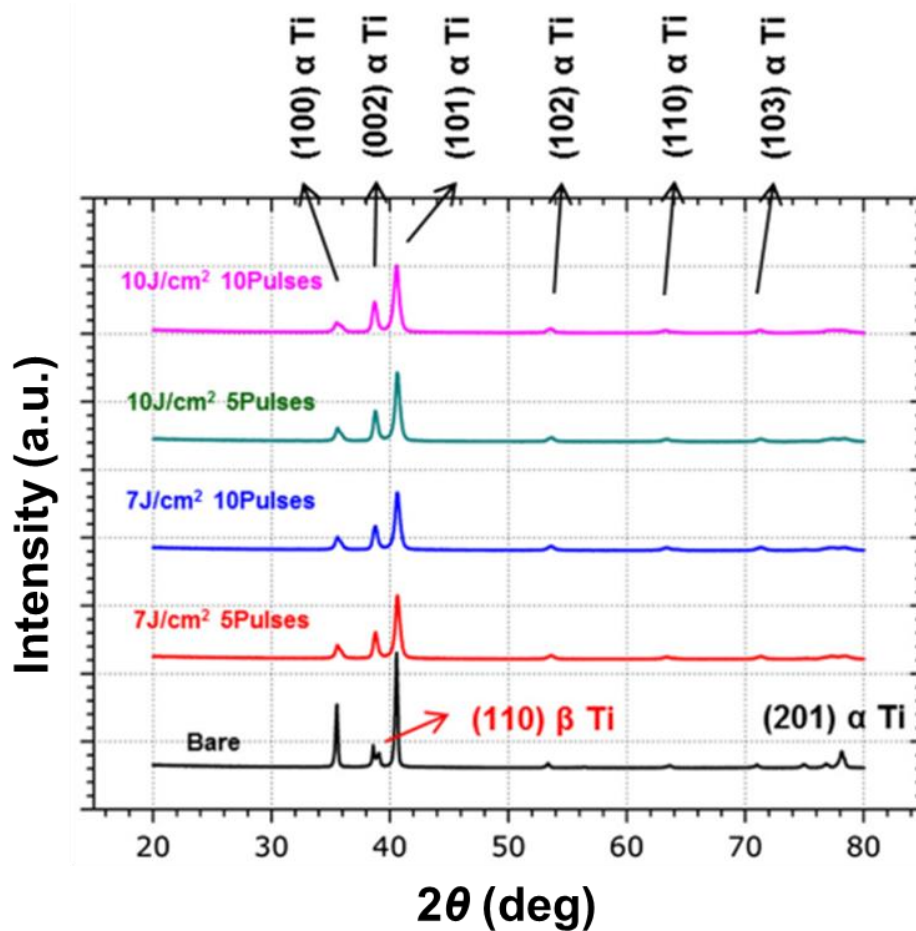


Figure 35. XRD patterns obtained from Ti-6Al-7Nb before and after the LPEB irradiation

It appears that the melted surface immediately following electron-beam irradiation was readily oxidized, forming a thicker passivation layer when compared to the native oxide layer. The EPMA data showed that this passive oxide layer consisted of TiO_2 , Al_2O_3 , and TiN , and the presence of these chemical species may be expected to increase the corrosion resistance of the metal. The larger increase in corrosion resistance observed for Ti-6Al-7Nb alloy treated at higher energy density could be attributed to the formation of a thicker re-solidified layer at the surface.

4.3 Nitriding process assisted by the LPEB irradiation

Although Ti-6Al-7Nb is a relatively biocompatible material, some fundamental problems still remain unsolved. Damage of the thin oxide layer (1 - 4 nm) could lead to the formation of galvanic cells. As Song [107] and Gu et al. [108] pointed out, mechanical properties of corrosion-resistant films have been one of the most important concerns on electrochemically stable surface layer. Remarkably, many studies have reported that titanium nitride (TiN), used as a hard ceramic coating material, offered an improved corrosion resistance with superior surface hardness [109].

According to previous results with LPEB irradiation on Ti-6Al-7Nb, it was found that corrosion resistance and nano-hardness were improved by LPEB. Additionally, small TiN segments were observed on the LPEB-treated surface. In this context, the LPEB irradiation showed its potential application on the nitriding process overcoming the limitations of previous nitriding methods such as surface defects and low uniformity. As the LPEB irradiation could be adopted as a polishing method, this can lead to a defect-free surface re-solidified layer following the irradiation process. However, nitrogen implantation was obviously small on the re-solidified with the standard LPEB irradiation. Thus, the experiments were designed to develop a crack-less nitriding process by combining a nitrogen ion implantation system using LPEB and a cathodic process to improve the corrosion characteristics and nano-hardness of Ti-6Al-7Nb. LPEB irradiation was performed using argon (Ar) and N_2 plasma gas and the results of nitriding effects were evaluated in terms of surface morphology, microstructure, nano-hardness, wear resistance, and corrosion resistance [110].

4.3.1 Design of experiments and materials

The experimental set-ups used for LPEB irradiations were the same with previous works. For this study, the plasma source was changed from Ar to nitrogen (N_2) for LPEB nitriding process, which represents the LPEB irradiation using N_2 plasma gas. Furthermore, a negative DC bias cathodic apparatus was attached to the general experimental set-up to attract the N_2 plasma from environment to the substrates. The Ti-6Al-7Nb sample was connected to a copper electrode to apply a negative DC bias as summarized in Figure 36. The detailed parameters of LPEB irradiation are summarized in Table 8.

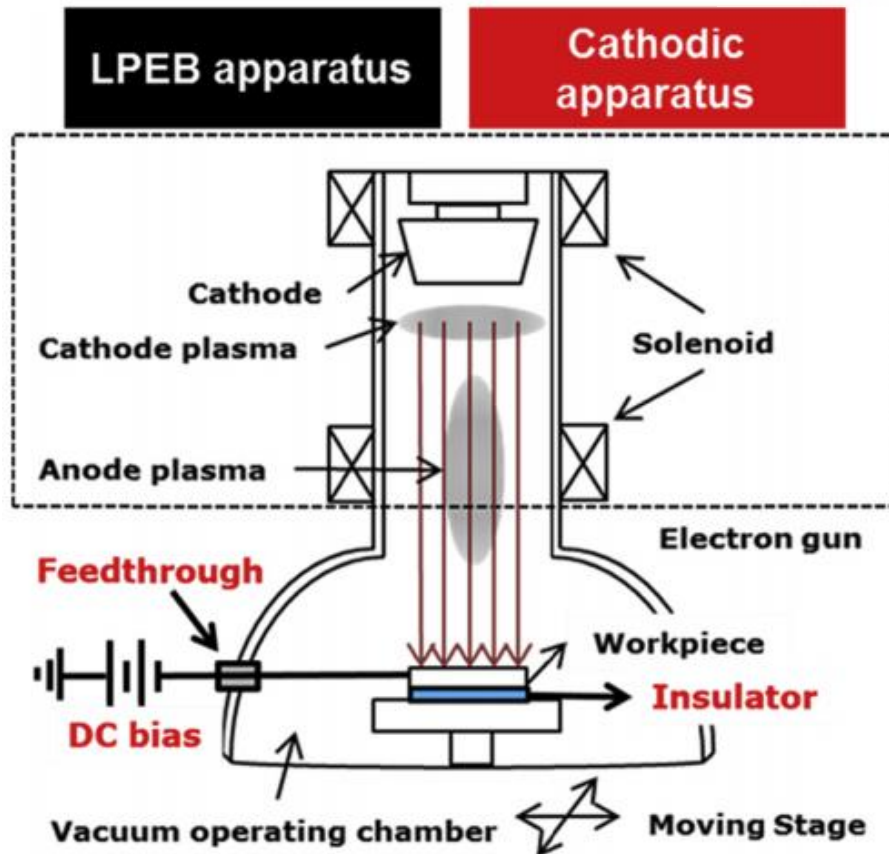


Figure 36. Schematic diagram of the experimental set-up for the LPEB nitriding

Table 8. Parameters of the LPEB nitriding process

Parameter	Value
Acceleration voltage (V_a)	30 kV
Energy density	10 J/cm ²
Plasma gas pressure (Ar and N ₂)	0.05 Pa
Pulse duration	2 μs
Negative DC bias	0 – 1000 V
Number of pulses	0 – 200 pulses

4.3.2 Microstructure and chemical components

Figure 37 shows the SEM images and corresponding roughness at the surface following LPEB irradiation using Ar and N₂ plasma gas. The surface roughness (R_a) was reduced significantly following LPEB irradiation with both Ar and N₂ plasma gas. R_a was reduced from ~540 nm to ~90 nm on the LPEB irradiated surface both with Ar and N₂ plasma gas when compared to the bare surface. This may be attributable to surface dissolution by LPEB, which could melt the polishing mark and generate a phase transformation on the surface. However, when applying a negative DC bias for the nitriding process, R_a on the surface was slightly larger than that on the surface with no DC bias because numerous crater-like defects were generated following LPEB irradiation as specified by white-interference micrographs in Figure 38. Especially, with a negative DC bias larger than 100 V, the defects were

formed frequently and their sizes were larger. The partial evaporation of non-metallic inclusions, such as manganese sulfide (MnS) and metal carbide was the major reason for crater generation during the LPEB irradiation process on mold steels. However, in the case of Ti-6Al-7Nb, there are almost no non-metallic inclusions, suggesting that the mechanism of crater generation differs from that of the iron-base alloys. Thus, SEM images and corresponding EDS analyses were performed to understand the crater generation mechanism during the LPEB nitriding process (Figure 39). The EDS results indicated that small particles consisted of iron at the center of the craters. Thus, it can be concluded that the increasing density of craters with increasing negative DC bias resulted mainly from sputtering effects on the surface by generating a glow discharge of plasma ions remaining in the vacuum chamber. Thus, it is preferred that the DC bias level should not exceed 100 V, because this is relatively low compared with the threshold voltage.

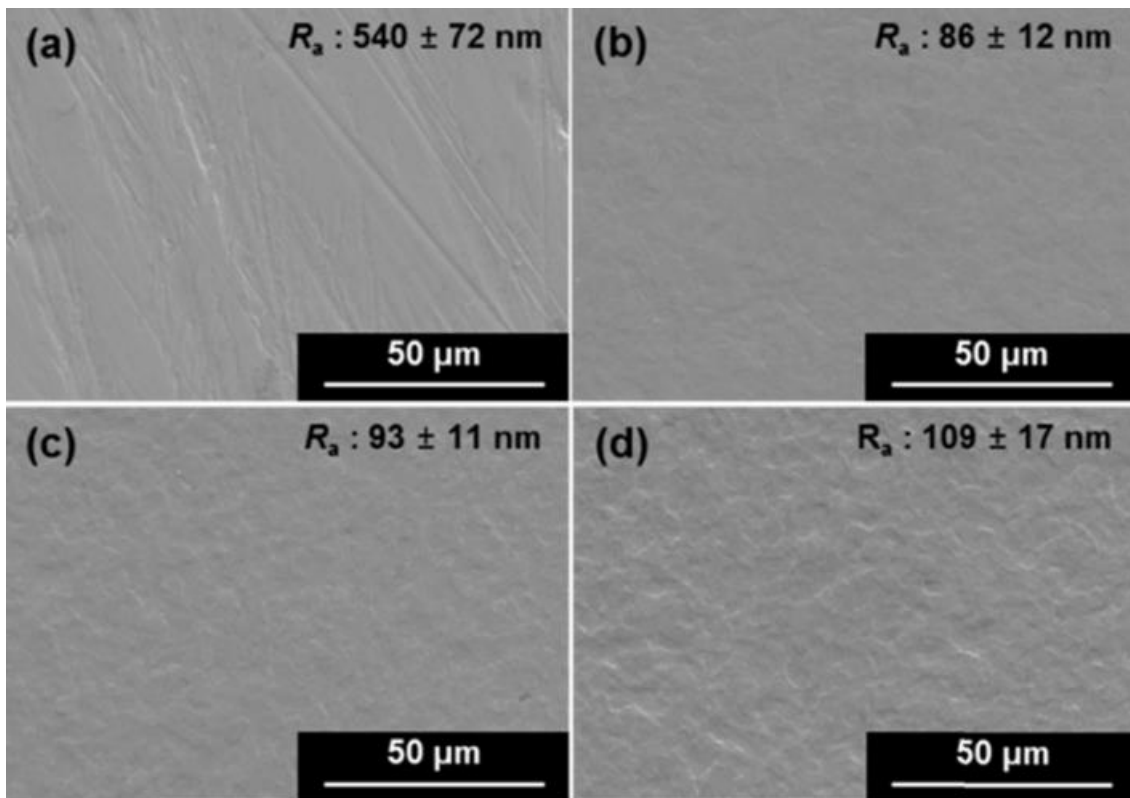
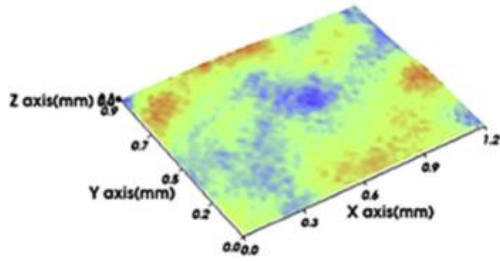


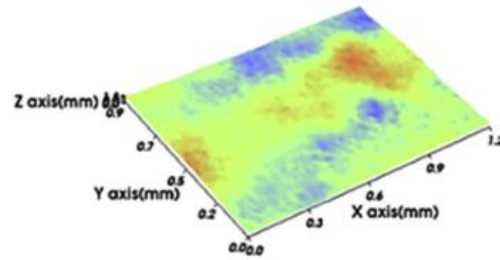
Figure 37. SEM images on Ti-6Al-7Nb surfaces (a) before and after LPEB irradiations with (b) 0 V-biased in Ar gas, (c) 0 V-biased in N₂ gas, and (d) -100 V-biased in N₂ gas

(a) 0V-biased with N₂ gas



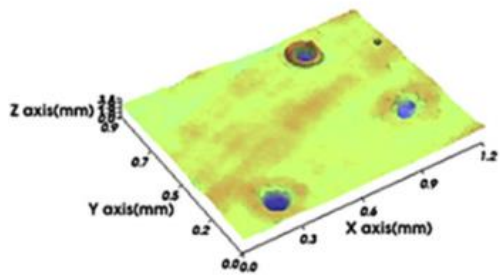
$R_a : 93 \pm 11 \text{ nm}$

(b) -100V biased with N₂ gas



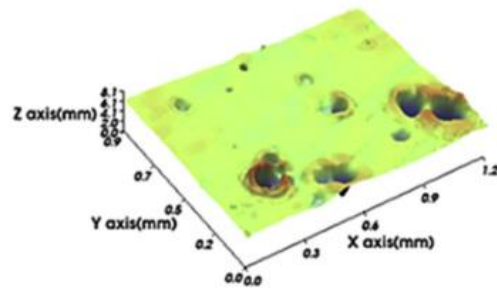
$R_a : 109 \pm 17 \text{ nm}$

(c) -500V-biased with N₂ gas



$R_a : 250 \pm 86 \text{ nm}$

(d) -1000V-biased with N₂ gas



$R_a : 483 \pm 104 \text{ nm}$

Figure 38. White-interference micrographs on the surface of Ti-6Al-7Nb after the LPEB irradiations

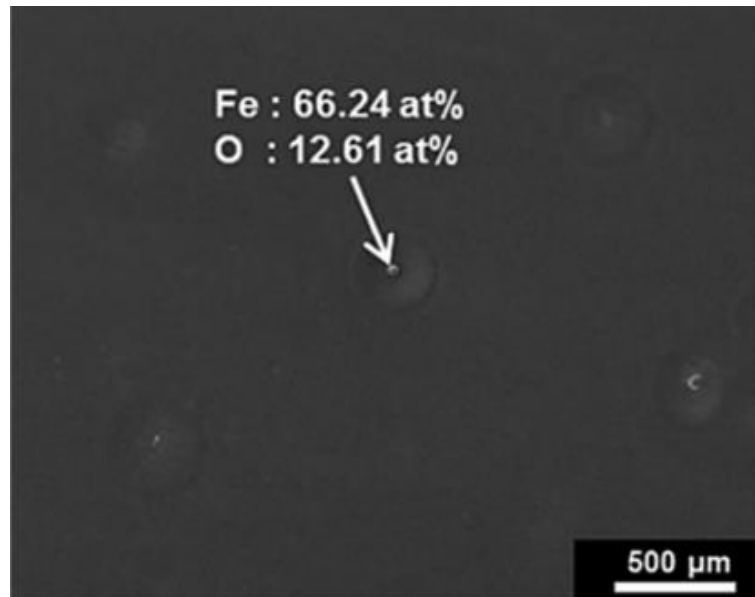


Figure 39. A SEM image and EDS result near the crater-generated region corresponding to FIGURE

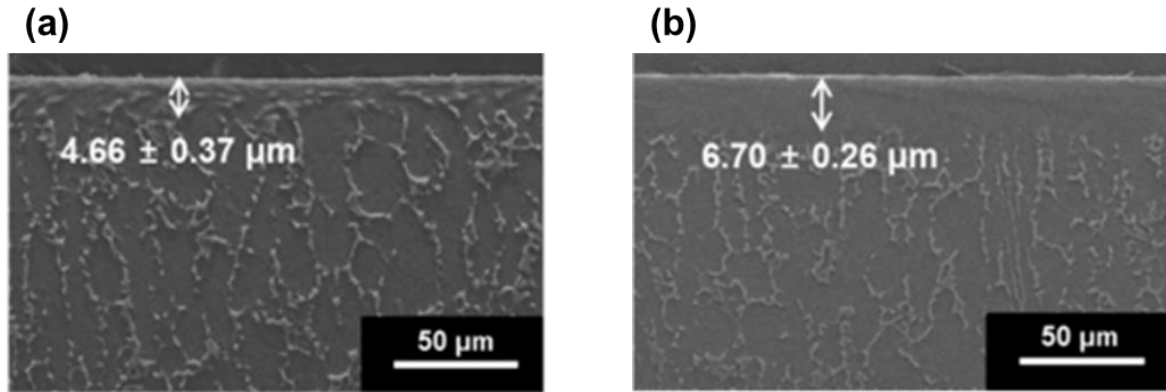


Figure 40. Cross-sectional SEM images of LPEB-irradiated Ti-6Al-7Nb with (a) Ar plasma gas and (b) N₂ plasma gas

Figure 40 shows the cross-sectional SEM images of Ti-6Al-7Nb alloys following LPEB irradiation with Ar and N₂ plasma gas. The depth of the re-solidified layer could slightly increase with more pulses; however, it did not vary markedly above 10 pulses. The depth of the re-solidified layer induced by LPEB irradiation was deeper with Ar than using N₂ plasma gas. This could be a result of a change in beam energy density transferred to the surface of the substrates. The beam energy induced from the electron gun is partially absorbed by plasma gas ionizing atoms. The ionization energy of each plasma source used in LPEB irradiation is expressed as:



As shown in Eq. (29) and (30), Ar plasma is induced simply, only consuming the ionized enthalpy of 1520.6 kJ/mol in a single ionization step. In contrast, N₂ plasma is generated in multiple steps to make the same number of electrons by consuming a total enthalpy of 1874.5 kJ/mol to break the powerful triple bond of the nitrogen molecule (472.5 kJ/mol) and to ionize it (1402 kJ/mol). Thus, the energy absorbed on the surface of substrates is relatively small with N₂ plasma gas, leading to a thinner depth of the re-solidified layer than the one obtained under Ar plasma.

In addition to the depth of molten layer and phase transformation, in the case of nitriding processes, the fraction of nitrogen available for reaction plays a major role in determining the formation of TiN. The EDS results indicating the variations in atomic concentrations following LPEB irradiation are summarized in Table 9 and 10, as a function of the negative DC bias and number of pulses, respectively. The corresponding variations in nitrogen concentration are shown in Figure 41. When compared with bare Ti-6Al-7Nb, the atomic concentration of nitrogen was increased slightly after LPEB irradiation

with Ar plasma gas (Figure 41(a)). This could be a result of the flushing gas, which was used to clean up the vacuum chamber between pulses. Because nitrogen was used as the flushing gas during LPEB irradiation, some of the gas remained in the chamber, forming a small fraction of TiN at the re-solidified layer. By changing the plasma source for LPEB from Ar to N₂, it was possible to achieve a much higher fraction of nitrogen in the re-solidified layer. LPEB nitriding without a negative DC bias increased the nitrogen fraction, to 17.08 at. %, at the top surface. Moreover, the nitrogen fraction was increased further by applying a negative DC bias to the substrate. It was increased to over 18 at. % with a negative DC bias ranging from 0 to 1000 V. The optimized number of pulses in terms of nitrogen fraction was well matched to that of the re-solidified depth. The atomic concentration at the re-solidified layer was almost unaffected by increasing the number of pulses above 10 (Figure 41(b)). The effect of negative DC bias was clear; the nitrogen fraction was increased with 100 V of bias compared with 0 V. However, no significant change in nitrogen fraction was observed with various DC biases above 100 V; all substrates were similar, ~18.5 at. %. Thair et al. [111] showed that TiN was not formed if the nitrogen concentration was lower than ~6 at. %; otherwise, TiN was formed uniformly at the surface if nitrogen concentration was ~20 at. %. Thus, it can be concluded that an effective nitriding process could be performed using LPEB irradiation with N₂ plasma gas and a negative DC bias. Also, 100 V of DC bias was the optimal condition because use of a larger bias did not modify the nitrogen concentration significantly and induced the small crater-like defects shown in Figure 38.

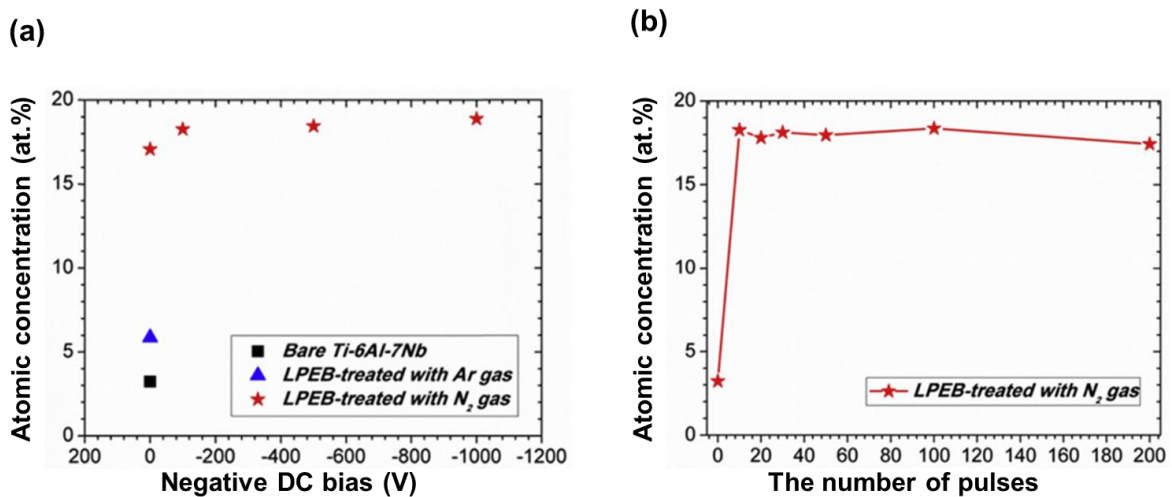


Figure 41. Atomic concentration of nitrogen after the LPEB irradiation in terms of the (a) negative DC bias and (b) number of pulses

Moreover, the nitrided layer induced by the LPEB nitriding process showed clearly different microstructures when compared to that induced by conventional nitriding processes. Conventional nitriding processes such as plasma nitriding, gas nitriding, and solid nitriding induce two main layers; 1) compound layer (white layer); and 2) diffusion layer as described in Figure 42 (a). Generally, the

compound layer with superior surface hardness and chemical stability determines the tribological and anti-corrosion characteristics of the nitrided layer. The diffusion layer, generated by the diffusion of nitrogen ions inside the bulk at high-temperature is considered to be beneficial to prevent fatigue fracture. However, when the thickness of the white layer is about 10 μm or more, problems such as cracking and voids could affect its quality resulting in the delamination of the white layer. Unlike the conventional nitriding processes, the LPEB nitriding process proceeds at relatively low temperature with a rapid thermal gradient. As a result, the diffusion layer is hardly formed while a stable white layer can be achieved.

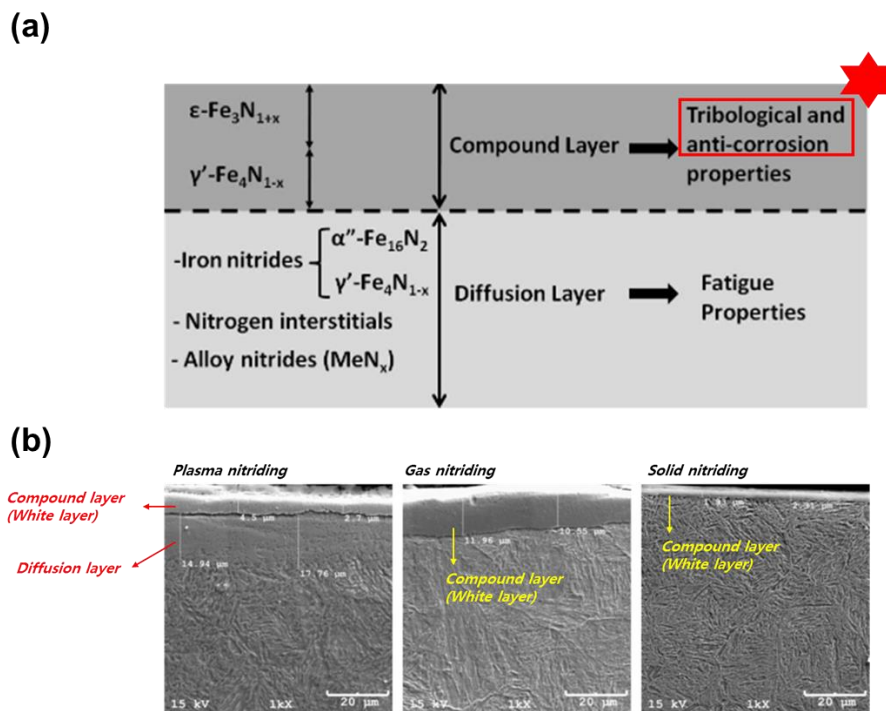


Figure 42. (a) Schematic diagram of nitrided layers and (b) cross-sectional SEM images following plasma, gas, and solid nitriding processes

Figure 42 shows the cross-sectional SEM images of mold steels after plasma nitriding. It is evident that the thickness of the white layer is varied from 5 to 15 μm , and the diffusion layer is irregular. Furthermore, it is a well-known problem during plasma nitriding that the surface roughness can be adversely affected by the physical exchange of metal ions by nitrogen ions. In case of long time nitriding, in order to bring the nitrogen content closer to the theoretical maximum of 20%, formation of a very thick white layer (about 10 μm or more) occurs and such a thick nitrided layer is susceptible for cracking and generation of voids. To solve these problems, post-processing is essential in most of cases in which the thick white layer is removed by mechanical polishing. Consequently, the production efficiency is significantly lowered.

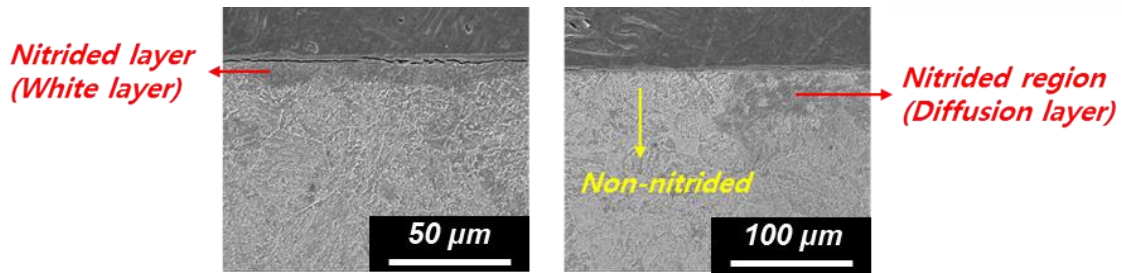


Figure 43. Cross-sectional SEM images after the plasma nitriding process on mold steels at two randomly selected regions

These inferences make it clear that the LPEB nitriding process is highly suitable for forming a white layer with a thickness of 10 μm or less (Figure 40), and under optimized processing condition, the nitrogen content of the layer reaches about 18 to 19 %, which is similar to the theoretical maximum (Figure 41). Most importantly, the LPEB nitriding process favours the formation of a white layer with uniform thickness regardless of area and shape of products. Finally, there is a great advantage of the process that the surface roughness of the treated component can be decreased when compared to the conventional nitriding process (Figure 37).

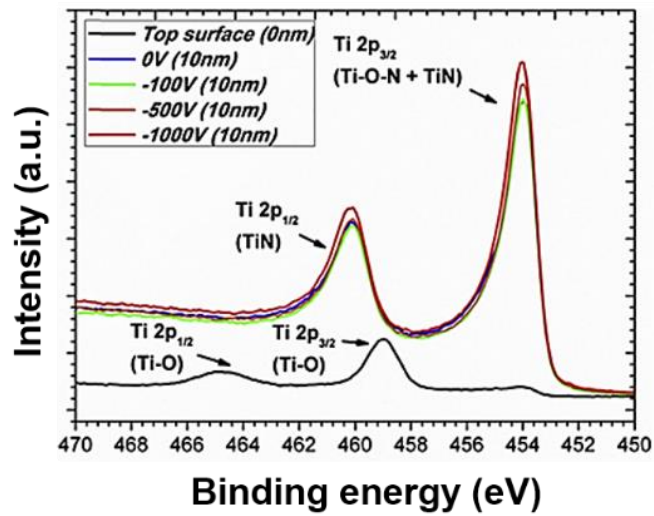
Table 9. Energy dispersive X-ray spectroscopy of Ti-6Al-7Nb before and after the LPEB irradiation and nitriding process in term of the negative DC bias

Types of plasma gas	Negative DC bias (V)	Atomic concentration (at.%)			
		C	N	O	Ti
Untreated	0	9.86	3.23	13.92	55.77
Ar	0	5.42	5.87	8.69	63.48
N ₂	0	3.81	17.08	3.84	64.75
N ₂	-100	3.51	18.27	3.26	63.68
N ₂	-500	5.35	18.45	4.17	60.70
N ₂	-1000	5.00	18.88	3.09	62.90

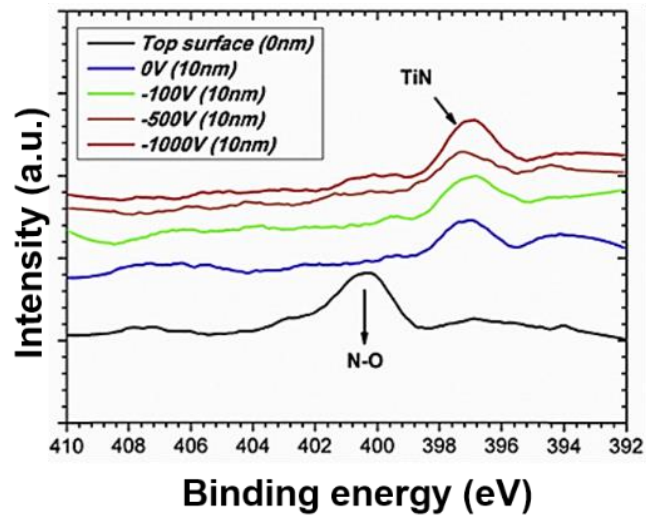
Table 10. Energy dispersive X-ray spectroscopy of Ti-6Al-7Nb after the LPEB nitriding process in term of the number of pulses

Types of plasma gas	Pulses	Atomic concentration (at.%)			
		C	N	O	Ti
N ₂	10	3.51	18.27	3.26	63.68
N ₂	20	5.31	17.80	3.84	61.53
N ₂	30	5.95	18.12	3.85	61.84
N ₂	50	4.87	17.96	3.21	63.46
N ₂	100	5.63	18.36	3.27	64.03
N ₂	200	7.07	17.43	3.93	63.02

(a) Ti-2p



(b) N-1s



(c) O-1s

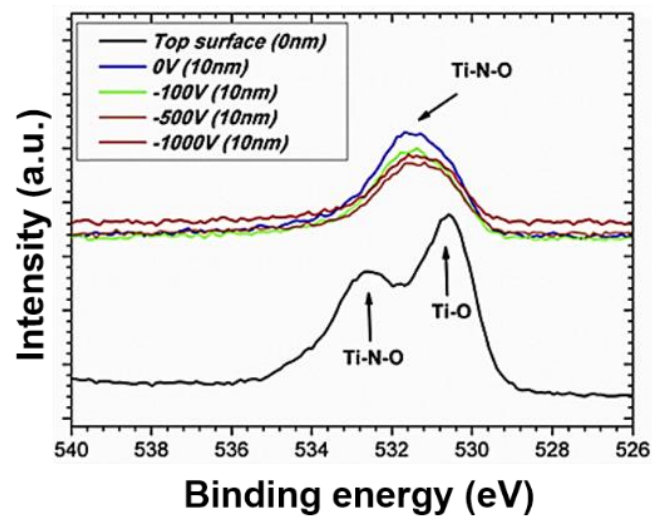


Figure 44. XPS spectra of Ti-6Al-7Nb after the LPEB nitriding with the negative DC bias

In addition to EDS analyses, XPS results specified the formation of TiN in the re-solidified layer after LPEB nitriding. The XPS results are presented in Figure 44. The spectral data were obtained at the top surface and 10 nm-deep regions of Ti-6Al-7Nb samples subjected to LPEB nitriding at 0, 100, 500, and 1000 V bias in N₂ gas atmosphere. It is clear that TiN and TiO_xN_y were formed on Ti-6Al-7Nb after LPEB nitriding. In Figure 44(a), the binding energy of the Ti-2p_{3/2} peak or shoulder was shifted from the 458-460 eV range to 453-456 eV. Also, the Ti-2p_{1/2} peak was moved from the 464-465 eV range to 459-461 eV, with a higher overall intensity of the spectrum. It has been documented that TiN and TiO_xN_y correspond to the Ti-2p_{3/2} peak appeared at the ~454.5 and the Ti-2p_{1/2} peak indicating TiN was measured at ~460.85 eV. Thus, the shift in the Ti-2p spectrum suggested that TiN was formed inside the re-solidified layer while a compound layer, composed mainly of TiO_x, was formed at the top surface. Additionally, the spectrum of N-1s in Figure 44(b) showed the extent of TiO_xN_y at the top surface and TiN at 10 nm below the top surface. These results were well agreed also with the spectrum of Ti-2p and O-1s, as shown in Figure 44(a) and (c). It can be concluded that LPEB nitriding could facilitate nitrogen implantation in the re-solidified layers and the formation of TiO_xN_y layers on the nitrided layers.

4.3.3 Mechanical properties

TiN is known to have much higher hardness than conventional titanium alloys, such as Ti-6Al-4V and Ti-6Al-7Nb. Moreover, surface hardening effect of LPEB irradiations has been firmly established in previous chapters. Thus, a comparison of the nano-hardness profiles of the bare and LPEB-treated Ti-6Al-7Nb alloy with Ar and N₂ plasma gas are appropriate to specify the surface hardening and extent of the nitrogen diffusion into the substrates. Figure 45 shows variations in nano-hardness of the Ti-6Al-7Nb alloy after LPEB irradiation with Ar and N₂ plasma gas, as a function of depth from the surface to bulk. The nano-hardness near the top surface was increased slightly following LPEB irradiation with Ar plasma gas. At the top surface, it was modified by ~15%, and the depth of modification was observed to be ~1500 nm. Use of N₂ plasma gas during LPEB irradiation without DC bias, a further increase in nano-hardness was observed at the top surface. LPEB irradiation with N₂ plasma gas with DC bias significantly increased the nano-hardness, as shown in Figure 45. Indeed, the nano-hardness at the top surface is increased by ~75% (~5.7 GPa) when compared to the bare surface (~3.25 GPa). Although there was no major difference in nano-hardness depending on the DC bias, the most improved nano-hardness was obtained with 100 V. In addition to the increasing fraction of TiN, microstructural changes of Ti-6Al-7Nb itself following LPEB irradiation could have possibly favoured an increase in nano-hardness. The formation of TiN at the re-solidified layer generates a phase transformation during the process because the nitrogen atoms are implanted interstitially between the titanium atoms in the re-solidified layer. Thus, the lattice structures at the re-solidified layer can become distorted, resulting in surface dislocations, which are well-established hardening mechanisms of metal alloys [94]. Consequently, the nano-hardness of Ti-6Al-7Nb could be effectively modified by LPEB irradiation with

the formation of TiN at the re-solidified layer.

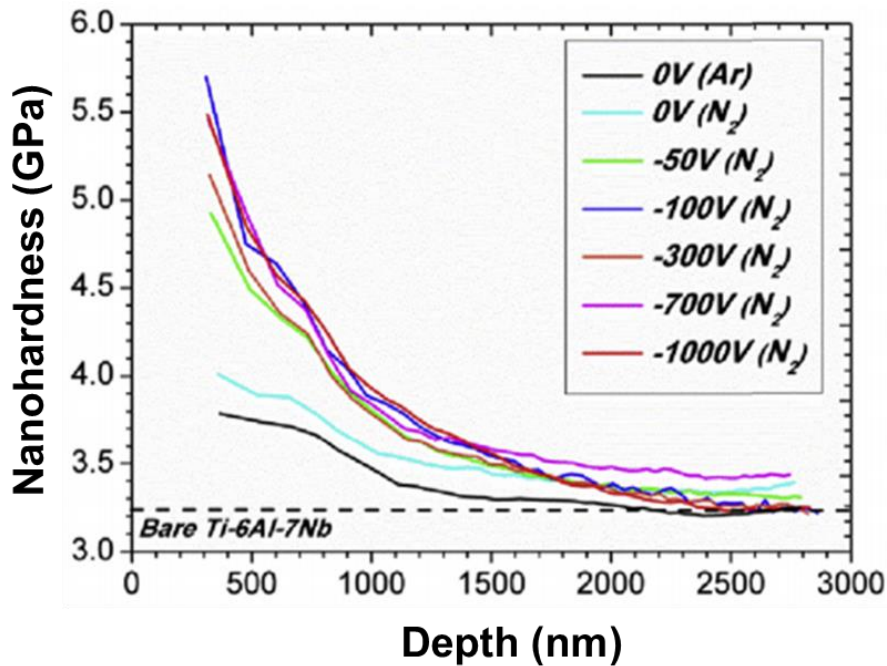


Figure 45. Variations in nano-hardness at re-solidified layer as a function of depth

4.3.4 Chemical properties

From the phase, microstructural, and nano-hardness analyses, it was clear that a 100 V DC bias was the optimal condition because the fraction of nitrogen did not vary with an increase in DC bias voltage larger than 100 V. Thus, the corrosion characteristics were evaluated with a sample irradiated using a 100 V DC bias. Figure 46 shows the representative potentiodynamic polarization curves of the untreated and LPEB-treated Ti-6Al-7Nb alloys under N_2 and Ar plasma gas atmospheres and corresponding variations of corrosion potentials and corrosion current densities in a 1 wt. % NaCl aqueous solution at room temperature. The electrochemical parameters were estimated with the same experimental conditions used for the other experiments described in Chapter 4.1 and 4.2. The corresponding electrochemical parameters including corrosion potential, corrosion current density, and Tafel slopes, are summarized in Table 11. The corrosion potential became nobler following LPEB irradiation under N_2 and Ar plasma gas atmospheres; the corrosion potential on the LPEB-treated surface with N_2 plasma gas was nobler than that on the LPEB-treated surface with Ar plasma gas. Moreover, it was possible to achieve a positive level of corrosion potential following LPEB nitriding on Ti-6Al-7Nb using a bias of 100 V. In addition to the corrosion potential, the changes in corrosion current densities also indicated an improvement in the corrosion resistance following LPEB irradiation with Ar and N_2 plasma gas (Figure 46(b)). When compared to the bare surface (194.9 nA/cm^2), much lower corrosion current density was obtained on LPEB-irradiated surface with Ar plasma gas, N_2 plasma gas, and negative DC

bias of 100 V (~ 50 nA/cm²) (Figure 46(b)). Thus, it can be summarized that the corrosion resistance of the Ti-6Al-7Nb can be increased by LPEB irradiation and the extent of corrosion protection can be further increased by LPEB nitriding.

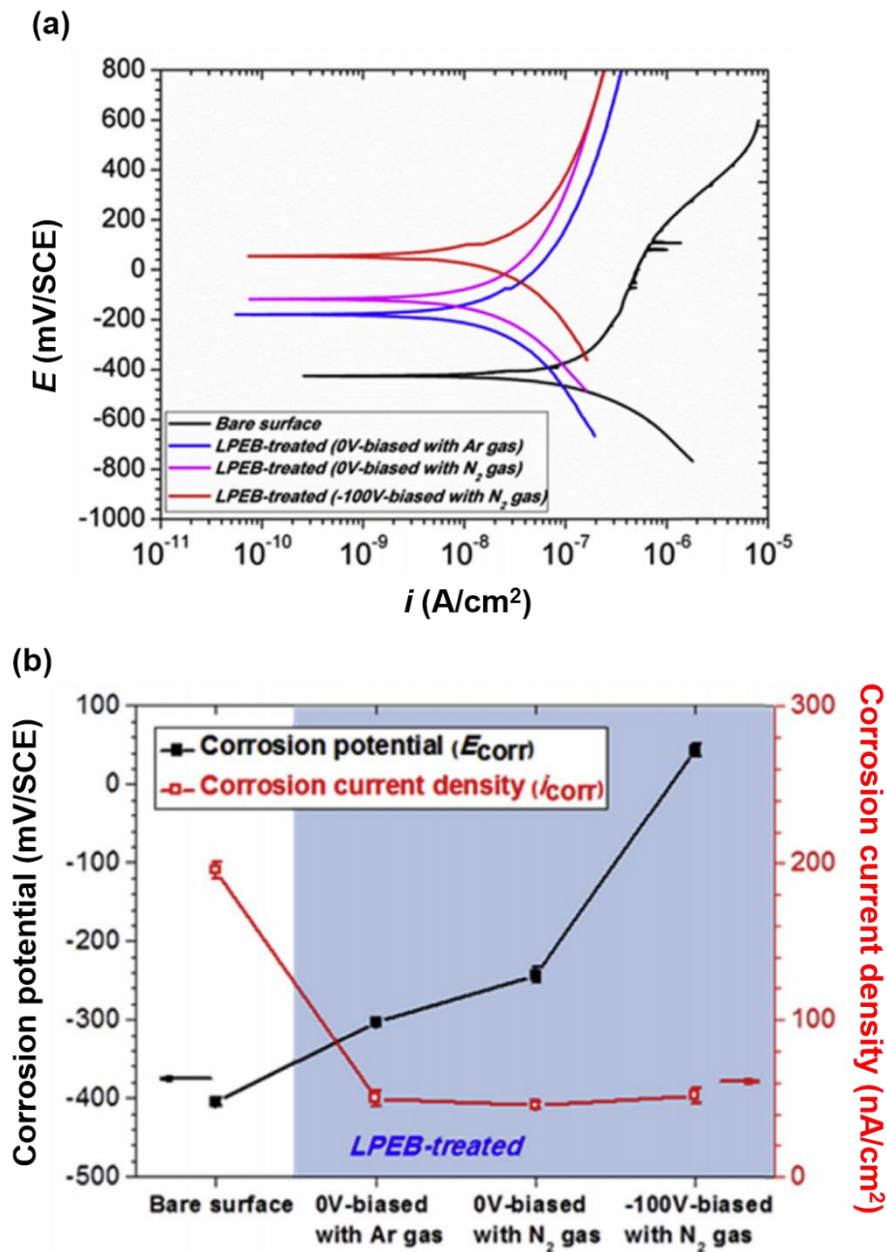


Figure 46. (a) Potentiodynamic polarization curves of LPEB-irradiated Ti-6Al-7Nb and (b) corresponding corrosion parameters

Table 11. Polarization electrochemical parameters before and after the LPEB nitriding process

Types of plasma gas	Negative DC bias	E_{corr} (mV/SCE)	i_{corr} (nA/cm ²)	β_c (mV/dec)	β_a (mV/dec)
Untreated	0 V	-404.7 ± 5.58	194.9 ± 5.04	-372 ± 10.5	971 ± 20.6
Ar	0 V	-303.5 ± 5.25	49.9 ± 4.60	-602 ± 22.9	1254 ± 22.9
N ₂	0 V	-243.0 ± 9.45	45.4 ± 2.41	-440 ± 22.0	1450 ± 40.0
N ₂	-100 V	43.2 ± 8.00	51.6 ± 5.01	-790 ± 16.0	943 ± 11.0

This further modification of corrosion resistance on the LPEB-nitrided layer comparing to the bare and LPEB-irradiated surface is strongly related to the formation of a stable and passive re-solidified layer consisted of oxides and nitrides. In order to clearly specify the effect of corrosion-resistant re-solidified layer induced by LPEB nitriding on corrosion reactions, chronoamperometry (CA) curves were analyzed potentiostatically at a certain anodic potential, +100 mV/SCE. Figure 47 shows the CA curves on Ti-6Al-7Nb samples before and after LPEB irradiations. The current densities measured from samples were increased dramatically in a few seconds immediately after the anodic potential applied. This increase of current density is mainly due to the dissolution of a passive oxide film [112]. After the momentary increase of current density, the curves soon decreased continuously till the oxide film to be fully dissolved. Finally, the current density is stabilized at a certain level, indicating continuous dissolution and formation of the passive film on the bare Ti-6Al-7Nb and re-solidified layer. As shown in Figure 47, the highest level of current density was obtained on the bare surface indicating the most reactive characteristic to corrosion, and it was not saturated until the 30th min of testing. The current densities obtained for LPEB-treated samples were significantly lower than that of the bare Ti-6Al-7Nb alloy surface. The Ti-6Al-7Nb alloy sample subjected to LPEB-treatment using Ar plasma gas indicate a current density of 40 nA/cm² at first, and it gets saturated at ~10 nA/cm² after 30 min. The LPEB-nitrided samples both with and without DC bias showed the lowest current densities; it was initially increased up to ~30 nA/cm², and then saturated at nearly zero after ~200 s, indicating negligible corrosion reactions. Thus, CA analyses confirmed that the re-solidified layer on Ti-6Al-7Nb alloy induced by LPEB nitriding has superior corrosion resistance.

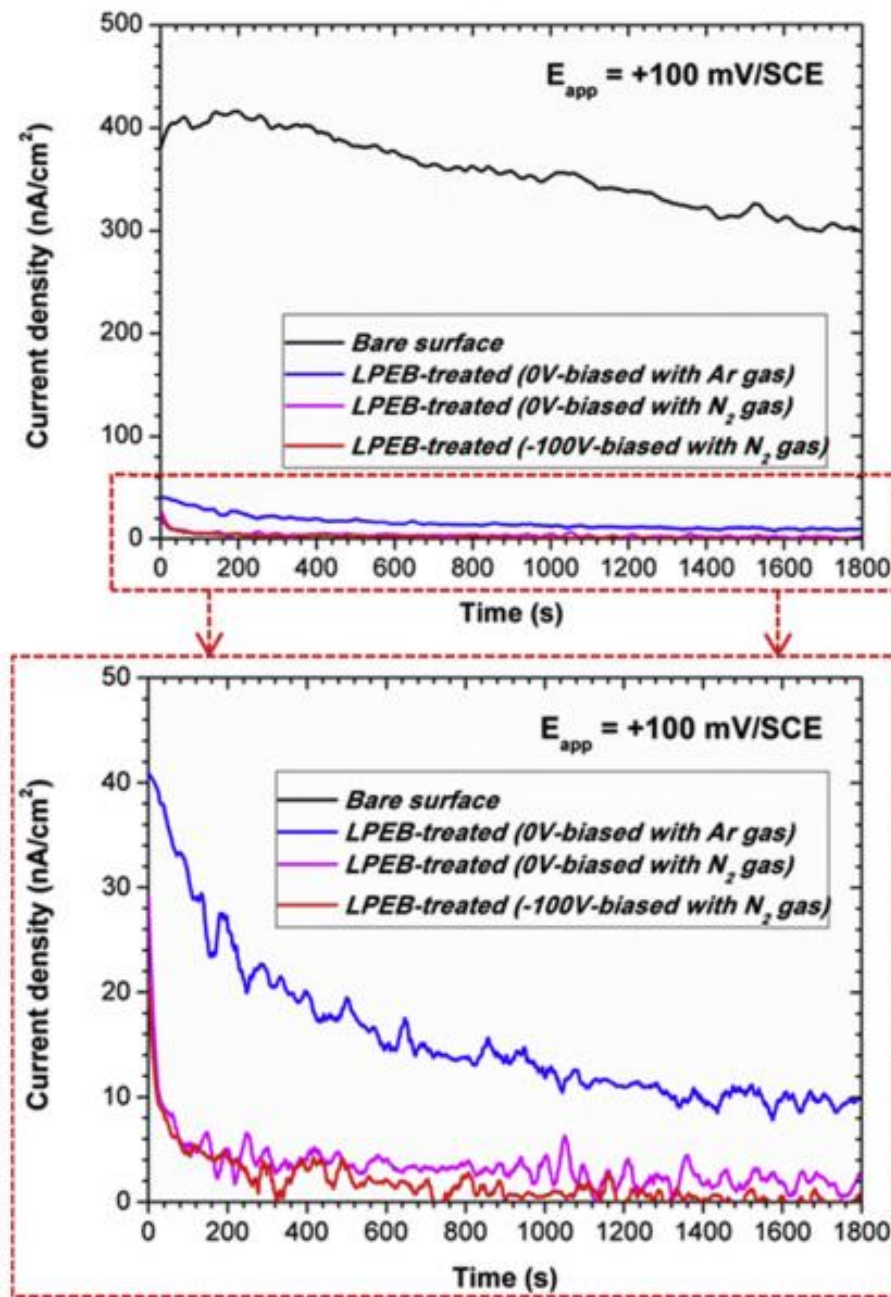


Figure 47. Chronoamperometry of Ti-6Al-7Nb before and after the LPEB irradiation

4.4 Summary

The fundamental applications of the LPEB irradiations were investigated in this chapter. The surface properties including mechanical robustness and chemical stabilities were explored and the mechanisms of surface modifications were specified following the changes in microstructure, crystalline structure, and chemical components after the LPEB irradiations. Most importantly, three major effect of the LPEB irradiation were revealed; (1) rapid surface melting and re-solidification, (2), modifications in surface properties, (3) energy transfer through electrons. Based on the predictive model of the LPEB irradiation and the optimized parameters for targeted properties on the re-solidified layer extracted by specified

mechanisms of surface modifications, the LPEB irradiation can further enlarge its application area in manufacturing processes. Based on the fundamental understandings about the LPEB irradiation effects and principles discussed in Chapter 4, Chapter 5 will cover manufacturing processes using the LPEB irradiation.

5. Applications of LPEB irradiations on manufacturing processes

5.1 LPEB manufacturing based on the melting mechanisms

As discussed in Chapter 3, the LPEB irradiation could induce rapid melting and re-solidification of materials with a molten depth of several micrometers. Although it is relatively small in terms of bulk material-based applications such as automobile and aircraft, this could be effectively adopted for precision manufacturing by melting and removing abundant parts of materials (so-called burrs), which cannot be removed by conventional finishing methods such as mechanical polishing.

5.1.1 LPEB deburring process on stainless steels

Patterned metal masks are good candidates to study the deburring process using the melting mechanism of LPEB irradiation. Manufacturing processes of electrodes in microelectronic devices such as light emitting diodes (LED) mainly focus on deposition using patterned metal masks. The deposition process of electrodes is very important in defining the shape of the pixels on the LED devices. Since the LEDs are used mainly for displays, the shape of the pixels directly affects the display definition. To define a desired shape of pixels on a display, patterned metal masks are widely used during thermal or physical deposition and spraying.

Electric discharge machining (EDM) [113], mechanical machining, and laser cutting processes are widely used to produce patterned metal masks in display industries [114-116]. The burrs generated at the edges and surfaces of the metal masks, especially during laser cutting, varies in their size depending on the type and thickness of the material and the power of the laser [117, 118].

The deburring process, which involves mechanical, chemical, and/or thermal processes to remove the burrs, has been widely studied. Previous studies have mainly focused on mechanical abrasive deburring methods [119], which effectively eliminate burrs larger than the tool used, but smaller burrs still remain after the process. Thus, the LPEB irradiation could be adopted for the deburring process of patterned metal masks combined with the abrasive deburring [120].

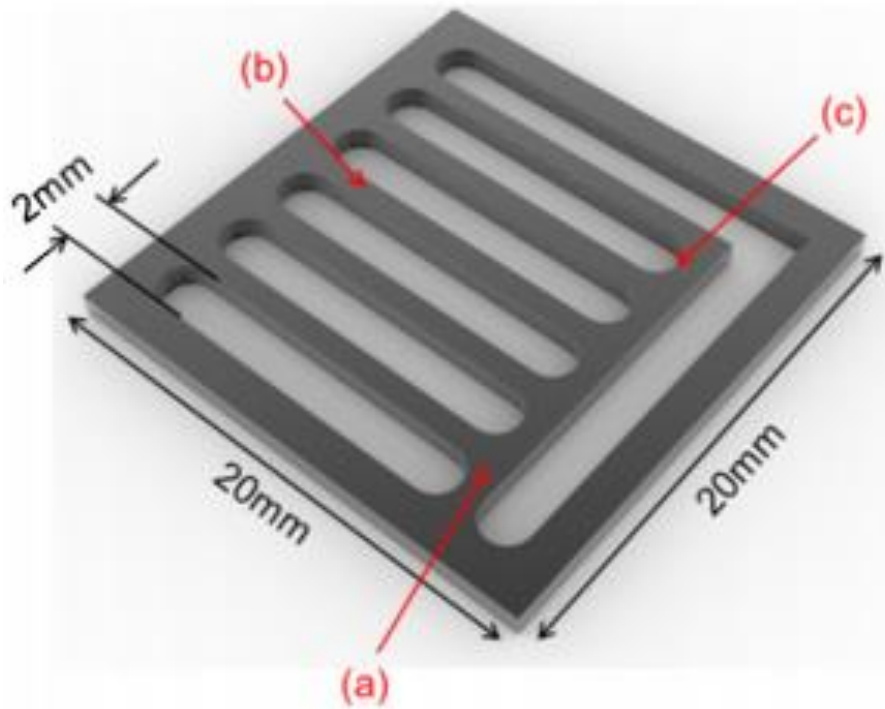


Figure 48. Illustration of a patterned metal mask

The AISI 304 stainless steel (SS304) was selected as the target material. Patterns on the metal masks were fabricated using a fiber laser, with the geometry shown in Figure 48. Abrasive deburring and LPEB irradiation were performed to remove the burrs induced on patterned metal masks during fiber laser cutting. Abrasive deburring involved a step-by-step deburring process using 320, 600, and 1200 grits of SiC coated abrasive papers in sequence. The rotating speed of the grinder used for mechanical abrasive deburring was set at 15,000 rpm with a grinding pressure of 20 N. The duration of process was kept at one minute for each step. The experimental set-up for the LPEB irradiation was illustrated in the earlier chapter (Chapter 3.4). The irradiation cycle consisted of four pulses, which formed a 2 x 2 grid, to achieve a uniform energy density on irradiated surfaces. To maximize the size of the removed burrs, the energy density of LPEB irradiations was set at 10 J/cm², with an acceleration voltage of 30 kV, as this was the maximum voltage available. The number of pulses at each irradiation point was fixed at 10 pulses. Figure 49 shows the details of each process. The standard sizes, after classifying burrs as large or small, as shown in Figure 49, were extracted from the experimental results.

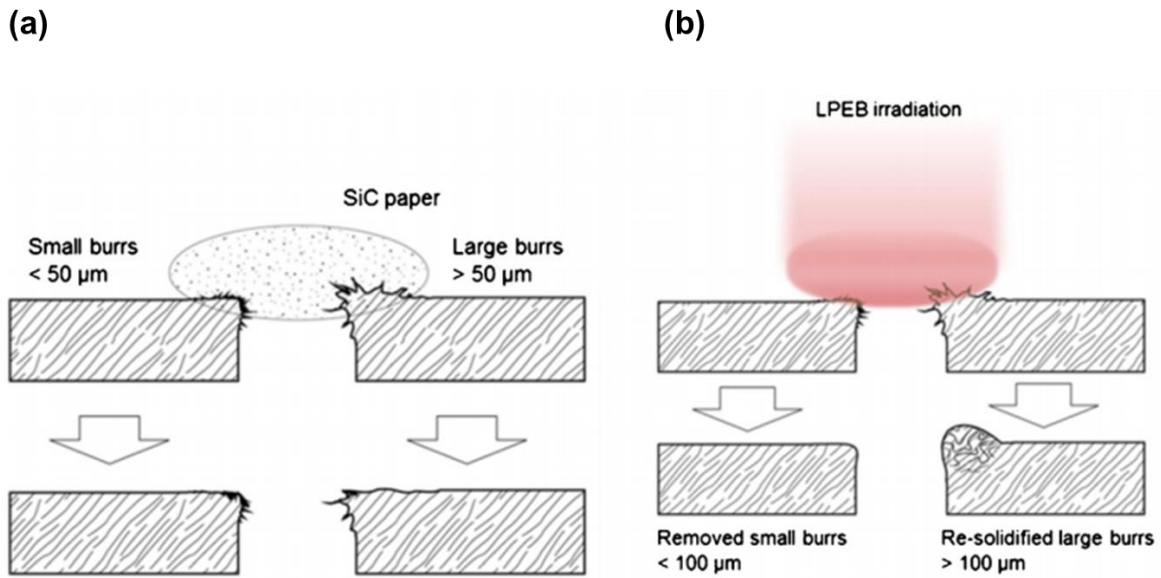


Figure 49. Schematic diagrams of (a) abrasive deburring and (b) LPEB irradiation

Burrs with various sizes were generated at the edges and on the surfaces after fiber-laser cutting, as shown in Figure 50. Points (a)–(c) in Figure 50 correspond to points (a)–(c) in Figure 48. Burr formation during fiber laser cutting was intensive at narrow straight surfaces and round edges. Burrs were generated by sparks released during melting. The average size of the generated burrs was 145.39 μm, with a minimum size of 19 μm and a maximum size of 313.02 μm. Burrs generated during fiber laser cutting on a surface can create vacant space between the samples and metal masks, requiring metal masks to be tightly secured to the surface of the microelectronic devices. If this happens, the electrodes deposited cannot form the exact desired shape and can overlap. Thus, the deburring process on the metal mask was adopted for a top surface.

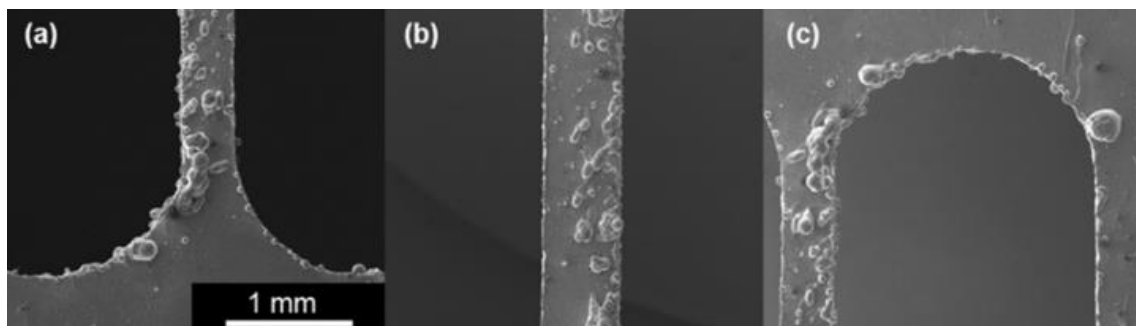


Figure 50. SEM images of the surface of patterned metal masks after fiber laser cutting

Figure 51 shows SEM images of metal masks after the abrasive deburring process. The abrasive deburring could effectively remove burrs, and was especially effective on top surfaces; but some small burrs (<50 μm) and burrs around the edges remained after abrasive deburring. The average size of the burrs that remains after abrasive deburring was 38.01 μm, a reduction by 74% when compared to the

average size of the burrs remains after fiber laser cutting (minimum: 11.23 μm ; maximum: 52.60 μm). Because abrasive deburring uses SiC particles to induce abrasive wear, burrs smaller than SiC particles could not be removed. Moreover, the burrs generated on the side faces could not be removed because the metal mask was too thin and small to apply abrasive deburring on the side faces. Although abrasive deburring is one of the most widely used deburring methods for metal masks, fracture defects are commonly observed. Thin metal sheets can be easily damaged by abrasive wear, as shown in Figure 51(b).

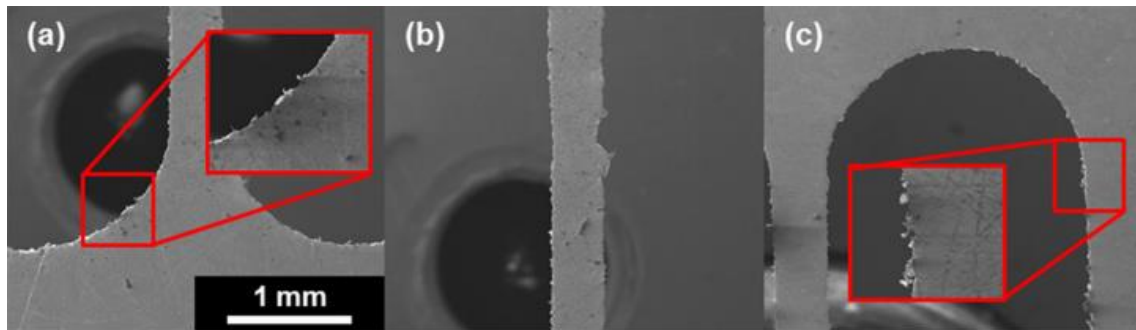


Figure 51. SEM images of the surface of patterned metal masks after abrasive deburring

The use of LPEB irradiations to deburr metal masks produced markedly different results from those of the abrasive deburring process. Figure 52 shows SEM images of the surface of patterned metal masks after LPEB irradiation. As shown in Figure 52, much larger burrs (larger than 100 μm) remained after LPEB irradiations when compared to abrasive deburring. However, burrs smaller than 100 μm at the edges were effectively removed after deburring using LPEB irradiation. This means that LPEB irradiation can melt the connecting points of small burrs and detach them from a metal mask during repeated irradiation cycles. Figure 49(b) presents the deburring mechanism using LPEB irradiation in detail. The average size of the remaining burrs was 222.92 μm , the maximum size was 283.04 μm , and the minimum size was 99.08 μm . Burrs smaller than 100 μm were effectively eliminated by LPEB irradiation. The surface texture of metal masks after LPEB irradiation was considerably different from those obtained after abrasive deburring, as shown in Figure 51 and Figure 52. The surface roughness of LPEB-treated metal masks was 332 ± 93.7 nm, which is relatively less than that of an abrasively deburred surface.

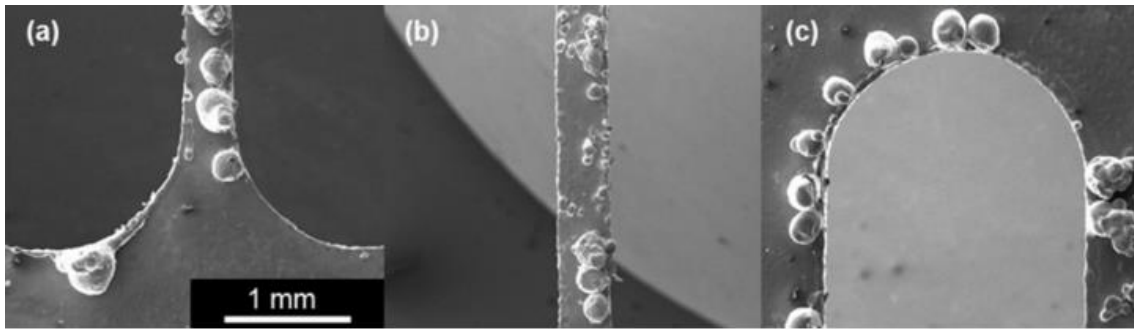


Figure 52. SEM images of the surface of patterned metal masks after the LPEB deburring

As the experimental results of LPEB irradiation revealed, only burrs smaller than 100 μm could be eliminated by LPEB irradiation. Furthermore, it is obvious that bubble-like burrs formed on the surface after LPEB irradiation, as shown in Figure 52. Some bubble-like burrs that are formed during the LPEB irradiation exhibit an increase in size. This could be attributed to the partial melting of large burrs. LPEB irradiation melts burrs, but the energy transferred during LPEB irradiation may not be enough to melt the splice of large burrs ($>100 \mu\text{m}$ in size). Meanwhile, partially melted burrs tend to aggregate by attraction due to the higher surface tension of liquid metals. Thus, prediction of LPEB irradiation was performed to verify the melting thickness induced by the LPEB.

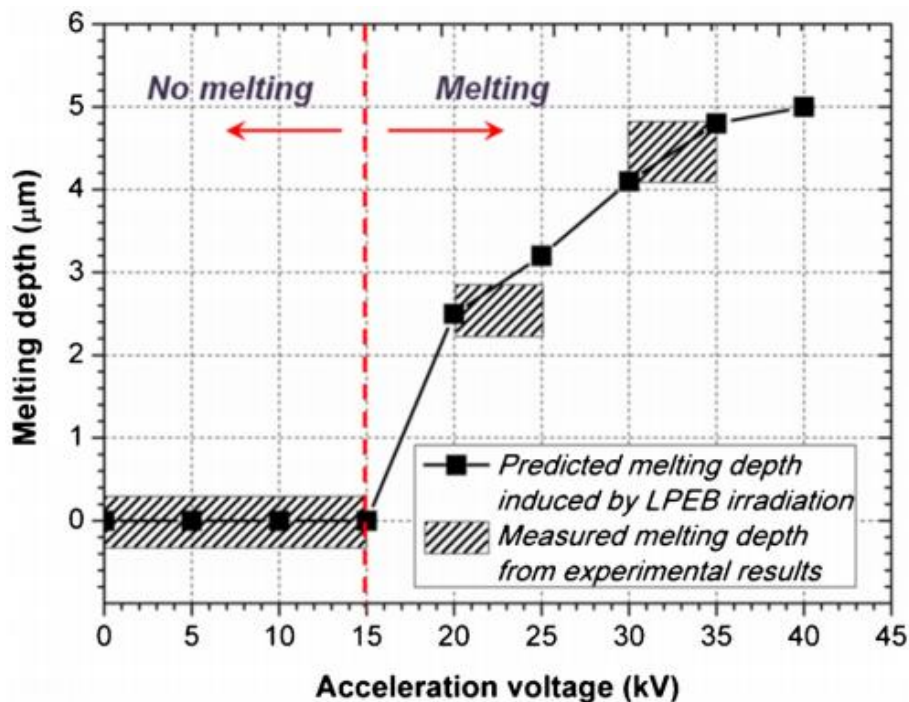


Figure 53. Variation in predicted molten depth as a function of acceleration voltage and corresponding experimental results

Figure 53 shows the variation in melting depths as a function of acceleration voltages. In the prediction of melting, the energy density of LPEB was varied with the change of acceleration voltage

from 1 J/cm^2 at 15 kV to 10 J/cm^2 at 30 kV. For low acceleration voltages, less than 15 kV, the numerical model predicted that AISI 304 stainless steel would not melt by LPEB irradiation. Metal masks would start to melt at an accelerating voltage of 20 kV, and the melting depth would continuously increase from 2.3 to $5.0 \mu\text{m}$ with an increase in acceleration voltage. From the predicted melting depth induced during treatment, it can be concluded that LPEB irradiation is effective in eliminating burrs with a splice thickness thinner than $5 \mu\text{m}$. Moreover, the experimental observations of the deburring effects of LPEB irradiation estimated that burrs smaller than $100 \mu\text{m}$ have a splice thickness thinner than $5 \mu\text{m}$, because they were almost perfectly removed by LPEB irradiation at an acceleration voltage of 30 kV. Figure 54 shows the SEM image of a generated burr after fiber laser cutting with the size of $\sim 110 \mu\text{m}$. The splice thickness of this burr is about $5.13 \mu\text{m}$. LPEB irradiation is expected to smooth the surface free of scratches that are less deep than the melting depth. Thus, it is essential to leave only scratches smaller than $5 \mu\text{m}$ before LPEB irradiation to ensure an effective removal of every scratch from the metal masks.

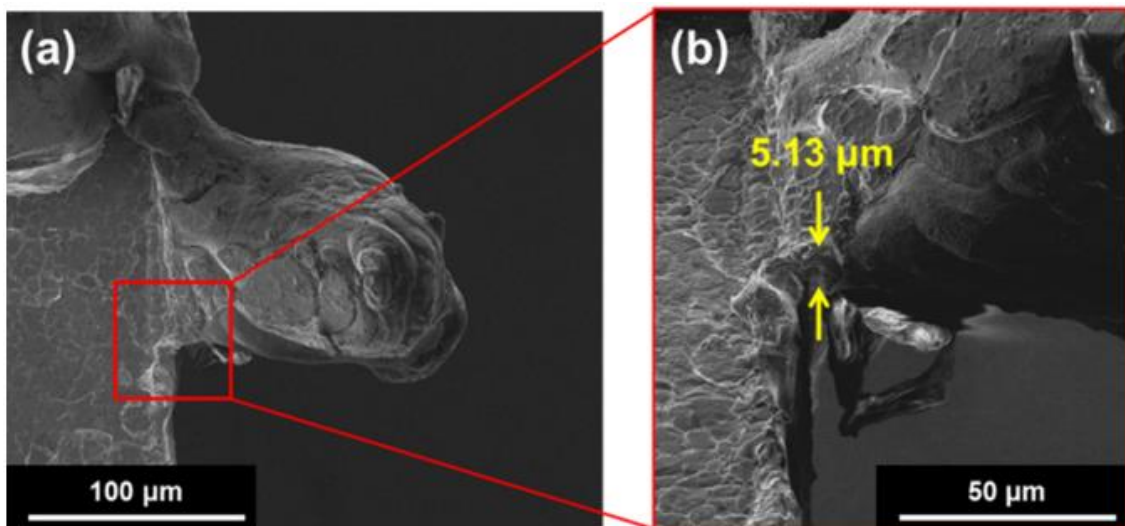


Figure 54. SEM images of a generated burr after fiber laser cutting viewed from (a) above and (b) side

The experimental results and predictions using the numerical model revealed that deburring using either abrasive deburring or LPEB irradiation is insufficient to perfectly eliminate burrs generated by fiber laser cutting. Therefore, a LPEB-assisted hybrid deburring process was developed to remove burrs regardless of their size or location. This hybrid deburring process involves a step-by-step removal by abrasive deburring and LPEB irradiation. LPEB irradiation was performed on abrasively deburred metal masks as shown in Figure 55. The frequency of the rotating unit used in LPEB-assisted hybrid deburring was 3000 rpm and the grinding pressure was 10 N, to avoid generation of any potential fracture defects on the thin metal masks.

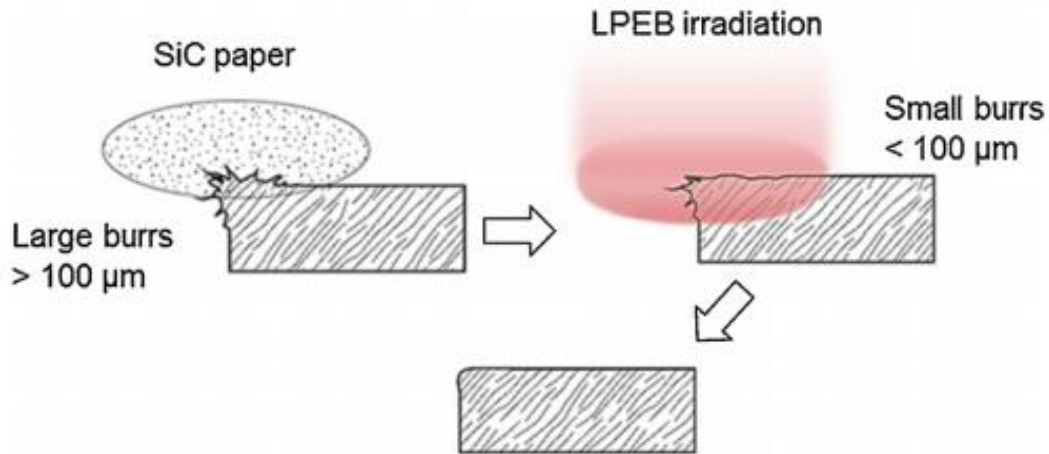


Figure 55. Schematic diagram of the LPEB-assisted hybrid deburring process

Figure 56 shows the SEM images of the surface of a metal mask after the LPEB-assisted hybrid deburring process. The hybrid deburring process could successfully eliminate the burrs regardless of their size: only burrs smaller than several micrometers are remained. Also, fracture defects were not observed on the metal masks after the process due to the relatively slow rotating speed. This result comes from combining the advantages of abrasive deburring and LPEB irradiation. During the first step, burrs larger than 100 μm and those generated on the surface were mostly removed by mechanical abrasive deburring. Subsequently, during the second step, burrs smaller than 100 μm and burrs generated at the edges and side faces of the pattern were effectively removed by LPEB irradiation splice melting. Consequently, the remaining burrs were the smallest after the hybrid deburring process when compared with other methods.

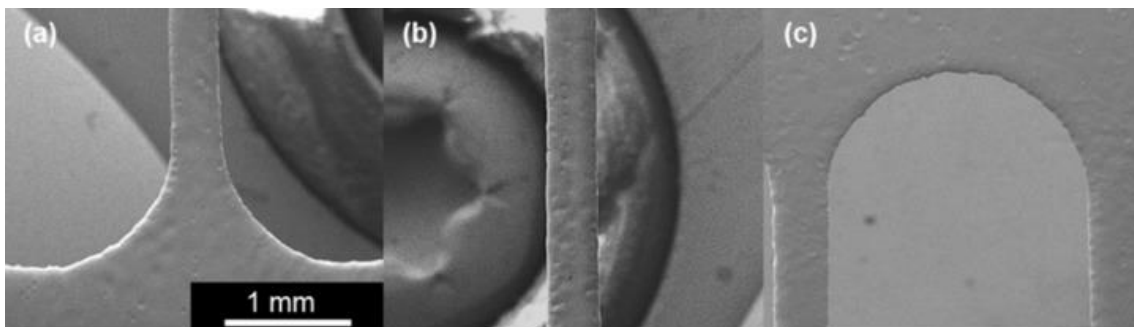


Figure 56. SEM images of the surface of patterned metal masks after the LPEB-assisted hybrid deburring

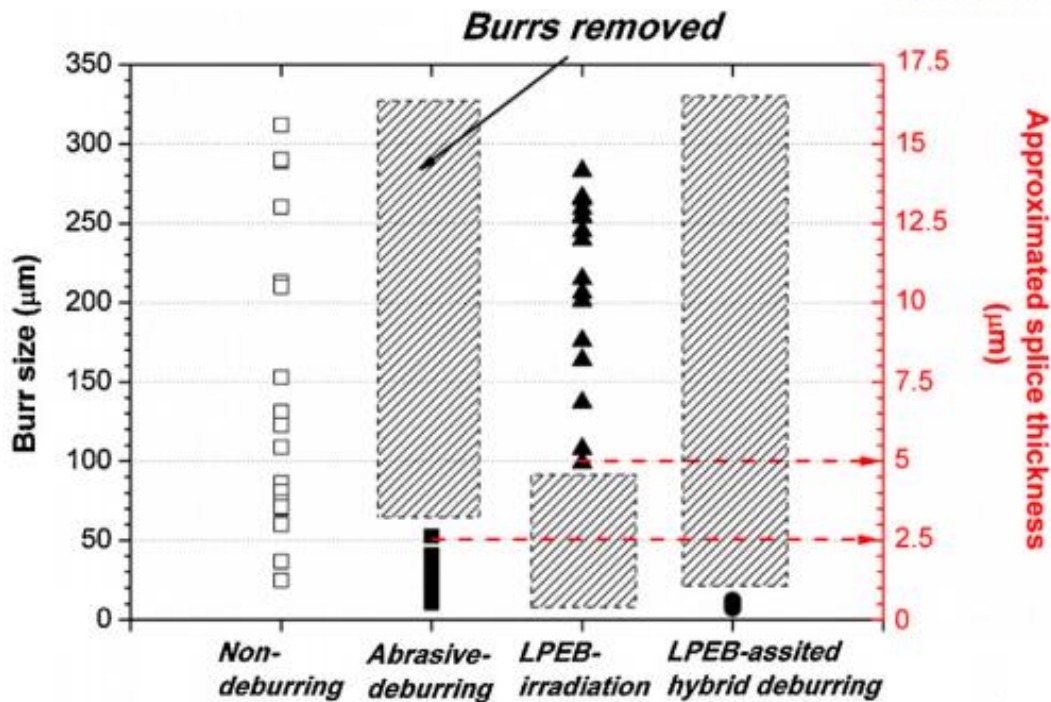


Figure 57. Scatter of the burr size generated and remaining after the fiber laser cutting and deburring processes

Figure 57 shows the distributions of the burr sizes that remains after fiber laser cutting and the deburring processes. The abrasive deburring and LPEB irradiation were completely opposite in terms of their ranges of distribution in the eliminating burr size. The distribution ranges of burr size were significantly decreased by the hybrid deburring process. This means that uniform surface texture and edges, with high levels of accuracy, can be achieved using the hybrid deburring process.

5.1.2 LPEB deburring process on CFRP composites

The deburring process based on the melting mechanisms of LPEB irradiations is not only limited to metallic alloys, but also possible to be applied for non-metallic materials. CFRP composites are a good candidate of application because they are mainly composed of two completely different materials: epoxy resin and carbon fibers. Due to the unique energy transfer mechanism of LPEB irradiation through accelerated electrons which enables effective energy transfer regardless of material types, it is believed that the LPEB deburring would be one of the most effective methods to finish CFRP composites. Although many researchers have reported that CFRPs typically have better mechanical properties than conventional metallic alloys, their industrial applications are rather limited because of the difficulty in machining them [121]. Drilling is the most widely used machining process in CFRPs. The CFRP based products are generally assembled from parts with simple structures [122]. Several problems arise when machining CFRPs, the most difficult among them being delamination and burr generation. It is not possible to completely avoid delamination and burr generation at the exit side of

the holes by controlling the machining parameters and tool geometries [123]. Thus, the optimal drilling process must be followed by adopting post processing steps to remove burrs and prevent delamination of the drilled CFRP holes. Despite the availability of various deburring processes for CFRP composites, their critical limitations prevented them from being directly applied to CFRPs. For example, solution-based processes can induce delamination if the solution penetrates between the resin and carbon fibers, and the large difference in laser absorptivity between resin materials and carbon fibers makes laser deburring difficult [124]. The most recent and promising attempt made to overcome those limitations is a dry-EDM method [125]. However, there is still no single deburring process that can guarantee the required hole quality and burr elimination with no side effects [126]. In this context, the LPEB deburring was applied on drilled holes in CFRPs.

Unidirectional CFRP composites were supplied by the Korea Institute of Carbon Convergence Technology. The CFRP composites with 3 mm thickness were fabricated by stacking 11 plies of prepreg. In the CFRP composite, the fiber volume fraction was set as 67 %. The remaining fraction of the composite was filled with epoxy resin (33%). A water-jet machining was used to cut the CFRP composites into pieces with dimensions of 20 mm x 20 mm x 3 mm. For the LPEB irradiations, the same experimental set-up described in Chapter 4 were utilized.

The CFRP composites consisted of two different materials, and they may be affected differently by the LPEB irradiation. However, it is necessary to avoid evaporation of the polymer resin at the surface of the composite and prevent damage of the carbon fibers. The carbon fibers can be damaged because the energy of the LPEB is much higher than the bonding energy of the carbon fibers and epoxy resin. Hence, an aluminum metal mask with the same dimension for that of the CFRP composite was cut using fiber laser. A hole with the same diameter as that of the drilled holes, namely 9 mm, was made on the aluminum metal mask. As shown in Figure 58, the aluminum metal mask was clamped to the drilled CFRP composite with a clip prior to LPEB irradiation. This prevented evaporation of the polymer and potential damage of the carbon fibers during irradiation, so that only the uncut fibers, or burrs, were removed.

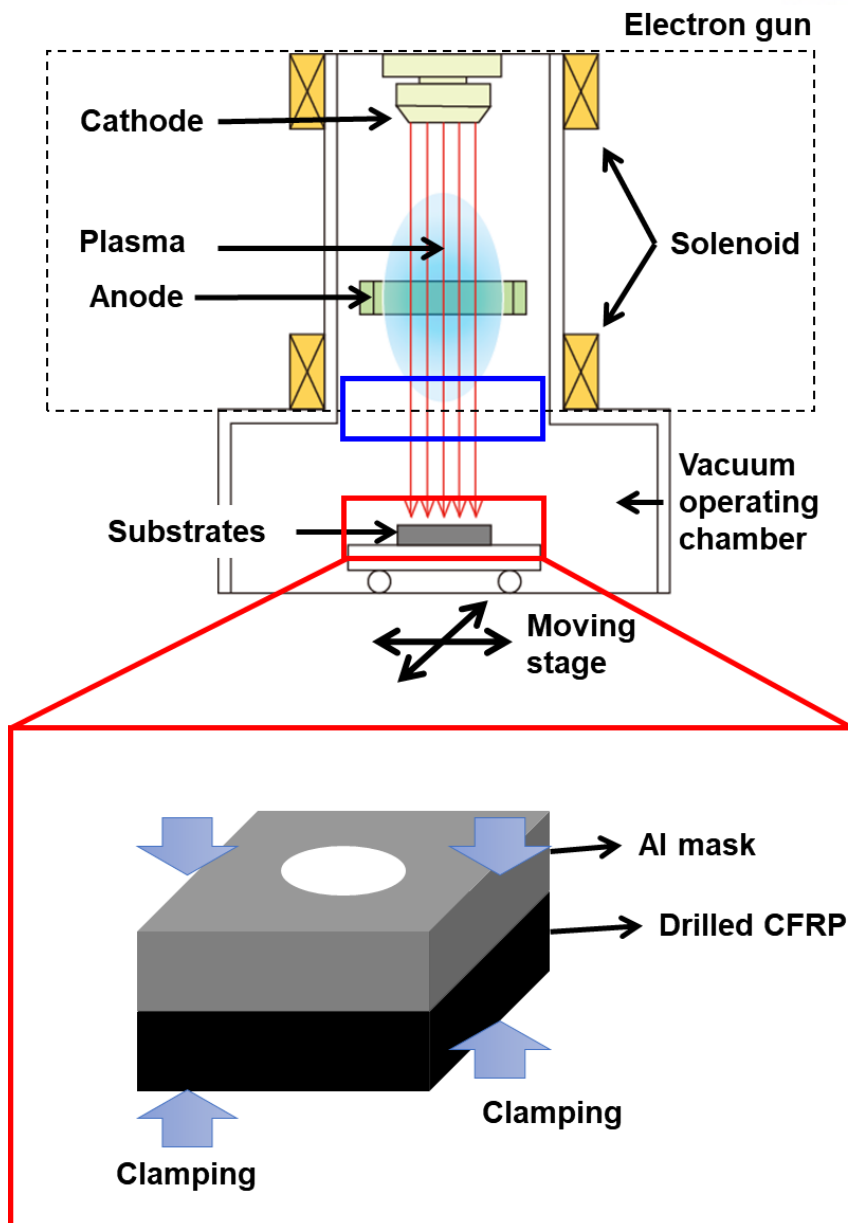


Figure 58. Schematic diagram of the experimental setups for the large pulsed electron beam irradiations

The CFRP composite has a specific orientation, so the fibers in its stacks are unidirectionally aligned. It is not possible to remove the fibers that are oriented in the direction of the drill rotation using the drill bit [127]. Although fibers at the entrances of holes can be removed by the rest of the drill bit after the drill has penetrated into the hole, the burrs at the exits of the holes will remain. This is why burr formation mainly occurs on the exit side of drilled holes. In addition, when the composite layers are separated and the bending stress exceeds the bending strength limit, uncut fibers can cause the layers to fracture, leading to delamination at the exit side of the holes. Figure 59 shows that the drilling process created a significant number of burrs. These burrs were distributed symmetrically because the CFRP used in these experiments was unidirectional. Furthermore, the burrs had a relatively high aspect ratio,

with an average length of 5.09 mm and width of 0.4 mm.

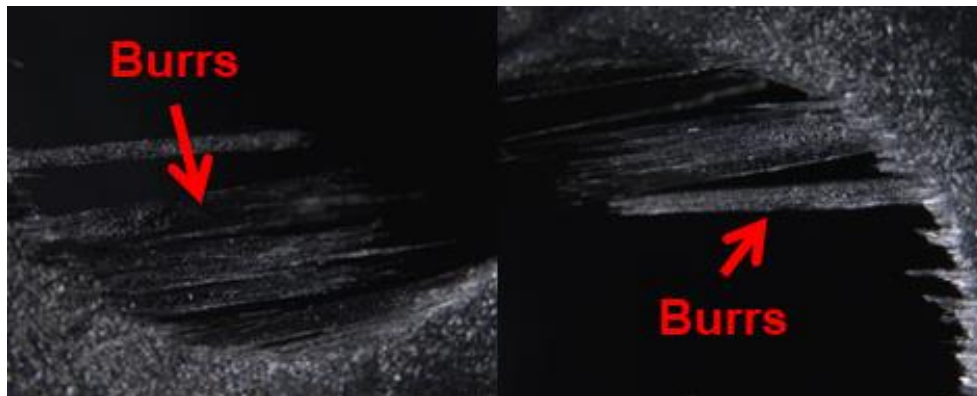


Figure 59. Optical images of the generated burrs after the drilling process on CFRP composites

It is well known that electron beams can easily break carbon-carbon bonds [128]. However, the energy density of LPEBs is much higher than that of the electron beams used in polymer crosslinking [129]. This means that repeated irradiations can break, destroy, and detach carbon-carbon bonds. As the burrs on CFRPs are mainly composed of carbon fibers, they should be removed effectively by LPEB irradiation. In addition to the parameters investigated in previous chapters including V_a and the number of pulses, V_s should also be considered that the Lorentz force induced by V_s can differ the helical pathway of accelerated electrons.

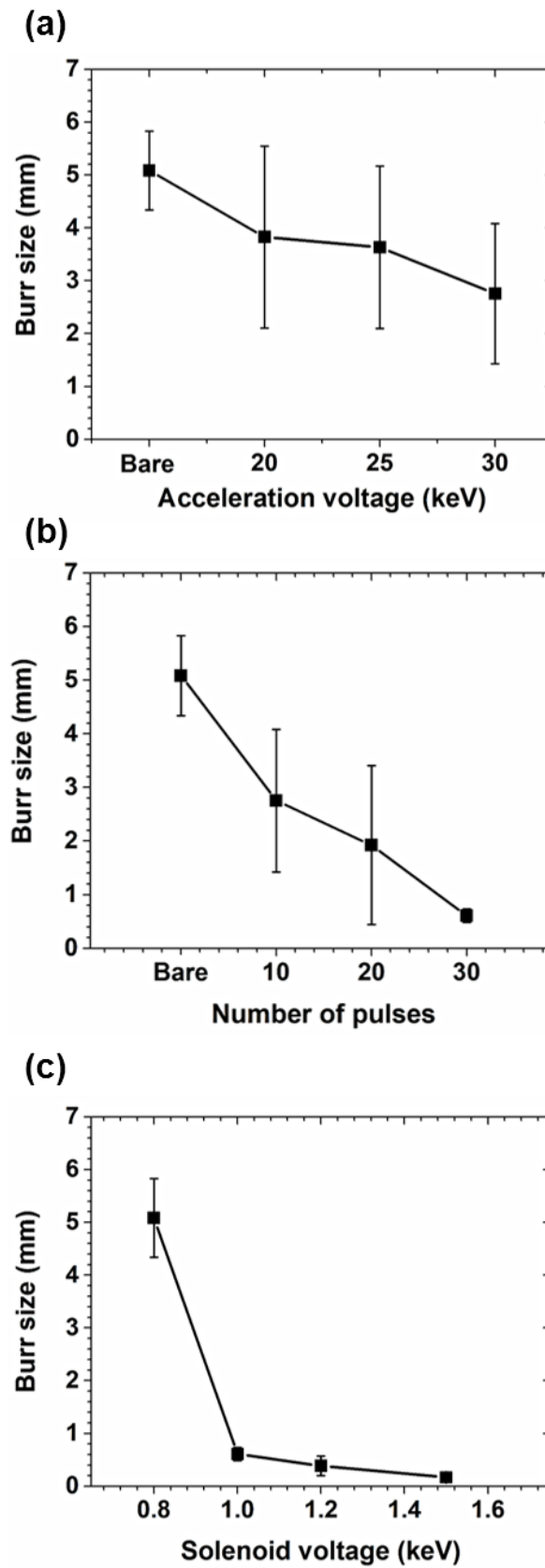


Figure 60. Variations of the burr sizes before and after the LPEB irradiations in terms of (a) acceleration voltage, (b) the number of pulses, and (c) solenoid voltage

Figure 60 shows the variations in burr size before and after LPEB irradiation as a function of acceleration voltage. The solenoid voltage was held constant at 1.0 kV and 10 irradiation pulses were used. The average size of the burrs that remains after deburring is slightly decreased with an increase in V_a . The decrease in the average size of the remaining burrs may be due to the fact that the energy density of the LPEB is increased with V_a . Figure 60(b) shows the variation in burr size according to the number of pulses, with V_a and V_s fixed at 30 kV and 1.0 kV, respectively. Increasing the number of pulses has caused a greater reduction in the average size of the remaining burrs than increasing V_a . The average burr size was reduced from 5.09 mm to 1.93 mm after 20 pulses. After 30 irradiation pulses it is reduced even further, to 0.61 mm. The largest decrease in average burr size, amounting to 88 %, has occurred after 30 irradiation pulses. Only submicro-sized burrs remained after more than 30 pulses of LPEB irradiation when the acceleration voltage was greater than 30 kV. Moreover, the quality of the drilled holes was also improved significantly, as indicated by the decrease in the error bars on Figure 60(b). Finally, Figure 60(c) shows the effect of varying V_s on the average size of the burrs remaining after LPEB irradiation. As previous investigations revealed that the performance of the deburring process improved when V_a was larger and more pulses were used, we set V_a to 30 kV and used 30 irradiation pulses while varying V_s . As we used the optimal values of the other parameters when increasing V_s , the results of these experiments were different to those of previous experiments. For each value of V_s , the remaining burrs were extremely small. Although the remaining burrs were already on the submicron level when V_s was 1.0 kV, their size reduced further as V_s increased, as shown in Figure 60(c). The smallest remaining burrs were observed when V_s was 1.5 keV. The LPEB deburring process caused a 97 % reduction in the size of the burrs, from 5.09 mm to 0.17 mm. In other words, the LPEB irradiation almost completely removed the uncut fibers generated by the drilling.

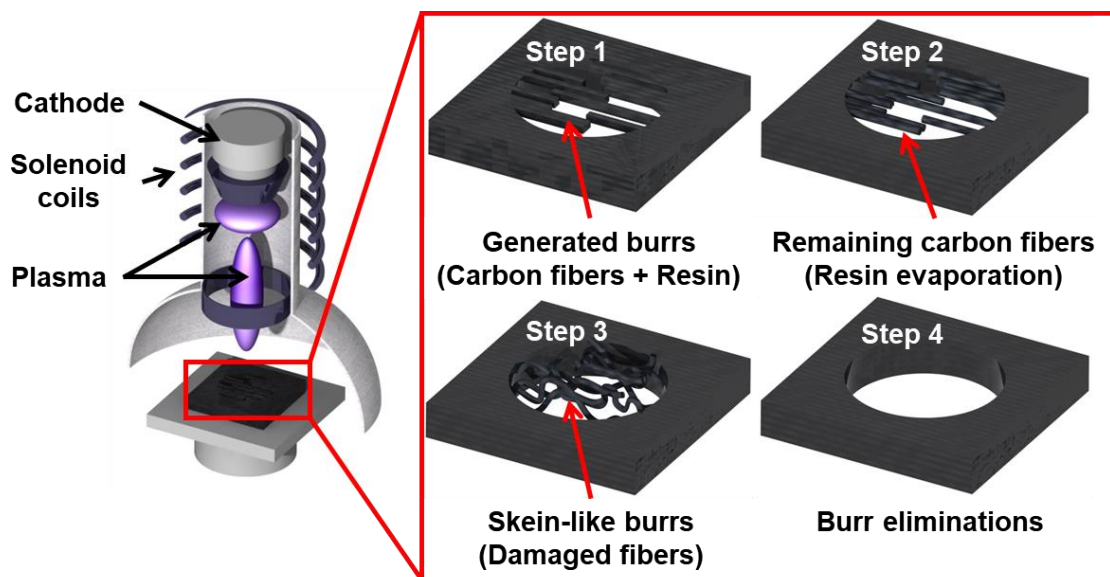


Figure 61. Schematic diagram and mechanisms of the deburring process for drilled CFRP composites using the large pulsed electron beam irradiations

Figure 60 shows an important feature of CFRP hole deburring with LPEB irradiation. The error bars indicate the distribution of the size of the remaining burrs, which varied significantly with respect to the irradiating parameters. The range of variation in burr size increased slightly when V_a is increased from 20 to 30 kV. This unexpected increase in the size variation may adversely affect the quality of the deburred holes. We observed a wide range of burr sizes, from 0.5 to 3.5 mm, when the holes were irradiated with up to 20 pulses, as shown in Figure 60 (b). However, the size range is decreased suddenly when the number of pulses is increased to 30. Figure 60(c) shows the sizes of the burrs obtained after deburring with 30 irradiation pulses as a function of V_s . The variation in burr sizes is extremely small in each case. This indicates a uniform deburring performance over all the edges of the drilled holes. This could be caused by a special interaction between the accelerated electrons and the CFRP composites. CFRP composites are composed of epoxy resin and carbon fiber. As the epoxy resin acts as an adhesive and it generally surrounds the carbon fibers. Therefore, the accelerated electrons irradiate the resin first. The LPEB irradiation induces a large thermal gradient and extremely high temperatures. Hence, if the energy density is sufficient, then the resin could become molten or evaporate within the duration of the short pulse. This means that the accelerated electrons can reach the carbon fibers and break the carbon-carbon bonds, thus detaching the uncut fibers from the substrate. These mechanisms for deburring CFRP composites using LPEB irradiation are described in detail in Figure 61.

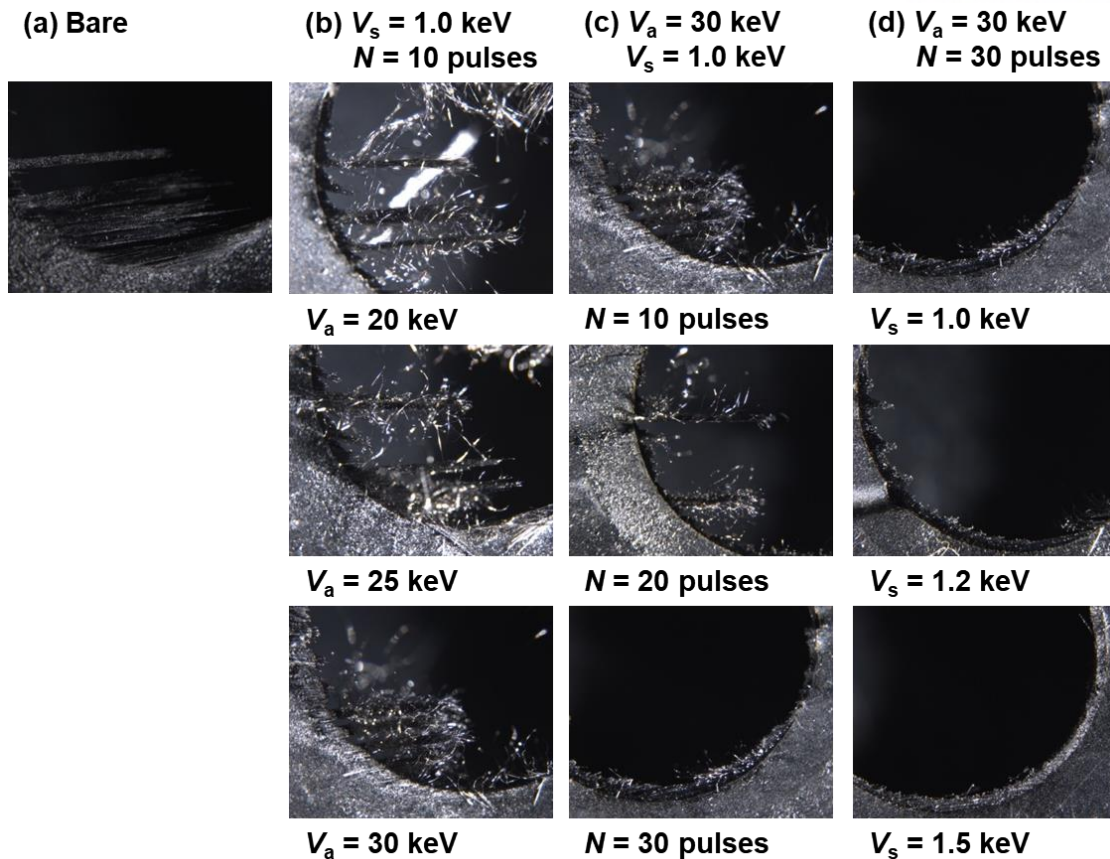


Figure 62. Optical images of the generated and remaining burrs on CFRP composites after the LPEB irradiations in terms of V_a , V_s , and the number of pulses (N)

However, for all values of V_a and V_s , more than 20 pulses were required to evaporate the surrounding resin and detach the uncut carbon fibers. The optical microscopic images clearly show the partial evaporation of the resin and the breaking of the carbon fibers. Figure 62 shows optical images of burrs before and after LPEB irradiation. Instead of the solid and brittle burrs observed on the as-drilled holes, the LPEB-irradiated burrs are thin, flexible, and skein-like following less than 20 pulses of irradiation, regardless of the other parameters. This may indicate that the resin evaporated partially, so the carbon fibers were not broken. In this case either the energy density or number of irradiation pulses was too low for the resin to evaporate, so the LPEB irradiation did not remove the uncut fibers completely. Although the sizes of the remaining burrs decreased after less than 20 pulses of irradiation, generation of the tiny skein-like carbon fibers negatively impacted the quality of the drilled holes. These skein-like burrs may have been caused by partially damaged carbon fibers. However, increasing the number of irradiation pulses to more than 30 removed almost all of the burrs. Figure 62 shows that the number of skein-like carbon fibers decreased as V_a and the number of pulses increased up to 30, beyond which they were eliminated completely. Hence, repeated irradiation pulses can be used to remove these skein-like carbon fibers. This result is in good agreement with the distribution of the remaining burr sizes, which, as shown in Figure 60(b), reduced significantly as the number of pulses increased beyond 30.

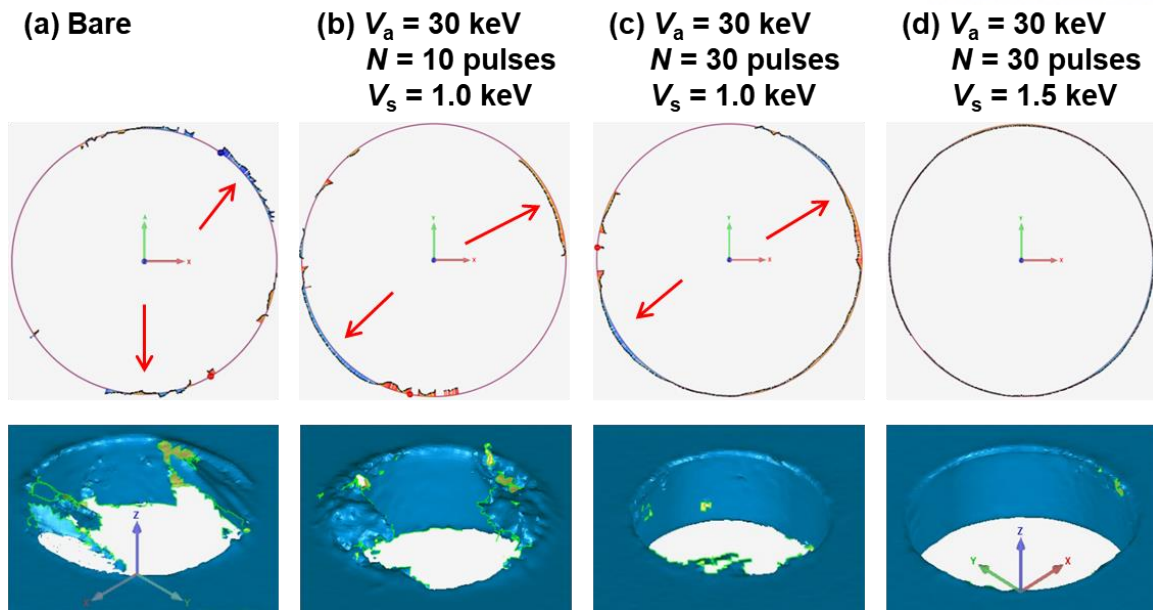


Figure 63. Representative 3D scanned geometrical features and diameter deviations of the drilled CFRP holes before and after the LPEB irradiations

The quality of holes drilled into CFRP composites can be negatively affected by burrs on their edges and surfaces. In particular, CFRP composites intended for use in vehicle bodies or aircrafts should not contain even very small burrs, as the uncut fibers can cause cracks and delamination of the stacks. These can be accompanied by fractures. Figure 63 shows a representative example of the results from the 3D geometrical scanning study, both before and after LPEB irradiation. The blue- and red-colored lines at the edge indicate where the diameter of the hole deviates from an ideal circle with a diameter of 9-mm. Figure 63 shows that the deviations among LPEB-treated holes were relatively small. It is also clear that the skein-like burrs, indicated by red arrows on Figure 63, caused larger diameter deviations. We observed a significant reduction in the average diameter deviations of the holes after LPEB irradiation. Moreover, Figure 63 (c) and (d) show that LPEB irradiation with high V_s rendered the surfaces of the holes markedly smoother. This could be due to the electrons following a spiral path with a small radius, which will penetrate material deeper than electrons on a spiral with a larger radius. LPEB irradiation with the optimal parameters resulted in drilled holes that were almost completely circular in shape and the removal of almost all of the burrs and skein-like carbon fibers.

Figure 64 shows the diameter deviations after LPEB irradiation with respect to V_a , V_s , and the number of pulses. The relationships between the diameter deviations and LPEB parameters were similar to those between the sizes of the remaining burrs and the LPEB parameters. The significant reduction of diameter deviations was observed especially with increasing pulses. The surface smoothing effect of the LPEB irradiation caused further reductions in the diameter deviation as V_s increased. It was obtained that these improvements in the accuracy of the hole shapes by varying the parameters in the same way as when the sizes of the remaining burrs were reduced. Specifically, holes with smaller remaining burrs

and more accurate hole shapes were achieved by increasing V_a , V_s and the number of pulses. It is important to note that the improvements seem to be most sensitive to the number of pulses. In the case of drilled holes in CFRP composites, the deburring performance should be assessed in terms of the geometrical accuracy of the holes. The remaining uncut fibers may degrade the quality of the holes by distorting their shape. The proposed LPEB deburring process improves the geometrical accuracy of drilled holes on CFRP composites.

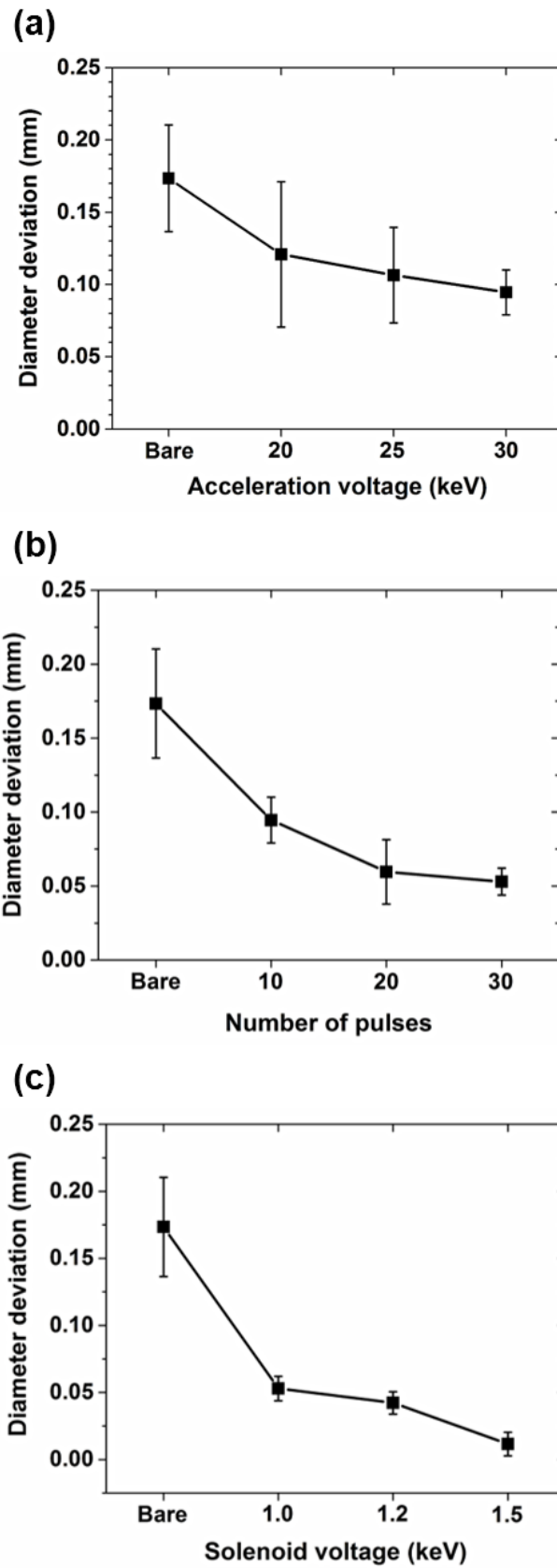


Figure 64. The diameter deviations of the drilled CFRP holes comparing to the ideal circle before and after the LPEB irradiations in terms of (a) acceleration voltage, (b) the number of pulses, and (c) solenoid voltage

5.2 LPEB manufacturing based on surface modification mechanisms

In Chapter 4, several effects of the LPEB irradiation were specified through in depth investigations on the re-solidified layer induced by rapid melting and re-solidification processes. The LPEB irradiation was turned out to have simultaneous modification effects on mechanical properties and surface stabilities. Furthermore, as illustrated in Chapter 5.1, the electron showering principle of LPEB irradiation with spiral pathway of accelerated electrons induced by solenoid voltages facilitate it to be simply adopted on complex surface patterns without any special experimental set-ups. These prevailing advantages of LPEB irradiation could be maximized when it is adopted in the field that require robust surface characteristics and superior chemical stabilities on complicated surface patterns which cannot be covered with conventional surface modification methods.

5.2.1 Superhydrophobic transformation of metallic patterns

Hydrophobic surfaces characteristic of certain metallic alloys has been intensively studied because of potential applications such as self-cleaning surfaces, for reduced liquid drag in pipes and microchannels, as the outer surface of vehicles, and for corrosion protection [130]. The fabrication of superhydrophobic surfaces has significantly advanced through the use of techniques including layer-by-layer deposition [131], electrochemical treatment [132], photolithography [133], micro/nanofabrication processes [134, 135]. The layer-by-layer deposition of hydrophobic materials on metallic alloys is one way to produce superhydrophobic surfaces. However, the bonding force between the hydrophobic film and metals is rather weak because polymers are used as the deposited materials. Micro/nano-pillars have been fabricated on a surface by laser ablation [134], wire-electric discharge machining (WEDM) [136], chemical etching [137] and micromachining [138]. Metals generally require post-processing, such as etching, to render their surfaces hydrophobic. Most of the post-processing techniques have used nonmetals to lower the surface energy, but delamination of the surface layer can lead to metal aging. However, lowering the surface energy of patterned metals directly has not been adequately investigated.

To solve certain limitations of the previous methods to fabricate durable hydrophobic surfaces, the LPEB irradiation was applied on the micropatterns of stainless steel as it can simultaneously improve mechanical properties and hydrophobicity on the metallic alloys [139]. Micropatterns were fabricated with various groove depths (d) on standard AISI 304 stainless steel using WEDM (SL400G, Sodick Inc., Tokyo, Japan) (Figure 65). The width (w) and pitch (p) of the patterns were fixed to specifically investigate the effect of d on superhydrophobic transformation. Patterns having various depths (50, 100, 150, 200 and 250 μm) were fabricated on SS304. Three independent samples were fabricated for each depth. Water was used as the working fluid for the WEDM fabrication process. The general experimental set-ups for the LPEB were also used for the irradiations.

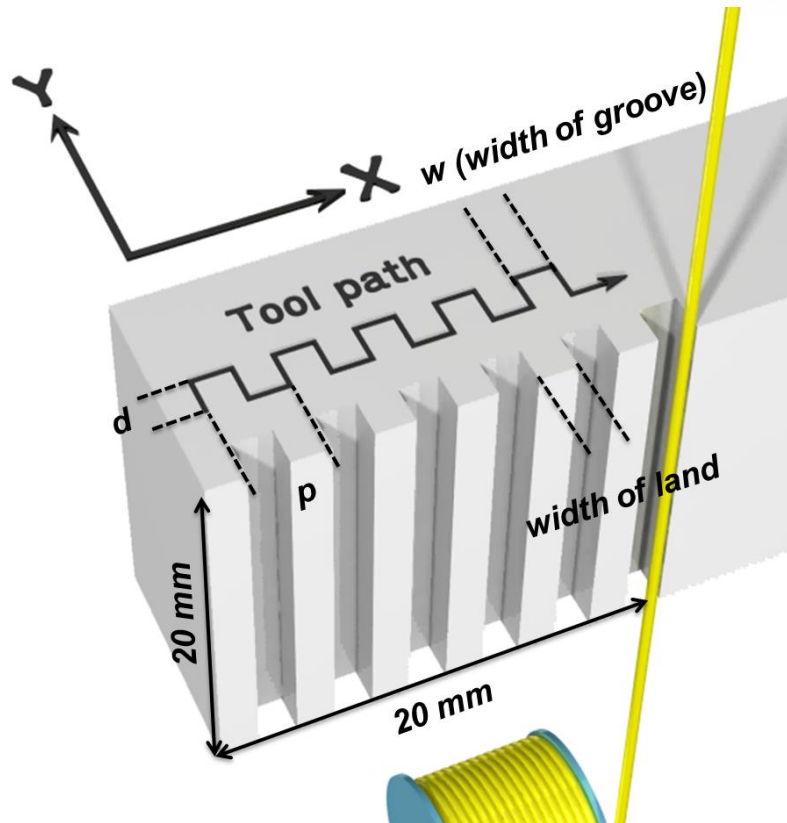


Figure 65. Schematic diagram of wire electric-discharge machining (WEDM) and variables corresponding to pattern structures

A perfectly square patterned area could not be fabricated because of the circular spark gap around the brass wire and the SS304 substrate. Figure 66 shows cross-sectional OM images of the WEDM-fabricated patterns before and after LPEB irradiation. Figure 67 indicates the measured d and width of land in terms of the d set in the tool path. The exact depths of the patterns following WEDM fabrication were relatively well matched to the d set in the tool path (within 10%). However, that was not the case for the land widths, which varied from 200 to 50 μm as d increased from 50 to 250 μm . This may have resulted from the increasing size of the areas affected by the spark gap as the penetration depth of the wire increased during discharge. Furthermore, the pattern depths were slightly less after LPEB irradiation of the WEDM-fabricated surfaces. LPEB irradiation is a process that induces rapid melting and/or evaporation of the top surface layer, followed by re-solidification. During repeated melting and re-solidification of the alloy, the pitches of the grooves could have melted and slightly evaporated, thereby reducing the pattern depth. Molten metal could flow down along the groove and re-solidify. This could account for the land widths after LPEB irradiation of the WEDM-fabricated patterns being slightly higher.

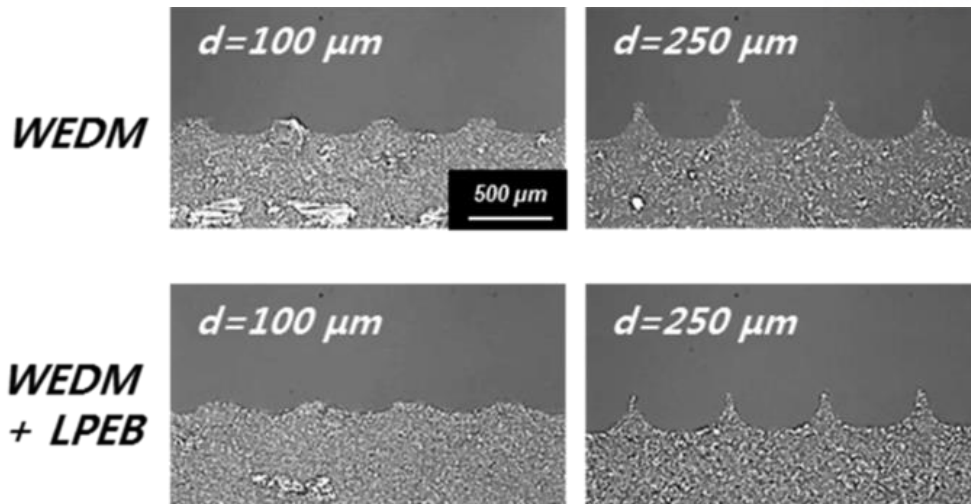


Figure 66. Cross-sectional optical microscopy images of WEDM-fabricated patterns before and after large pulsed electron beam (LPEB) irradiation

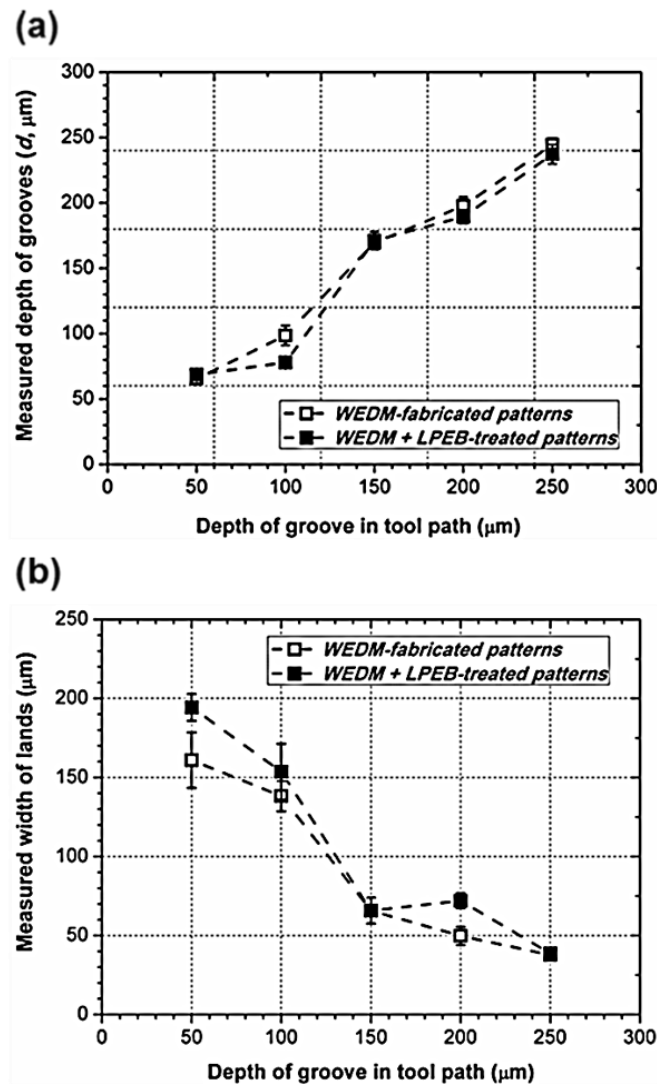


Figure 67. Measured (a) groove depth, d and (b) land width of WEDM-fabricated patterns before and after LPEB irradiation as a function of tool path groove depth

Surface roughness is one of the most important factors for controlling wetting characteristics [140]. Therefore, typically several skim cuts were made to reduce the surface roughness during WEDM fabrication. Bae et al. [136] needed at least four skim cuts to produce a roughness less than about 0.5 μm . However, in this experiment, only one skim cut was performed because the LPEB irradiation reduced the surface roughness. Figure 68 shows SEM images of the WEDM-fabricated patterns before and after LPEB irradiation. Figure 68(a) shows the surface morphology of the WEDM-fabricated patterns after only one skim cut; the surface was rough with many overthrust-like faults induced by irregular discharge along the 20-mm long wire. LPEB irradiation provided much smoother and cleaner surfaces. The surface roughness greatly decreased following the LPEB irradiation, e.g., from $4.23 \pm 1.2 \mu\text{m}$ to $0.54 \pm 0.2 \mu\text{m}$, indicating a much smoother and more uniform surface texture of the treated patterns.

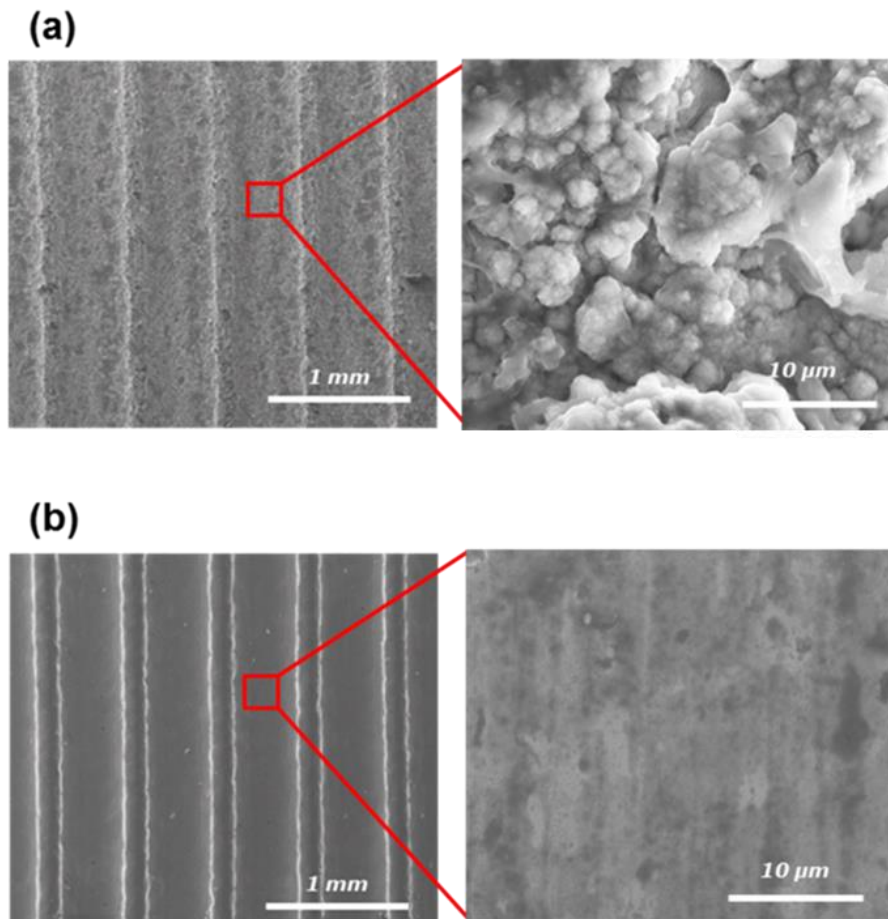


Figure 68. SEM images of WEDM-fabricated patterns (a) before and (b) after LPEB irradiation

Figure 69 shows the variation in the static contact angles (CAs) of the WEDM-fabricated patterns as a function of d before and after LPEB irradiation. The CA was measured using the sessile drop method and a drop shape analyzer (DSA100; KRÜSS Optronic GmbH, Hamburg, Germany) on three different spots for each sample at room temperature. The drop volume was fixed at 5 μl that the droplet was

placed over the least number of groove(s) when it formed Cassie-state using the volume of 5 μl . The measurements were performed in a dark room for the best DSA performance.

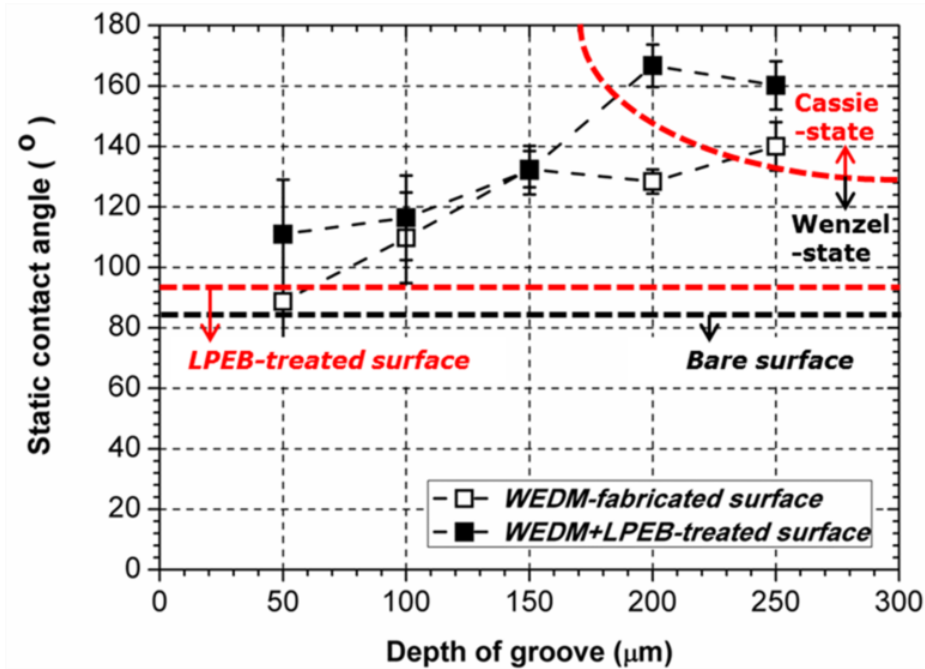


Figure 69. Contact angles of WEDM-fabricated patterns as a function of groove depth before and after LPEB irradiation

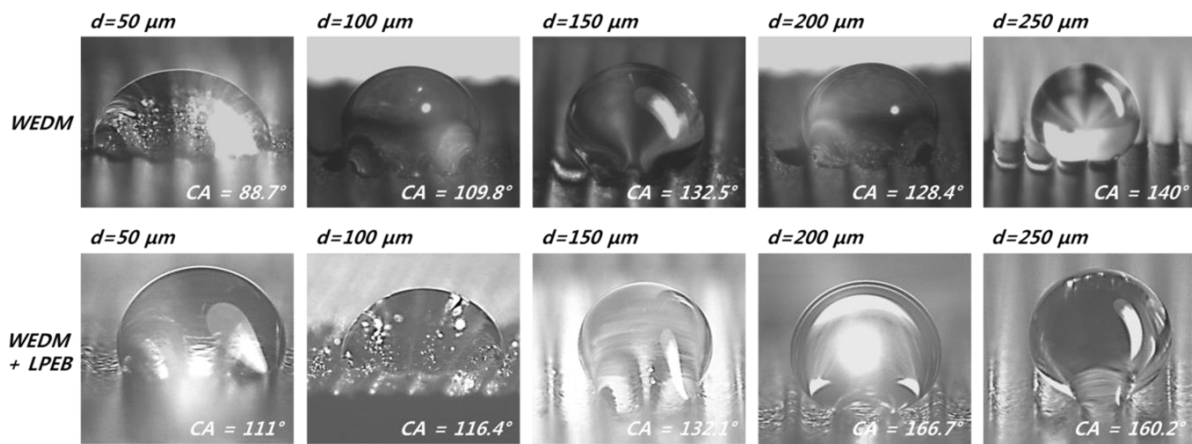


Figure 70. Variation of droplet shape as a function of groove depth before and after LPEB irradiation

The static CAs tended to increase with increasing d . Most of the CAs was higher than those measured for bare and LPEB-treated unpatterned SS304 surfaces. The CA increased from 88.7° (d : 50 μm) to 140° (d : 250 μm) for the untreated WEDM-fabricated patterns. Up to a d of 200 μm , water droplet testing indicated a Wenzel-state CA, with hemi-wicking behavior (Figure 70). A Cassie-state CA, which is also one of the most necessary characteristics to make surface hydrophobic, was observed only for those patterns with a d of 250 μm . It was possible to achieve a Cassie-state CA at a d of 200 μm for the LPEB-

irradiated patterns following WEDM fabrication. This d was smaller than that observed for the untreated WEDM-fabricated patterns (Figure 69). The static CA of the LPEB-irradiated patterns increased to over 160° at higher d than $200\ \mu\text{m}$. The CA measurements of the WEDM-fabricated patterns before and after LPEB irradiation were in good agreement with theoretical descriptions of wetting transition criteria using surface energy models that included the effect of groove shape, droplet radius and surface roughness factor. Reyssat et al. [141] assumed that grooved surfaces would be wet when the droplet in the groove contacted the bottom surface of the substrate. Based on this assumption, the following expression was derived:

$$\delta = w^2 / R \quad (31)$$

where δ denotes the penetration depth of a droplet in the groove, w denotes the width of groove, and R is the radius of the droplet. For Wenzel-state wetting, penetration of a water droplet into a groove occurs when $\delta > d$. Thus, the wetting condition that penetration of a water droplet occurs could be expressed as

$$R = w^2 / d \quad (32)$$

where d denotes the depth of groove. Eq. (32) indicates that a higher d would reduce the penetration of water into the grooves and maintain a Cassie-state CA on the patterns.

Although Eq. (31) and (32) describe the effect of d on the wetting properties of the patterns, the effect of LPEB irradiation on the hydrophobicity of the patterns remained unclear. Surface roughness was the greatest visualized difference between patterns before and after LPEB irradiation; thus, a simple modeling of the surface energy considering the roughness factor was adopted. Bae et al. [136] and Quéré [142] described surface energy models that considered the roughness factor, i.e.

$$dE = \gamma_{LA}(w - r(2d + w)\cos\theta)dx \quad (33)$$

where dE is the change of surface energy, γ_{LA} is the surface energy of the liquid/air interface, and r is the roughness factor. The roughness factor is a ratio of the real surface area to the geometric surface area; it could be affected by the pattern structures and the surface roughness of patterns [143]. All systems seek the lowest energy level at system boundaries. Thus, the critical transition criterion for the Wenzel-to-Cassie state transition can be expressed as [136]

$$\cos \theta_c = \frac{w}{r(2d + w)} \quad (34)$$

where θ_c denotes the critical angle of the Wenzel-to-Cassie transition; a water droplet can maintain a Cassie-state CA above the critical angle. From Eq. (34), a lower roughness factor leads to a lower critical angle for the Wenzel-to-Cassie transition in a hydrophilic region ($\theta < 90^\circ$). Most engineering stainless steels are barely hydrophilic; thus, it is reasonable to evaluate the effect of surface roughness on the wetting transition using Eq. (34).

Table 12. Roughness factors, radius of droplets, and w^2/d of WEDM-fabricated patterns before and after the LPEB irradiation

Depth of grooves (μm)	WEDM			WEDM+LPEB		
	Roughness factor (r)	Droplet radius (μm)	w^2/d	Roughness factor (r)	Droplet radius (μm)	w^2/d
50	4.13	1344 \pm 320	5000	1.51	1210 \pm 270	5000
100	4.72	974 \pm 110	2500	1.73	1090 \pm 96	2500
150	5.31	1096 \pm 43	1667	1.95	1006 \pm 22	1667
200	5.9	1199 \pm 31	1250	2.17	1233 \pm 25	1250
250	6.49	1236 \pm 29	1000	2.38	1333 \pm 14	1000

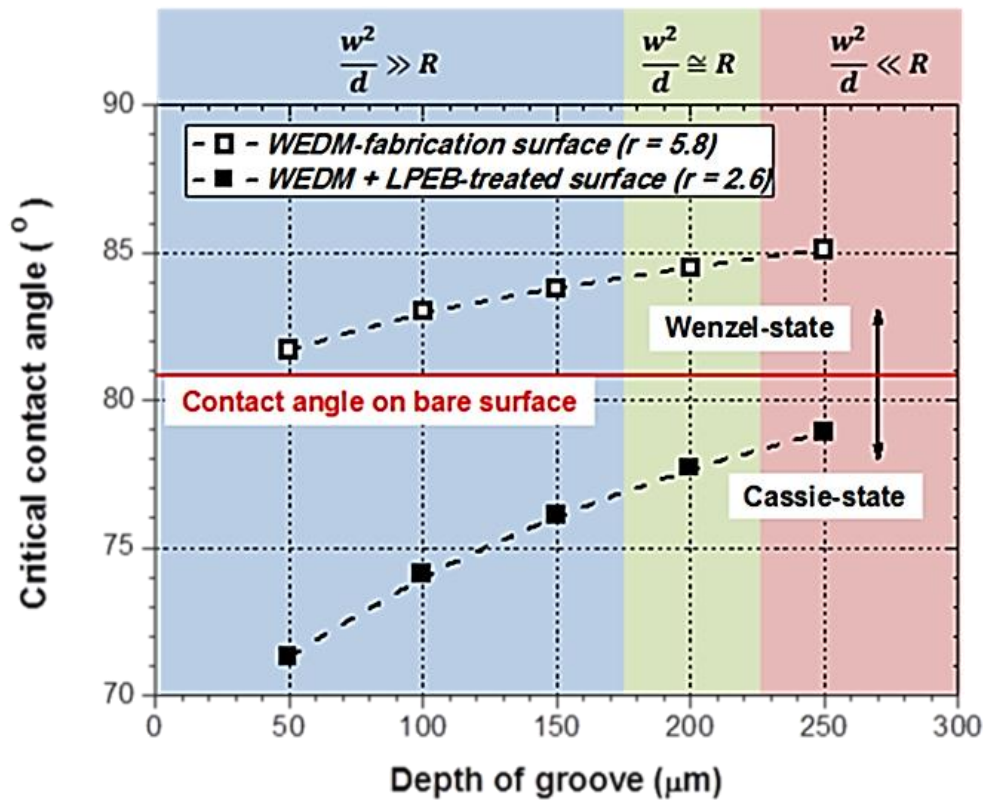


Figure 71. Quantitative comparisons between theoretical descriptions and experimental contact angles for Wenzel-to-Cassie transition

Our measurement of static CAs supported these predictions. Table 12 shows roughness factors, radius of droplets, and w^2/d values corresponding to Eq. (32) and (34). Figure 71 shows quantitative comparisons between theoretically estimated wetting conditions and critical angles of Wenzel-to-Cassie transition in terms of d and roughness factors [142]. The roughness factors on WEDM-fabricated patterns before and after LPEB irradiation were measured and calculated from white-interference micrographs. As the patterns with d between 50 and 150 μm (blue shaded in Figure 71) attained much larger value of w^2/d than R , Wenzel-state CAs were achieved on those patterns before and after LPEB irradiation (Figure 70). For pattern with groove depth of 250 μm (red shaded in Figure 71), in contrast, w^2/d value was smaller than R indicating Cassie-state and it was well matched to experimental results (Figure 70). Although the structural effect of the patterns affecting the states of droplets could be clearly explained by Eq. (31) and (32), the obscure region indicated by $w^2/d < R$ (green shaded in Figure 71) was needed to be described further considering roughness variation (Eq. (34)). The effect of reduced roughness factor on the state of CA was clearly shown at the $w^2/d < R$ region. The only LPEB-irradiated pattern showed Cassie-state when $w^2/d < R$. This could be resulted from the decrease of Wenzel-to-Cassie transition critical angle after LPEB irradiation as illustrated in Figure 71; the critical angle on WEDM-fabricated surface which was higher than CA of the bare surface was significantly reduced to lower than CA of the bare surface. Thus, it is reasonable to conclude that reduced roughness factor following LPEB irradiation contributed to achieve Cassie-state at lower d on LPEB-irradiated patterns. Figure 72 shows the direct comparison of droplet shape for the untreated and LPEB-irradiated WEDM-fabricated patterns. Although both samples were fabricated with the same groove depth (200 μm), water penetration was observed only for the non-irradiated WEDM-fabricated patterns. This was attributed to the lower surface roughness factor and smaller θ_c caused by the LPEB irradiation.

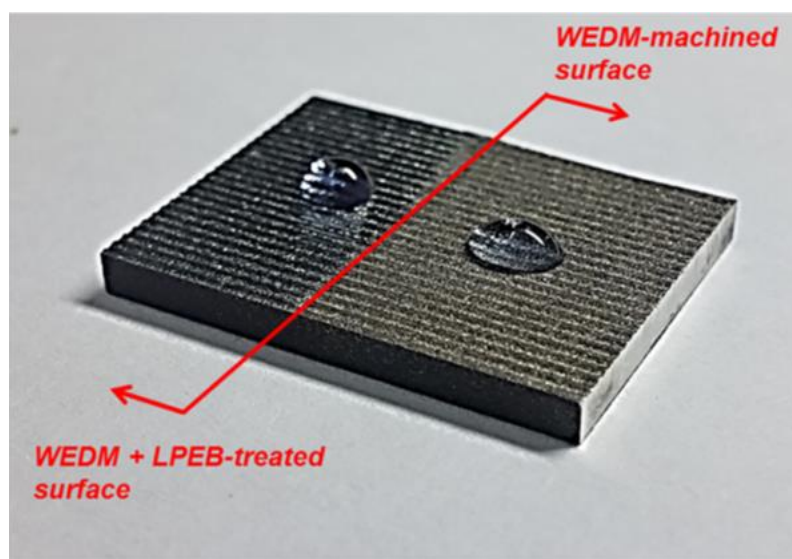


Figure 72. Comparison of liquid spread along the grooves of a WEDM-fabricated surface before and after LPEB irradiation ($d = 200 \mu\text{m}$)

Structural wettability can modify the shape of patterns on SS304, as noted above. Changes in chemical wettability can also affect the Wenzel-to-Cassie CA transition. The chemical wettability of a material is directly related to the surface functional groups. Functional groups affect wetting characteristics because they are hydrophilic or hydrophobic, depending on their polarities. Figure 73 shows the attenuated total reflection infrared (ATR-IR) spectra of WEDM-fabricated patterns before and after LPEB irradiation and changes of spectra before and after 2 h wetting. Major absorption bands detected on the as-prepared WEDM-fabricated patterns (Figure 73(a)) was attributed to C-O functional group, which is considered as hydrophilic group. After 2 h wetting with distilled water, major absorption bands were significantly changed to C=O, C-O, C-H and N-H and O-H functional groups, respectively. Those groups have bent and polarized structures. These are also considered as hydrophilic groups [144]. In contrast, those hydrophilic functional groups were either absent or significantly reduced by the LPEB irradiation (Figure 73(c)). Only small amount of the C=O peak was observed after 2 h wetting (Figure 73(d)). These variations of surface contaminations are highly related to the stability of hydrophobicity [145, 146], and were well matched to the transient CAs measured during 2 h.

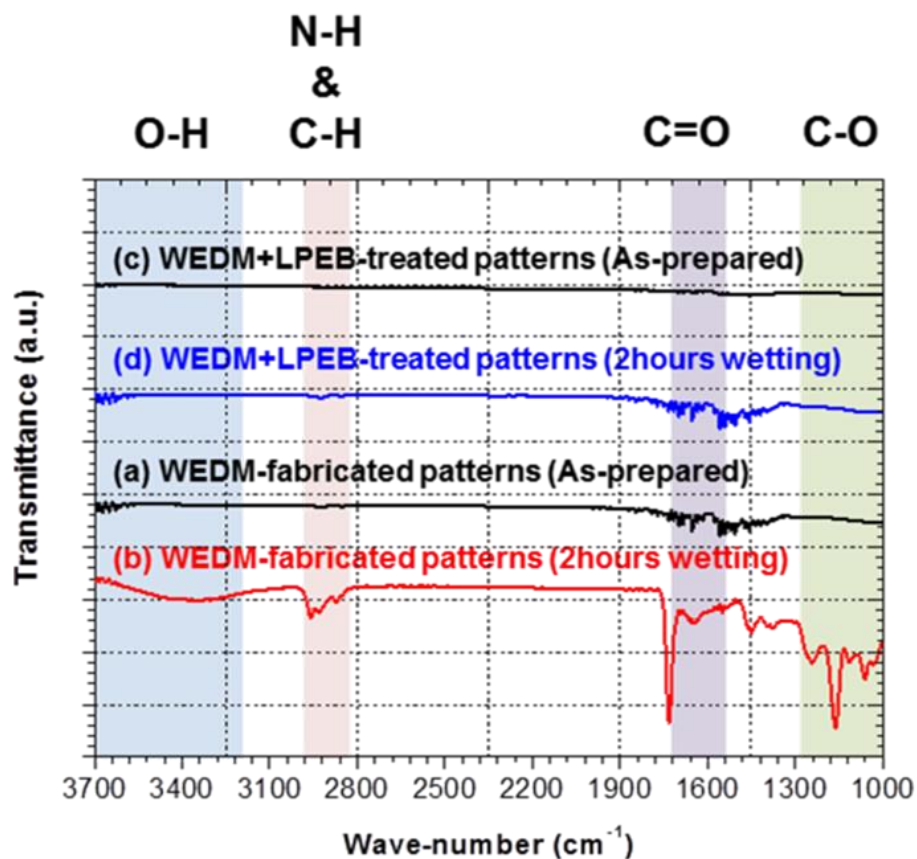


Figure 73. Attenuated total reflection infrared (ATR-IR) spectra of WEDM-fabricated patterns (a) before and (b) after LPEB irradiation

Figure 74 shows the variation of CAs on WEDM-fabricated pattern ($d = 250 \mu\text{m}$) before and after LPEB irradiation in terms of time. The WEDM-fabricated pattern which initially had Cassie-state showed Wenzel-state transition after ~ 10 min contact with droplet, and the transient CA ratio to initial CA decreased continuously to 0.3 after 2 h. However, LPEB-irradiated pattern maintained Cassie-state during 2 h of CA measurement; transient CA ratio to initial CA was only reduced to 0.85 after 2 h. It is likely that large amount C and O was emerged after WEDM process due to sparks as summarized in Table 13. However, C-, O- and N- bonds were broken by the large kinetic energy of LPEB electrons. Thus it is easier for hydrophilic functional groups to be formed on WEDM-fabricated pattern comparing to LPEB-irradiated pattern. The reduction in C and O after LPEB irradiation on WEDM-fabricated pattern could lead outstanding stability of hydrophobicity preventing hydrophilic contaminations on the surface.

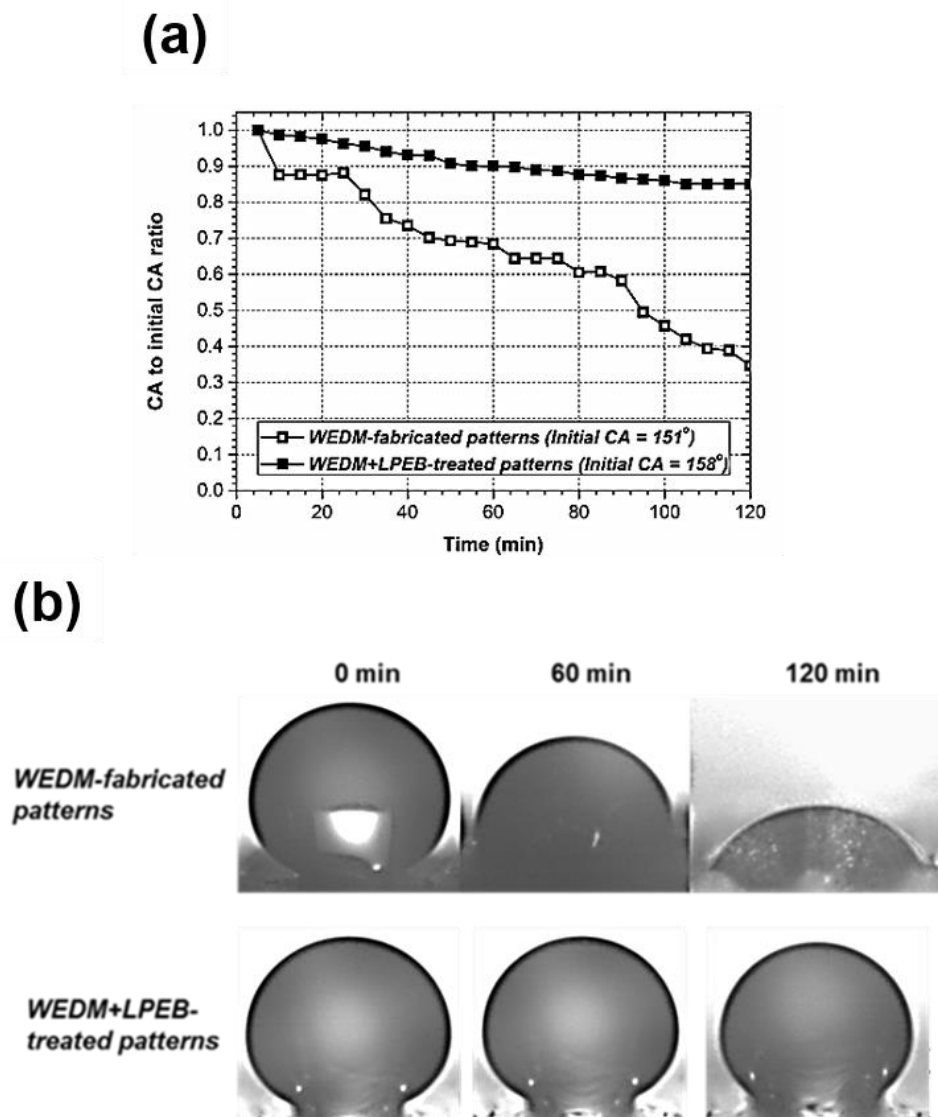


Figure 74. (a) Transient CA ratios to initial CA on WEDM-fabricated patterns before and after LPEB irradiation and (b) optical microscopy images of droplets during two hours of CA measurements ($d = 250 \mu\text{m}$)

Table 13. EDX chemical compositions of bare and WEDM-fabricated patterns before and after the LPEB irradiation

Element	Atomic %		
	Bare	WEDM	WEDM + LPEB
C	13.56	25.64	12.16
O	5.31	19.16	6.86
Cr	16.03	10.33	15.62
Ni	8.29	11.31	8.5
Fe	56.81	33.56	56.86

To conclude, a durable hydrophobic surface was fabricated on SS304 using WEDM and LPEB irradiation; the measured CA was 166.7°. The hydrophobicity with Cassie-state CA was obtained at a shallower groove depth after LPEB irradiation. This water-repellent characteristic was attributed to the smoother surface caused by the LPEB irradiation. Moreover, hydrophilic functional groups on the surface were mostly eliminated by LPEB irradiation, which further increased the hydrophobicity of the patterned surfaces. The hydrophobicity on the LPEB-irradiated surface was maintained during long-term contact with droplets. The electrochemical stability of the surface was also greatly improved by LPEB irradiation.

5.3 LPEB manufacturing based on charge transfer mechanisms

In Chapter 4, the LPEB irradiation was applied on bulk materials and the macroscale application of the process was examined specifying modification principles of surface properties. In Chapter 5.1 and 5.2, microscale applications of the LPEB irradiation on eliminating micro-sized burrs of metallic alloys and CFRP composites were investigated based on the melting mechanisms induced by the irradiations. Furthermore, the special energy transfer mechanism of the LPEB through accelerated electrons, nanoscale applications of LPEB irradiations on manufacturing processes could be studied based on the charge transfer mechanisms of the electron beam irradiation.

5.3.1 Design of experiments and materials

A welding process of metal nanowires (NWs) is one of the most promising manufacturing process which can be further modified by replacing previous method with LPEB irradiations. Most recently, noble metal NWs such as Cu and Ag percolation networks have been widely used as transparent and flexible conductors. Randomly distributed percolating networks of NWs are relatively easy to produce, as they use a simple, reproducible solution process including spin- or spray-coating. Despite high transmittance and low sheet resistance (R_s), spin-coated NWs are weak under bending or stretching forces, as the junctions have poor mechanical resilience with weak attractive forces between each NW, resulting in an extremely large contact resistance. Hence, they can be easily broken under shear stress

and strain. Many studies have suggested flexible electronic devices using NWs, however these devices showed performance degradation under cyclic deformation through fractures in NWs and junctions [147, 148]. In this context, post processing techniques have been adopted for NW percolating networks, to enhance mechanical properties by inducing welded junctions. The most widely used methods are thermal-annealing. However, the uniformity of welded NW percolation networks cannot be guaranteed because the thermal annealing transfers the same amount of heat to a randomly distributed NWs having different density of junctions.

Thus, the LPEB irradiation was attempted for fabrication of flexible and transparent conductor with welded AgNW percolation networks [149]. In this approach, AgNW networks above the percolation threshold were welded using LPEB irradiations to enhance mechanical flexibility without significant reduction in transmittance and increase in R_s during bending cycles. The LPEB-welded AgNW electrodes were compared to pristine and thermally annealed AgNW electrodes in terms of the change in R_s over a number of bending cycles. Furthermore, polymer based light-emitting diodes (PLEDs) and resistive touch-panels fabricated using the LPEB-welded electrodes are demonstrated to confirm the mechanical durability and the potential applicability of the resultant transparent flexible electrode in practical optoelectronic applications.

The AgNW percolation networks were first constructed by spin-coating above the percolation threshold. A 0.5 wt. % isopropyl alcohol (IPA)-based suspension of AgNWs (Nanopyxis) with a length $25 \pm 5 \mu\text{m}$ and diameter $36 \pm 5 \text{ nm}$ was prepared. The AgNW networks were obtained on a thin polyethylene terephthalate (PET) film (thickness: 0.1 mm) with dimensions of 15 mm x 15 mm (Figure 75). The spin rate and time were fixed at 1500 rpm and 90 s respectively, as these are optimized conditions in terms of uniformity, transmittance, and electrical conductivity. On the spin-coated AgNW percolation networks, thermal-annealing and LPEB irradiation were adopted. Thermal-annealing was performed under ambient conditions at 130 °C for 10 min. LPEB irradiation was conducted for a single pulse at an acceleration voltage of 5 kV.

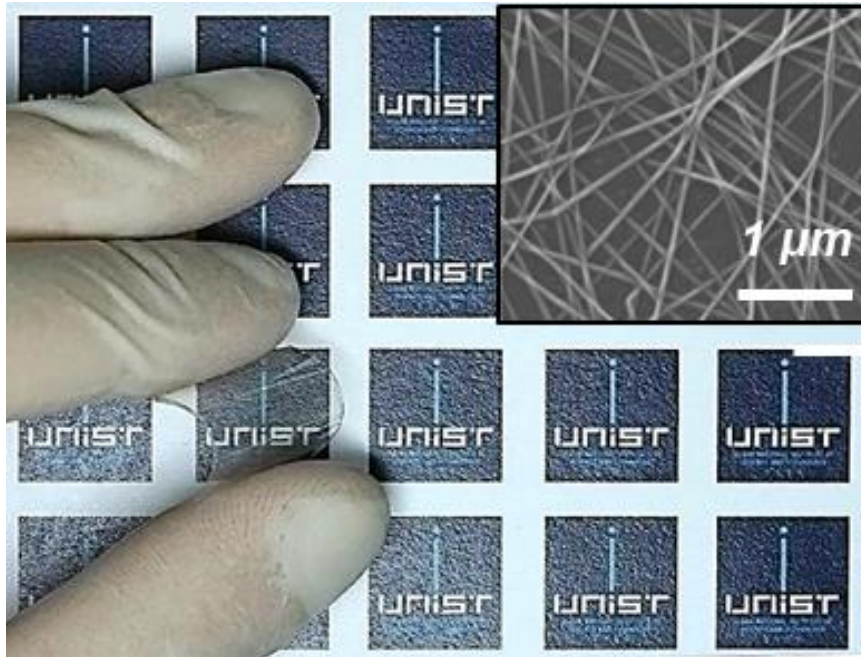


Figure 75. Photograph of spin-coated flexible AgNW electrode fabricated on a polyethylene terephthalate (PET) film

5.3.2 Nanostructures of welded AgNWs

The pristine AgNWs showed relatively low electrical conductivity, likely resulting from high contact resistance and weak junctions in NW–NW bonding. Figure 76 shows a schematic diagram of AgNW welding processes using thermal-annealing and LPEB irradiation. Thermal-annealing heats the entire AgNW network simultaneously whereas LPEB irradiation uses accelerated electrons to transfer energy. Figure 77 shows SEM images of the as-prepared, thermally annealed and LPEB-welded AgNW percolation networks. As shown in Figure 77(a), the NW–NW junctions of the as-prepared AgNWs showed only physical contact; however, the AgNW junctions were clearly welded following thermal annealing (Figure 77(b)) and LPEB irradiation (Figure 77(c)). These welded junctions may lead to continuously connected AgNW networks under substrate bending and significantly reduce the contact resistance when compared with that of the as-prepared AgNWs. Although larger LPEB acceleration voltages could improve the mechanical properties, a voltage of 5 kV was used, as higher voltages could degrade the surface texture and result in the formation of metallic bubbles at the end of the NWs (Figure 77(d)), which is a similar phenomenon observed during the LPEB deburring.

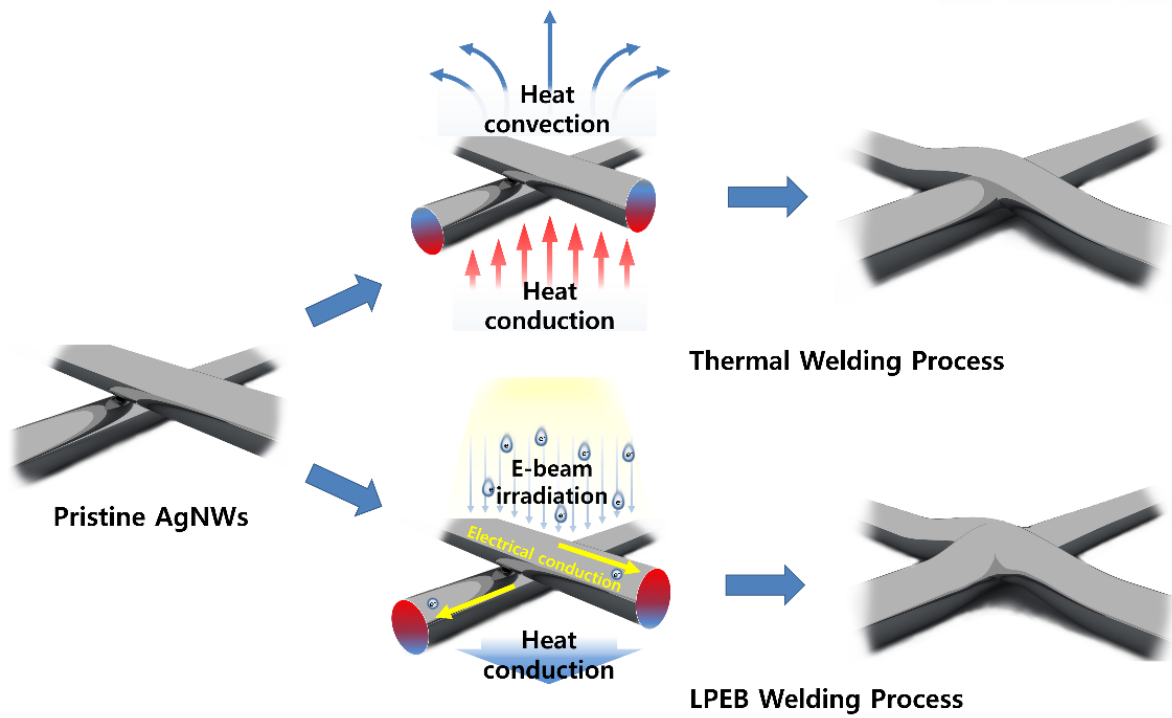


Figure 76. Schematics of thermal annealing and LPEB welding on AgNWs

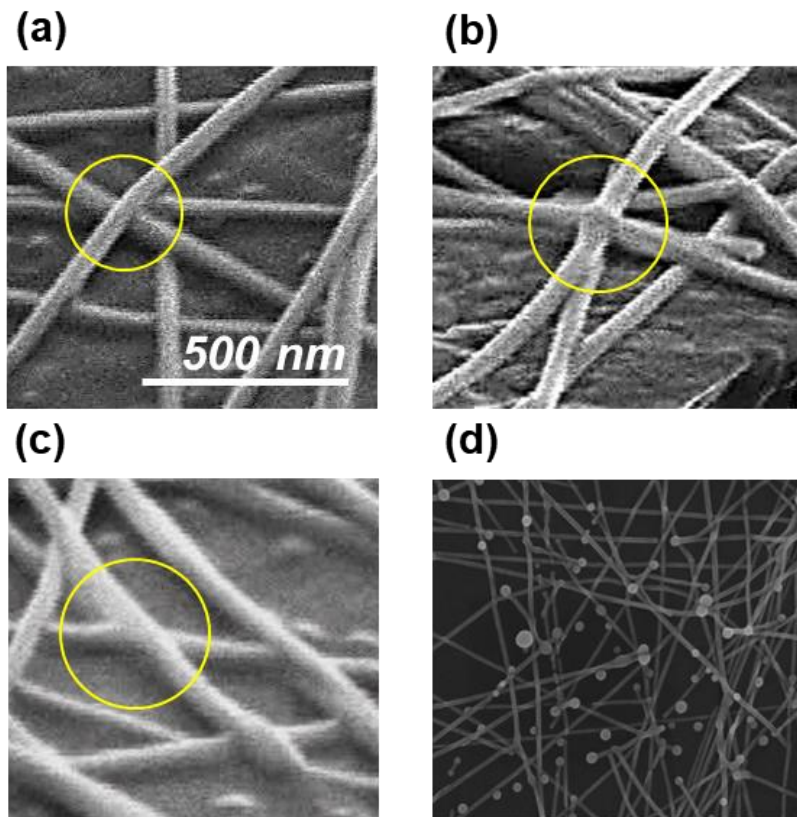


Figure 77. SEM images of AgNW junctions on percolation networks following (a) spin-coating, (b) thermal annealing, (c) LPEB welding and (d) bubbles generated on the edges of AgNWs after the LPEB welding process at acceleration voltage over 5 kV

Thermal-annealing and LPEB irradiation may also modify the mechanical properties of AgNWs and junctions. The most significant difference is that of the heat transfer mechanism. In the case of thermal-annealing, melting and re-solidification of the AgNWs at junctions are relatively slow due to continuous heat transfer across the whole processing time. In contrast, LPEB irradiation induces a rapid thermal gradient on substrates, leading to a fast melting and re-solidification process. As well explained in previous chapters, metals can also attain a phase transformation with amorphous structure; this phase transformation is commonly considered as a primary cause of modified mechanical properties including hardness and modulus.

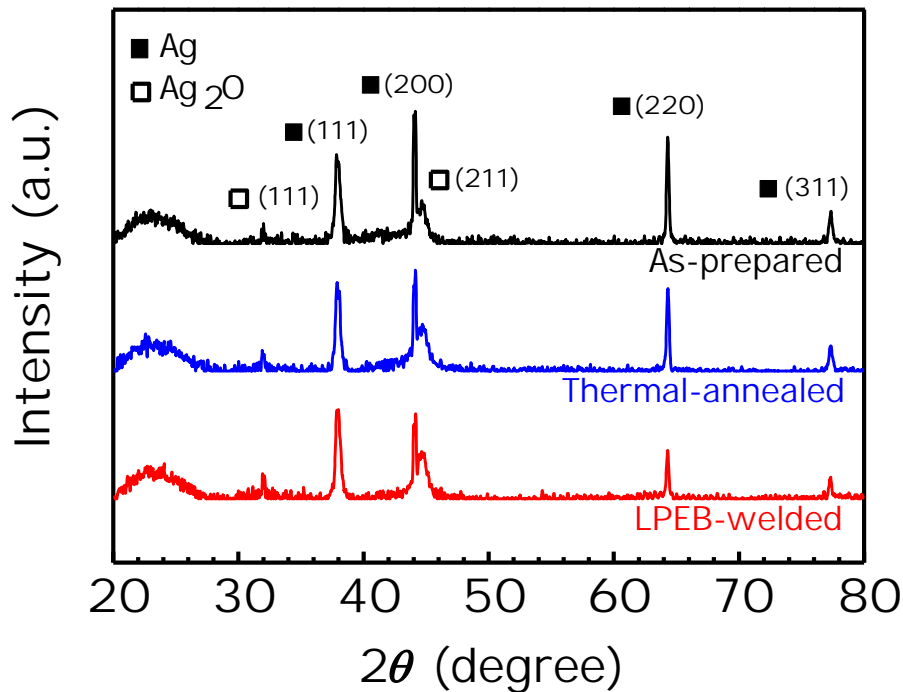


Figure 78. XRD peaks of as-prepared, thermally annealed, and LPEB-welded AgNWs

Figure 78 compares XRD patterns of the as-prepared, thermally annealed, and LPEB-welded AgNWs. The pristine AgNWs possess a face-centered cubic(FCC) structure synthesized with a certain preferred plane immediately after spin-coating. After thermal-annealing, the crystallinity of AgNWs is decreased slightly, as evidenced by the decrease in relative intensity of the (200) plane. However, no significant change in texture (preferred orientation) is observed following thermal-annealing. In case of the LPEB-welded AgNWs, a clear change in texture from (200) to (111) plane and a further reduction in the relative intensity when compared with those of as-prepared and thermally annealed AgNWs are observed. Moreover, changes in crystallinity can be estimated from the Bragg angle (θ) and full width at half-maximum (FWHM) of the main peak. Using Scherrer equation, the size of ordered crystalline domains (τ) can be estimated: $\tau = K\lambda/\beta \cos \theta$, where K is a dimensionless shape factor, λ is the X-ray

wavelength, and β is the FWHM [150]. As described in the Scherrer equation, a larger value of β and smaller θ denote smaller crystallites. The FWHM of the thermally annealed AgNWs is increased slightly to 0.354 ($\theta = 22.074^\circ$) and that of the LPEB-welded AgNWs is increased significantly to 0.421 ($\theta = 13.93^\circ$), when compared with that of the as-prepared AgNWs ($\beta = 0.310$ at $\theta = 22.074^\circ$).

5.3.3 Electrical properties of welded AgNWs

There are two competing effects arising from the decreased crystallinity. First, the loss of crystallinity is strongly related to the mechanical properties of each AgNWs, as metals with crystalline structures can be plastically deformed, or fail through slip processes. The change in XRD patterns of the three samples indicate that the mechanical properties of the AgNW percolation networks is likely to be enhanced most after LPEB irradiation. This could be due to the simultaneous loss of crystallinity and reduction in crystallite size [151]. In contrast, the higher crystallinity of conductive metals leads to a higher electrical conductivity [152]. Consequently, the significant decrease in crystallinity following LPEB irradiation could adversely affect the electrical conductivity of AgNWs initially synthesized in a single crystalline direction. The main advantages of LPEB irradiation for welding of AgNW percolation networks are demonstrated from changes in R_s following thermal-annealing and LPEB welding. Despite competing effects following changes in crystallinity, R_s was reduced considerably after thermal-annealing and LPEB irradiation. It appears that the reduction in electrical conductivity caused by the loss of crystallinity after LPEB irradiation was compensated by the decreased contact resistance at NW–NW junctions. The as-prepared AgNWs showed a relatively high R_s ($\sim 28.08 \Omega/\text{sq}$) because of the high contact resistance of NW–NW junctions in this structure. After thermal-annealing, R_s was reduced to $\sim 18.57 \Omega/\text{sq}$ because of the decrease in junction contact resistance after welding, as shown in Figure 77. A further reduction in R_s was observed after LPEB welding, down to $12.63 \Omega/\text{sq}$. In addition to the improved R_s of AgNWs following this process, there was almost no loss of optical transmittance and haze after each welding process (transmittance $>90\%$), as shown in Figure 79.

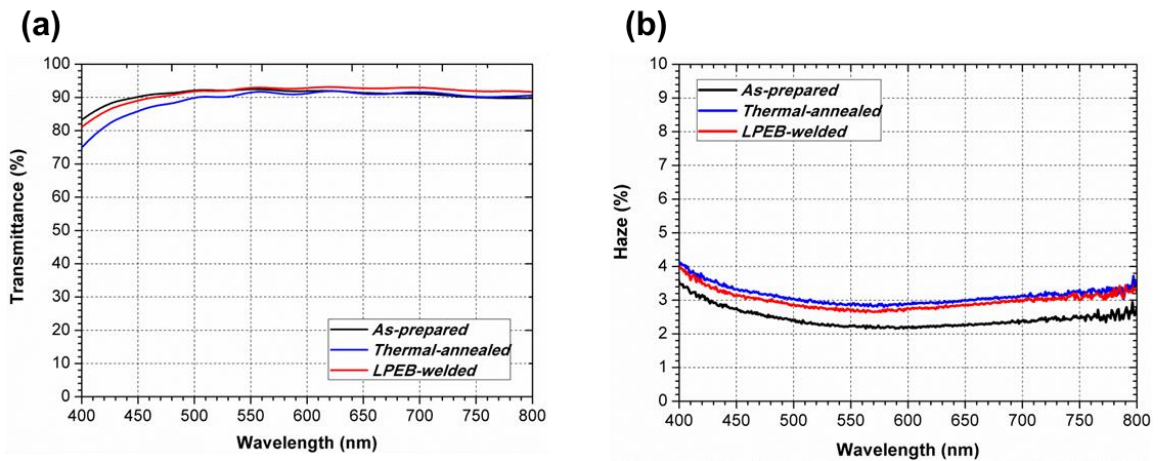
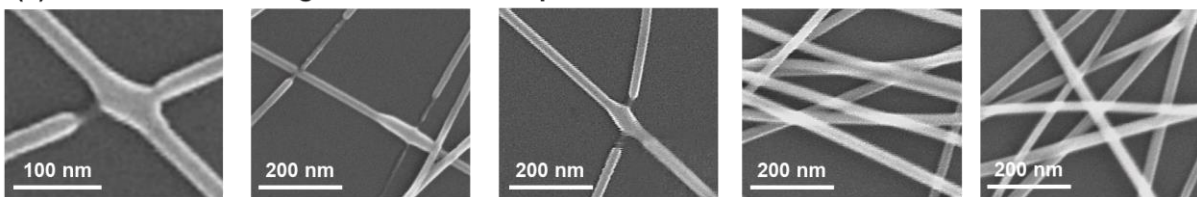


Figure 79. (a) Transmittance and (b) haze of the as-prepared, thermally annealed, and LPEB-welded AgNWs fabricated on a PET film

This could be a result of the different mechanisms arising from each welding method. Thermal-annealing is a bottom-to-top heat conduction process that continuously transfers heat through the whole area; hence different points on the surface would receive the same amount of heat from the heat source even if the density of the AgNW at each point is different. However, the heat needed to weld AgNWs is proportional to the density of NW-NW junctions; thus, the melting level varies depending on the uniformity of AgNWs during thermal-annealing as shown in Figure 80(a). In contrast, LPEB irradiation is a top-to-bottom energy transfer process, using accelerated electrons, with a larger amount of energy transferred in a much shorter time ($\sim 2 \mu\text{s}$). Some electrons transfer their energy directly and induce temperature elevation due to joule heating; thus, the AgNW itself acts as a heat source. This implies that, during LPEB irradiation, heat is induced and spread along AgNWs depending on AgNW and junction density (Figure 76).

(a) Thermal-annealed AgNWs at 5 different points



(b) LPEB-welded AgNWs at 5 different points

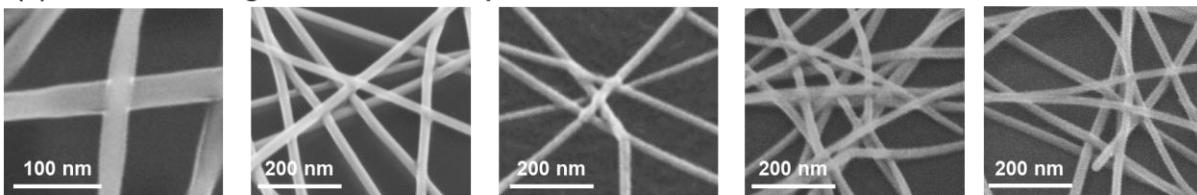


Figure 80. SEM images on AgNWs at five different points following (a) thermal annealing and (b) LPEB welding

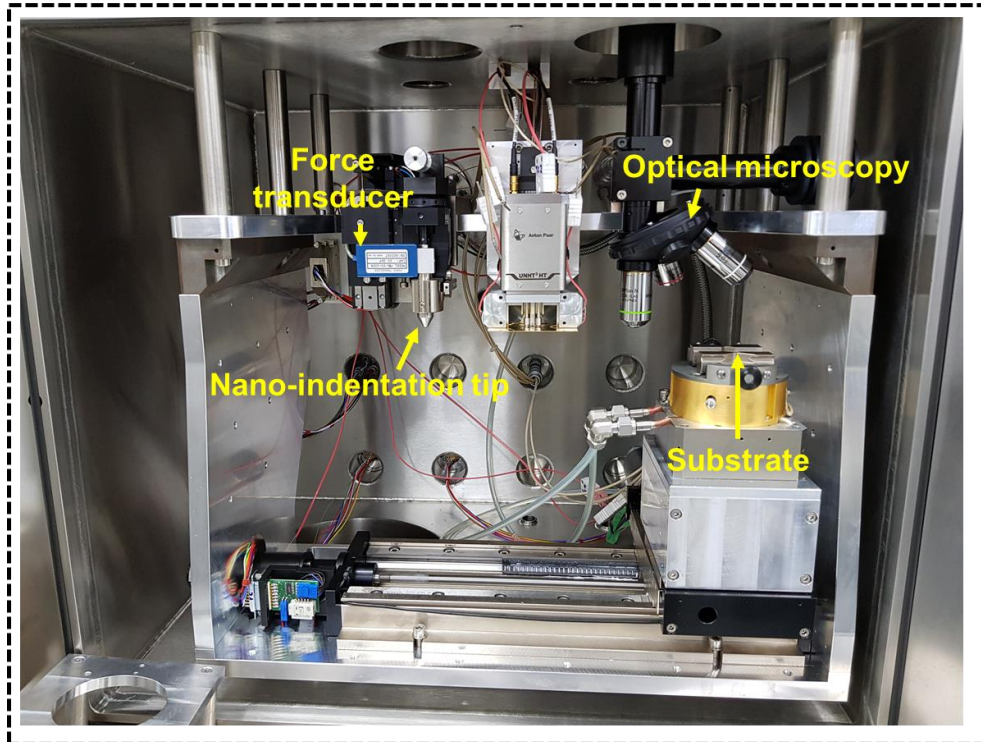
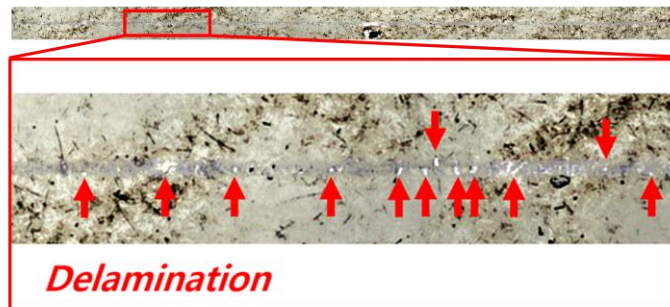
Vacuum chamber

Figure 81. Experimental setup for the nano-scratch tests

The mechanical properties of the AgNW percolation networks before and after the welding processes were investigated by nano-scratch tests using nano-indentation equipment (UNHT³ HT, *Anton Paar*). Figure 81 shows the photograph of the experimental setup used for nano-scratch test. The scratching equipment consisted of a diamond-coated nano-indentation tip ($\theta_{\text{tip}} = 100^\circ$), a force transducer, X/Y translation stages, and an optical microscope to capture the panorama images on the scratched tracks. The tests were performed at a normal force of 10 mN applied at a scratching speed of 1 mm/min along a total scratching length of 1 mm. The tests were performed inside a vacuum chamber.

(a) As-prepared AgNWs



(b) Thermal-annealed AgNWs



(c) LPEB-welded AgNWs

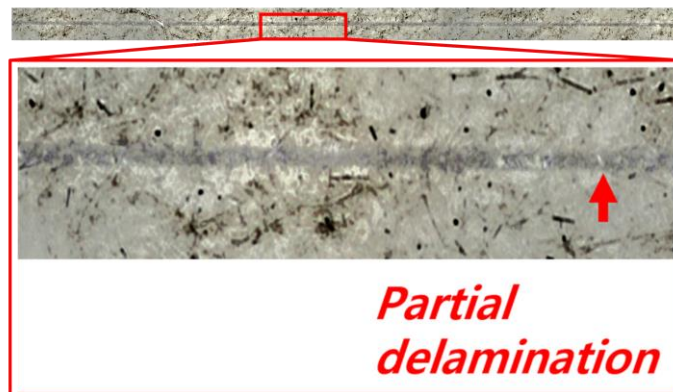


Figure 82. Optical micrographs on the scratch tracks after tests on (a) as-prepared, (b) thermal-annealed, and (c) LPEB-welded AgNW percolation networks

Figure 82 shows the panorama images and magnified images acquired on the scratch tracks after the nano-scratch tests performed on the as-prepared, thermal-annealed, and LPEB-welded AgNW percolation networks. Several delamination defects were observed after the scratch test on the as-prepared AgNWs due to disconnection of the physically contacted NW-NW junctions and lack of sufficient mechanical properties. In contrast, a reduced density of delamination was observed for thermally annealed AgNWs due to the modified mechanical properties at the welded junctions.

However, some delamination defects and partially damaged areas were still observed irregularly following the scratch test. These inferences indicate that thermal annealing cannot provide a uniform welding quality on randomly distributed AgNW percolation networks, which is well described in Figure 80(a). In contrast, the LPEB-welded AgNWs showed only few damaged areas after the scratch test. As shown in Figure 82(c), most of the regions were protected from delamination and damage of percolation networks. Also, the scratched track formed on the LPEB-welded AgNWs showed a uniform width along the scratching length. This indicates an uniform welding of AgNWs during LPEB as indicated in Figure 80(b).

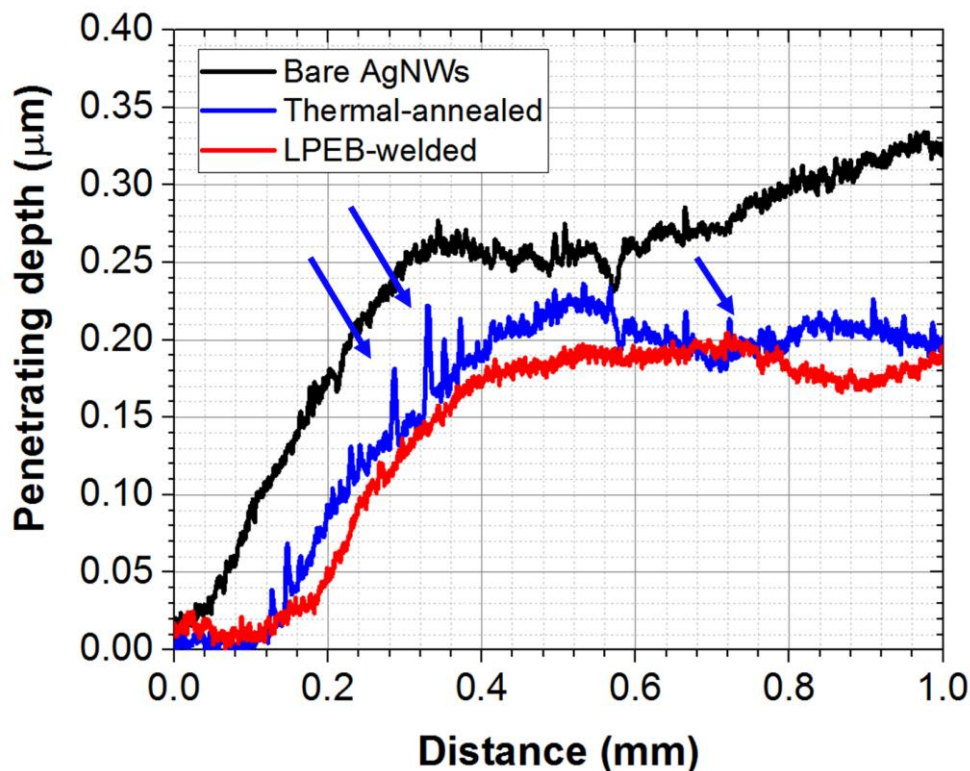


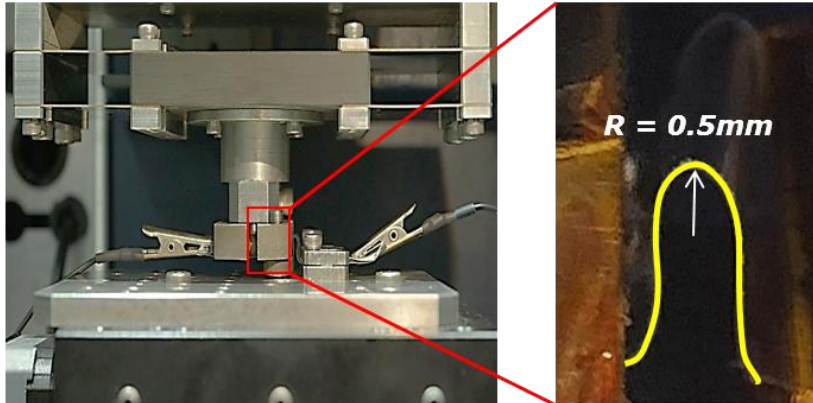
Figure 83. Penetrating depths of the nano-indentation tip in terms of the scratching distance

In addition, for the quantitative evaluations of mechanical properties, penetrating depths were simultaneously measured during the scratch tests. Figure 83 shows the penetrating depth of nano-indentation tip in terms of the scratching distance. The tip penetrated over 300 nm along a 1-mm scratching length on the as-prepared AgNWs, which means that the AgNWs were perfectly damaged at a normal force of 10 mN. In case of thermally annealed and LPEB-welded AgNWs, the penetration depths were similar at the end of tests. The penetrating depth was reduced by about 38 % following the welding of NW-NW junctions. However, a large fluctuation of penetrating depth could be observed as indicated by blue arrows in Figure 83. This reflects the irregular mechanical properties on the thermally annealed AgNWs. Thus, it could be concluded that much stronger junction contacts could be

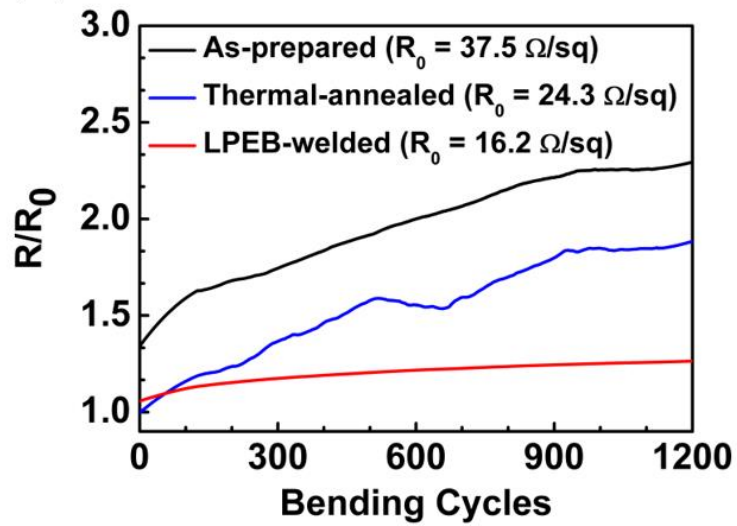
formed by the LPEB welding, resulting in a stable connection of the percolation networks. Furthermore, the uniformity of AgNW percolation networks can be guaranteed as the LPEB welding has resulted in sufficiently and uniformly re-solidified junctions throughout the whole area of percolation thresholds.

The modified mechanical properties were well reflected under cyclic bending and matched to the theoretical arguments about the superior mechanical properties of LPEB-welded AgNWs (Figure 84). The modified mechanical flexibility of welded AgNW percolation networks was well projected in the change in R_s during the cyclic bending test at a r_b of 500 μm . The R_s of as-prepared AgNWs increased significantly, up to $\sim 35\%$ of the initial value, as soon as the bending was initiated, and then increased continuously following repeated bending cycles, reaching 2.3 times the initial R_s value after 1000 bending cycles (Figure 84(b)). The thermally annealed AgNWs maintained a constant value of R_s at the start of bending cycles, but showed a continuous increase with repeated bending cycles. In contrast, R_s of LPEB-welded AgNWs remained at a relatively low level after the cyclic bending test. An increase in R_s of around 30% was observed after 1200 bending cycles. The stability of LPEB-welded AgNWs was also demonstrated in a slow single bending cycle. As shown in Figure 84(c), the R_s of as-prepared AgNWs was increased by up to 50% upon bending at a r_b as small as 500 μm . Since the as-prepared AgNWs contain only physical contacts, the junctions are highly susceptible to stress and strain, hence R_s may be highly irregular even with each individual bend in the same test. This irregular change in R_s in a single bending cycle was also observed in the thermally annealed AgNWs. The variation in R_s was significantly different for each cycle, between $\sim 10\%$ to $\sim 40\%$. In contrast, the LPEB-welded AgNWs showed superior flexibility, preserving R_s within $\sim 5\%$ upon each bending cycle.

(a)



(b)



(c)

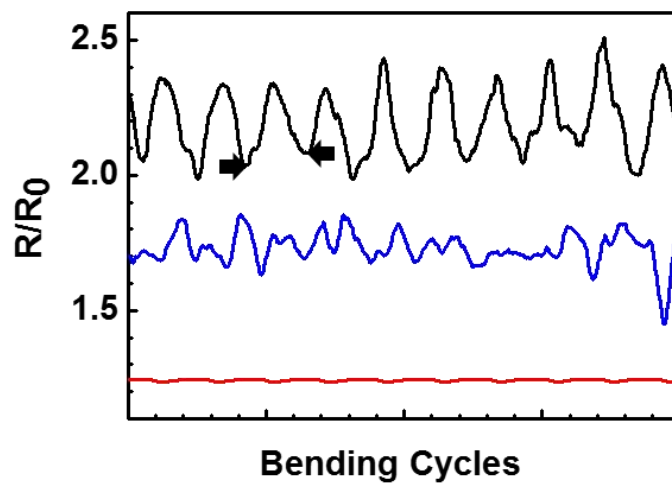


Figure 84. Experimental set-ups for cyclic bending tests and corresponding (b) trend lines of relative changes in a sheet resistance and (c) relative changes of sheet resistance after each individual bending

5.3.4 Performance of welded AgNWs

The mechanical flexibility of conductors is important for maintaining a good performance of electric devices during their lifetime without degradation. In particular, the stability of the resistance of the top electrode of a resistive touch-panel under repeated bending cycles is directly related to device stability, as multidirectional distortion of the top electrode occurs each time when users touch the surface. Thus, a resistive touch-panel was fabricated using the LPEB-welded AgNW percolation networks as a flexible transparent electrode (Figure 85). The operation of this device was confirmed by writing the word “UNIST”. The fabrication of the touch-panels verified that the LPEB welding process can be successfully applied for the fabrication of semiconducting devices. It was confirmed that LPEB welding could modify the mechanical flexibility of devices without any significant compensation in the performance of PLED. Figure 86 shows photographs of green-emissive flexible PLED (operated at 7 V), fabricated using the as-prepared, thermally annealed, and LPEB-welded AgNWs electrodes under bending stress. The flexible PLED with LPEB-welded AgNW electrode exhibited a good device performance. Moreover, Figure 86(c) showed that PLED with LPEB welded AgNWs exhibited outstanding mechanical stability as the same tendency with electrode characteristics.

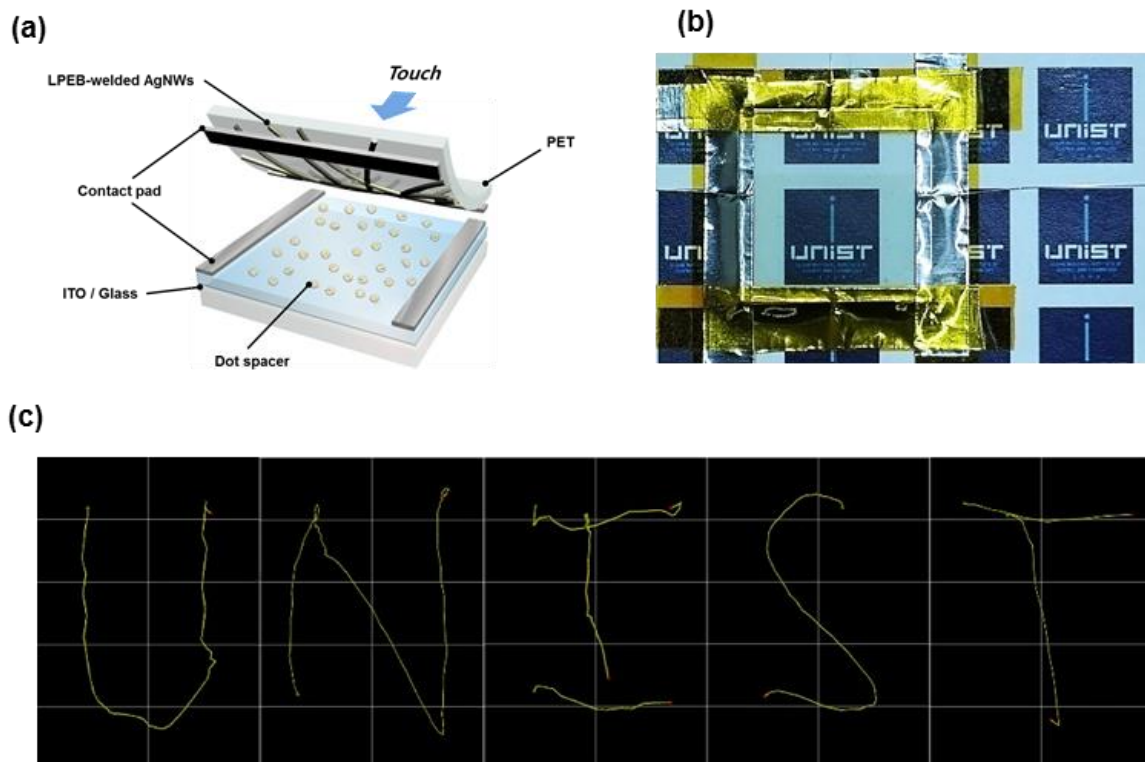


Figure 85. Fabrication of resistive touch-screen panels using LPEB-welded AgNWs and corresponding performance evaluation

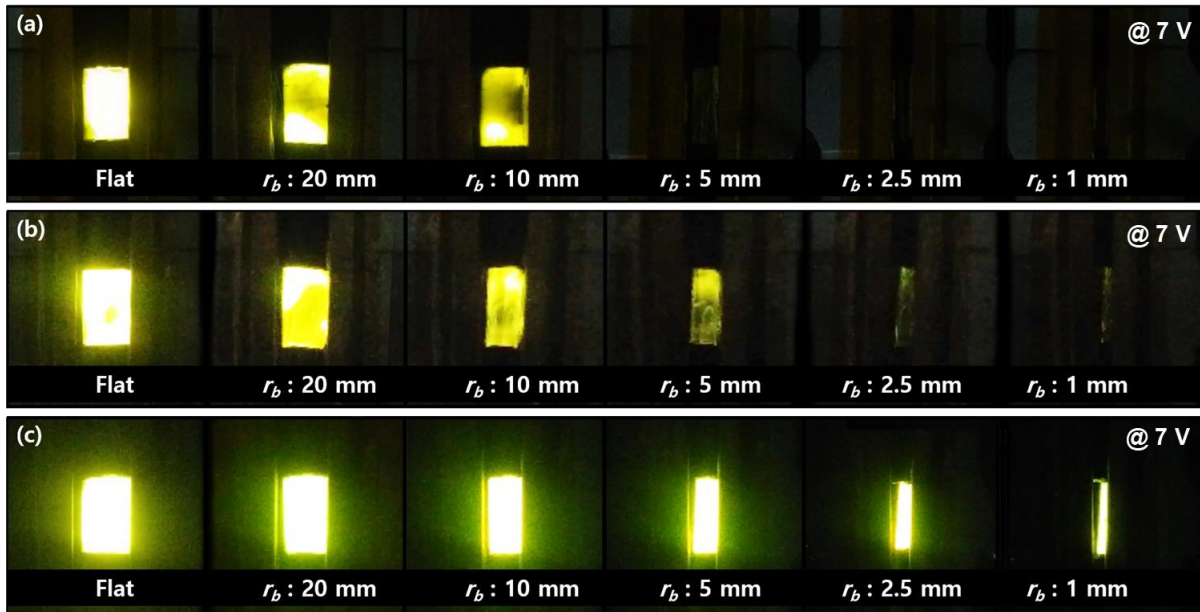


Figure 86. Series of photograph of PLEDs with (a) as-prepared, (b) thermally annealed, and (c) LPEB-welded AgNWs electrodes under bending stress following different bending radius

6. CONCLUSIONS AND RECOMMENDATIONS

6.1 Conclusions

In this study, the LPEB irradiation on engineering materials were investigated from the fundamental understandings of the mechanisms of the LPEB irradiation to the multiscale and hybrid manufacturing applications. A numerical model of temperature fields is proposed to predict the molten depth induced by LPEB irradiation, including energy absorptance, which is dependent on scattering, backscattering, and transmission. The overall consideration of natural interactions between accelerated electrons and substrates to specify the exact absorptance and energy transfer facilitated a better understanding of the multi-physical mechanisms induced during the LPEB irradiation. The numerical model describing depth-dependent absorptance greatly modified the accuracy of temperature and molten depth predictions, within an error range of ~5%, regardless of incident energy and type of materials. Thus, it can be concluded that the proposed model is extensively adaptable for a pulsed electron beam irradiation process to predict the depth of the treated zone before LPEB irradiation.

The LPEB irradiation was adopted for the surface modification of mold steels (KP1 and KP4) and Ti-6Al-7Nb, biomedical alloys. The LPEB irradiation not only produce a high surface quality with reduced surface roughness, also modified the mechanical and chemical properties of the surface including surface hardness, wear resistance, and corrosion resistance. Although the degree of improvement in surface properties varied depending on the type of materials, basically, the LPEB irradiation induced the formation of a metastable re-solidified layer with increased density of dislocations and elimination of pre-dominant slip planes, leading to the surface hardening. Furthermore, a passive and stable re-solidified layer formed by the rapid melting and re-solidification during the LPEB irradiation has resulted in the modification of corrosion resistance on the surface with a nobler corrosion potential, lower corrosion current density, and higher charge transfer resistance. The optimized LPEB conditions for different metallic alloys were extracted from the experimental results; acceleration voltage of 30 keV, solenoid voltage of 1.5 keV, and 10 irradiation cycles.

Especially for Ti-6Al-7Nb alloys, a formation of TiN was observed following the LPEB irradiation. To enhance the performance of surface modification, nitriding process using the LPEB irradiation was designed with the nitrogen plasma gas and a negative DC bias. The atomic concentration of nitrogen at the re-solidified layer could be achieved near the theoretical maximum, ~ 18%. The nano-hardness was improved by about 75% and the charge transfer resistance increased over 180 times following the LPEB nitriding process. The fundamental applications of the LPEB irradiations were investigated and the mechanisms of surface modifications were specified following the changes in microstructure, crystalline structure, and chemical composition after the LPEB irradiations. Most importantly, experimental approaches of the LPEB irradiation revealed three major effects; melting mechanisms,

surface modifications, and energy transfer through electrons. Based on these effects, the LPEB irradiation can further enlarge its application area in manufacturing processes.

The deburring processes for micropatterns were designed and performed on metals and composites. The LPEB deburring successfully reduced the size of the burrs that remained after the laser fabrication and drilling on metals and composites, respectively. Based on the melting mechanisms induced by the LPEB irradiation, micro-sized burrs were selectively eliminated from the products. Most of cases, the number of pulses was the most important parameter in determining the deburring performance.

For the micro-application based on the surface modification factors, a durable super-hydrophobic surface micropatterns were fabricated using the LPEB irradiation. The contact angle on the LPEB-irradiated micropattern was increased up to 166.7° with non-wetting characteristic. The reduction of surface roughness following the LPEB irradiation effectively reduced the critical angle for Wenzel-to-Cassie transition. The hydrophobicity on the LPEB-irradiated patterns was maintained during long-term contact with droplets.

Finally, the silver nanowire (AgNW) welding process was proposed based on the unique energy transfer mechanisms of the LPEB irradiation to fabricate a flexible and transparent electrode. Due to a uniform energy transfer through accelerated electrons, the flexible and transparent AgNW electrodes showed a lower sheet resistance ($12.63 \Omega/\text{sq}$), higher transmittance, and an excellent mechanical flexibility comparing to other AgNW percolation networks prepared by conventional thermal annealing. The fabrication of PLEDs using AgNW by LPEB irradiation proved that the AgNW electrode obtained by LPEB irradiation could serve as an alternative to ITO electrodes in the field of flexible semi-conducting devices.

As summarized in Figure 87, this dissertation contributes to widen the application areas of the LPEB irradiation in manufacturing industries. Based on the fundamental mechanisms revealed in the dissertation, the LPEB irradiation can be utilized as a promising method for manufacturing processes, not only for the applications introduced in this dissertation, but also for numerous kinds of manufacturing processes including precision, biomedical, and surface manufacturing.

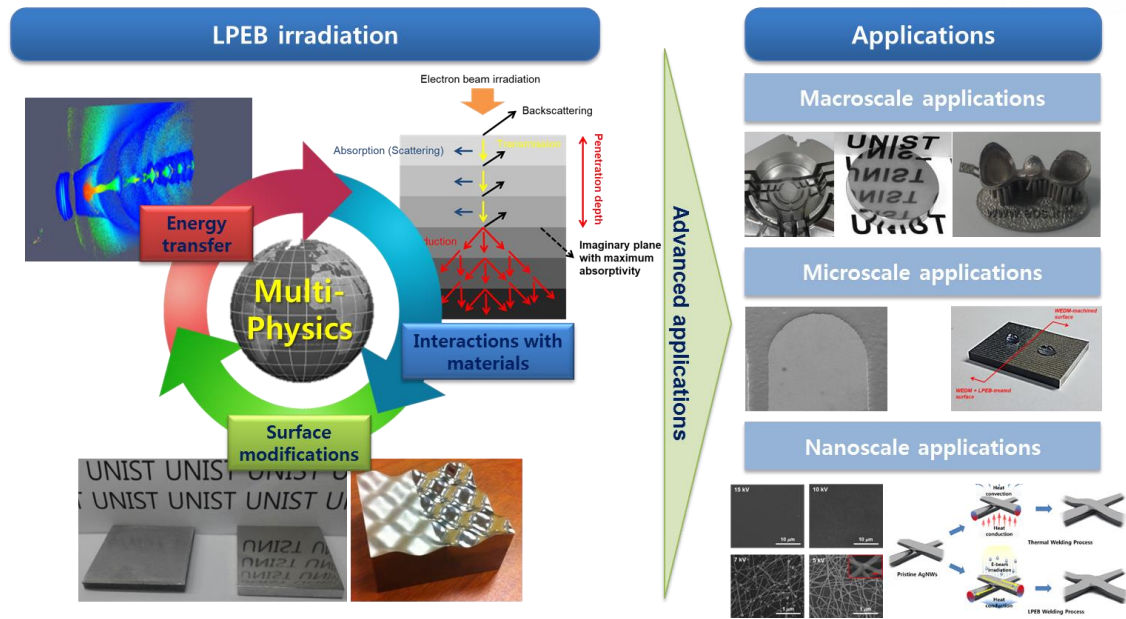


Figure 87. Schematic describing the contributions of the dissertation in manufacturing applications

6.2 Recommendations

In this dissertation, the mechanisms and effects of LPEB irradiations were clearly specified and the possible applications were investigated. In the predictive modeling of LPEB irradiation process, it was possible to analyze the multi-physical phenomena induced during the LPEB irradiation. The following experimental approaches revealed the fundamental effects of the LPEB irradiation on engineering materials. Consequently, it was possible to propose various multiscale and hybrid manufacturing applications using the LPEB irradiation, thanks to the firmly established theoretical descriptions of the process and clearly specified mechanisms of processing. Although those investigations were highly limited to the LPEB in this dissertation, the methodology of this research can be extended to other types of energy beam-based manufacturing process such as ion beam and laser.

Furthermore, there is still a problem that needs to be solved to further applications in surface manufacturing. It is obvious that craters can be generated on the surface by the inclusions present in the material. Although optimization of LPEB parameters, such as increasing number of cycles, can effectively reduce the generation of craters, it cannot be perfectly removed by only controlling the experimental conditions. In Chapter 4.1.2, the mechanisms of the crater generation have been evidently specified. The partial evaporation of non-metallic inclusions can lead the formation of craters following the LPEB irradiation. It is also clear that the resulting craters can have an adverse effect on the products as described in Figure 24. The generation of craters is caused by the inherent characteristics of the material, and no clear solution has been presented to date. The hybrid manufacturing process can be a good approach for solving this critical limitation.

Preliminary results

A hybrid surface modification process using a high power diode laser (HPDL) and LPEB was proposed to modify surface mechanical and chemical properties without generation of craters. A square-shaped hat-top laser was irradiated before the LPEB irradiation to remove the non-metallic inclusions. The hybrid surface treatment was applied on stainless steels that were commonly used in many industrial applications and seriously suffered from pitting corrosion.

A fiber-coupled HPDL (Direct photonics, Germany) having a square beam shape and hat-top energy profile was used for the laser irradiation. The size of beam was set as 200 μm . The power of laser beam was fixed at 100 W. The feed rate was varied from 150 to 600 mm/min.

The LPEB irradiation was applied on the laser-treated surfaces. An accelerating voltage of 30 kV with an energy density of 10 J/cm² was used. The beam pulse was irradiated over a 3 x 3 grid size moving 20 mm apart for each pulse, which matches well with the effective diameter of the beam (60 mm) so that uniform energy can be transferred on the whole surface area. Thus, one cycle of LPEB irradiation consisted of 9 pulses. In total, 9 cycles of LPEB irradiations were performed on each sample, following the laser irradiation.

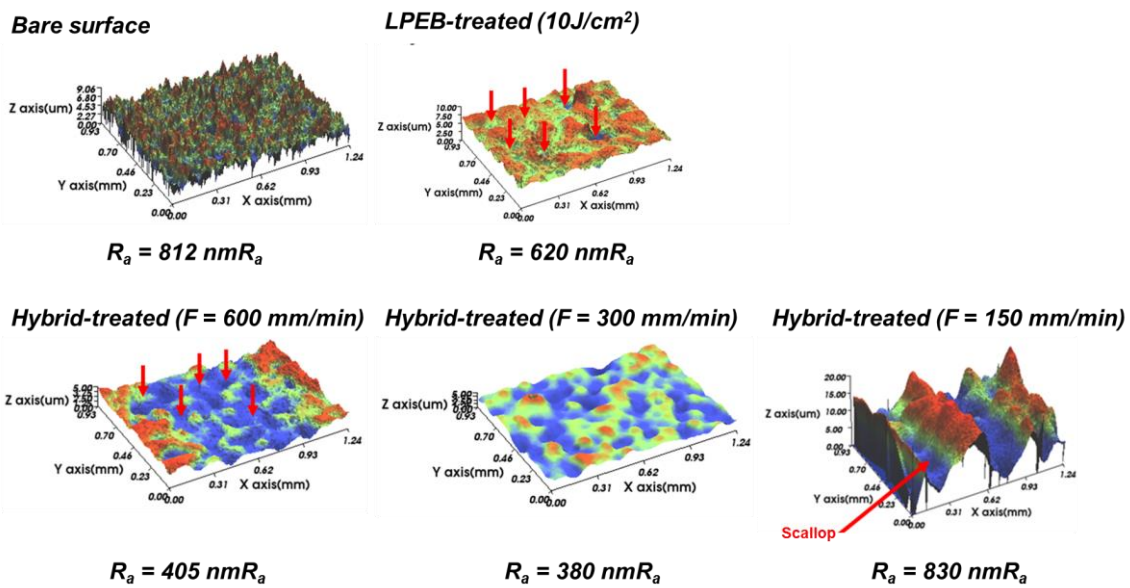


Figure 88. White-interference micrographs and corresponding surface roughness before and after the hybrid surface treatment using HPDL and LPEB

Figure 88 shows the white-interference micrographs and the corresponding variations of surface roughness before and after the hybrid surface treatment. The surface roughness was slightly reduced following the LPEB irradiation in spite of the generation of craters. However, the density and size of craters generated during LPEB irradiation were reduced if laser irradiation is preceded before the LPEB

irradiation. A decrease in feed rate of the laser irradiation before the LPEB irradiation has led to a continuous reduction in the density and size of craters. For a laser feed rate of 300 mm/min, the surface roughness was reduced about 53.2 % following the hybrid surface treatment. Furthermore, only submicro-sized craters were found to remain after the LPEB irradiation. Hence, it can be concluded that employing laser irradiation before the LPEB irradiation could effectively eliminate the non-metallic inclusions, preventing the generation of craters. For a laser feed rate of 150 mm/min, however, the surface roughness was increased due to the formation of scallops induced by overlapped molten regions.

As described in ***Preliminary results*** above, the hybrid surface manufacturing process between two different energy beams can be highly effective to complement limitations of each beam. Although more investigations are needed in depth, the manufacturing processes using LPEB irradiation can be further improved by approaching with the methodology presented here.

References

- [1] C. Herrmann, C. Schmidt, D. Kurle, S. Blume, and S. Thiede, "Sustainability in Manufacturing and Factories of the Future," *International Journal of precision engineering and manufacturing-green technology*, vol. 1, no. 4, pp. 283-292, 2014.
- [2] C. Schmidt, W. Li, S. Thiede, S. Kara, and C. Herrmann, "A methodology for customized prediction of energy consumption in manufacturing industries," *International Journal of Precision Engineering and Manufacturing-Green Technology*, vol. 2, no. 2, pp. 163-172, 2015.
- [3] T.-M. Lo and J.-S. Young, "Improvements of productivity for PCB drilling by laser driller machine," *International journal of precision engineering and manufacturing*, vol. 15, no. 8, pp. 1575-1581, 2014.
- [4] D.-J. Yoo, "New paradigms in cellular material design and fabrication," *International Journal of Precision Engineering and Manufacturing*, vol. 16, no. 12, pp. 2577-2589, 2015.
- [5] J. Heo, H. Min, and M. Lee, "Laser micromachining of permalloy for fine metal mask," *International Journal of Precision Engineering and Manufacturing-Green Technology*, vol. 2, no. 3, pp. 225-230, 2015.
- [6] C. Park, B.-S. Shin, M.-S. Kang, Y.-W. Ma, J.-Y. Oh, and S.-M. Hong, "Experimental study on micro-porous patterning using UV pulse laser hybrid process with chemical foaming agent," *International Journal of Precision Engineering and Manufacturing*, vol. 16, no. 7, pp. 1385-1390, 2015.
- [7] S. Prakash and S. Kumar, "Fabrication of microchannels on transparent PMMA using CO 2 Laser (10.6 μm) for microfluidic applications: An experimental investigation," *International Journal of Precision Engineering and Manufacturing*, vol. 16, no. 2, pp. 361-366, 2015.
- [8] C.-V. Ngo, G. Davaasuren, H.-S. Oh, and D.-M. Chun, "Transparency and superhydrophobicity of cone-shaped micropillar array textured polydimethylsiloxane," *International Journal of Precision Engineering and Manufacturing*, vol. 16, no. 7, pp. 1347-1353, 2015.
- [9] J. Kim, T.-J. Je, S.-H. Cho, E.-C. Jeon, and K.-H. Whang, "Micro-cutting with diamond tool micro-patterned by femtosecond laser," *International journal of precision engineering and manufacturing*, vol. 15, no. 6, pp. 1081-1085, 2014.
- [10] N.-H. Cha and C.-M. Lee, "A study on machining characteristics of silicon nitride with spline members in laser-assisted turn-mill," *International Journal of Precision Engineering and Manufacturing*, vol. 16, no. 13, pp. 2691-2697, 2015.
- [11] B. Guo, Q. Zhao, and X. Yu, "Surface micro-structuring of coarse-grained diamond wheels by nanosecond pulsed laser for improving grinding performance," *International journal of precision engineering and manufacturing*, vol. 15, no. 10, pp. 2025-2030, 2014.
- [12] C.-J. Lee, J.-D. Kim, and Y.-C. Kim, "Study on monitoring of plasma emission signal in lap

- welding of Zn coated steel sheet using CO₂ laser," *International Journal of Precision Engineering and Manufacturing*, vol. 16, no. 3, pp. 495-500, 2015.
- [13] S.-J. Lee, M. Takahashi, Y. Kawahito, and S. Katayama, "Microstructural evolution and characteristics of weld fusion zone in high speed dissimilar welding of Ti and Al," *International Journal of Precision Engineering and Manufacturing*, vol. 16, no. 10, pp. 2121-2127, 2015.
- [14] D.-H. Park and H.-H. Kwon, "Development of warm forming parts for automotive body dash panel using AZ31B magnesium alloy sheets," *International Journal of Precision Engineering and Manufacturing*, vol. 16, no. 10, pp. 2159-2165, 2015.
- [15] W. Choi and J. Kim, "Fractal dimensional analysis on glass fracture," *International Journal of Precision Engineering and Manufacturing*, vol. 16, no. 7, pp. 1655-1660, 2015.
- [16] J. H. Yu, Y. Rho, H. Kang, H. S. Jung, and K.-T. Kang, "Electrical behavior of laser-sintered Cu based metal-organic decomposition ink in air environment and application as current collectors in supercapacitor," *International Journal of Precision Engineering and Manufacturing-Green Technology*, vol. 2, no. 4, pp. 333-337, 2015.
- [17] S. Khademzadeh, N. Parvin, and P. F. Bariani, "Production of NiTi alloy by direct metal deposition of mechanically alloyed powder mixtures," *International Journal of Precision Engineering and Manufacturing*, vol. 16, no. 11, pp. 2333-2338, 2015.
- [18] N. Gupta, S. B. Ahirrao, S. Paul, and R. K. Singh, "Modeling of micro-scale fiber laser hardening process and optimization via statistical approximation of the engineering models," *International Journal of Precision Engineering and Manufacturing*, vol. 16, no. 11, pp. 2281-2287, 2015.
- [19] K.-W. Jung, Y. Kawahito, and S. Katayama, "Mechanical property and joining characteristics of laser direct joining of CFRP to polyethylene terephthalate," *International Journal of Precision Engineering and Manufacturing-Green Technology*, vol. 1, no. 1, pp. 43-48, 2014.
- [20] C.-C. Ho and J.-J. He, "On-line monitoring of laser-drilling process based on coaxial machine vision," *International journal of precision engineering and manufacturing*, vol. 15, no. 4, pp. 671-678, 2014.
- [21] J. Dureja, R. Singh, T. Singh, P. Singh, M. Dogra, and M. S. Bhatti, "Performance evaluation of coated carbide tool in machining of stainless steel (AISI 202) under minimum quantity lubrication (MQL)," *International Journal of Precision Engineering and Manufacturing-Green Technology*, vol. 2, no. 2, pp. 123-129, 2015.
- [22] D. Bae *et al.*, "Evaluation on hydrogen embrittlement of material using nondestructive test," *International journal of precision engineering and manufacturing*, vol. 15, no. 6, pp. 989-993, 2014.
- [23] C. Park, H. Kim, S. Lee, and H. Jeong, "The influence of abrasive size on high-pressure chemical mechanical polishing of sapphire wafer," *International Journal of Precision*

- Engineering and Manufacturing-Green Technology*, vol. 2, no. 2, pp. 157-162, 2015.
- [24] T. Hassel, N. Murray, R. Konya, A. Beniyash, and F.-W. Bach, "Nonvacuum electron beam cutting and welding—two partnering processes for fast and highly efficient metal working," *Welding in the World*, vol. 57, no. 3, pp. 315-322, 2013.
- [25] J. Ghatak, J.-H. Huang, and C.-P. Liu, "Derivation of the surface free energy of ZnO and GaN using in situ electron beam hole drilling," *Nanoscale*, vol. 8, no. 1, pp. 634-640, 2016.
- [26] M. S. Węglowski, S. Błacha, and A. Phillips, "Electron beam welding—Techniques and trends—Review," *Vacuum*, vol. 130, pp. 72-92, 2016.
- [27] V. R. Manfrinato *et al.*, "Resolution limits of electron-beam lithography toward the atomic scale," *Nano letters*, vol. 13, no. 4, pp. 1555-1558, 2013.
- [28] C. Körner, "Additive manufacturing of metallic components by selective electron beam melting—a review," *International Materials Reviews*, vol. 61, no. 5, pp. 361-377, 2016.
- [29] Y. Uno, A. Okada, K. Uemura, P. Raharjo, T. Furukawa, and K. Karato, "High-efficiency finishing process for metal mold by large-area electron beam irradiation," *Precision Engineering*, vol. 29, no. 4, pp. 449-455, 2005.
- [30] C. Zhou, L. Shan, J. R. Hight, S. Danyluk, S. Ng, and A. J. Paszkowski, "Influence of colloidal abrasive size on material removal rate and surface finish in SiO₂ chemical mechanical polishing," *Tribology Transactions*, vol. 45, no. 2, pp. 232-238, 2002.
- [31] P. Kao and H. Hocheng, "Optimization of electrochemical polishing of stainless steel by grey relational analysis," *Journal of Materials Processing Technology*, vol. 140, no. 1-3, pp. 255-259, 2003.
- [32] K. G. Budinski and M. K. Budinski, "Engineering materials," *Nature*, vol. 25, p. 28, 2009.
- [33] E. Atık, U. Yunker, and C. Meriç, "The effects of conventional heat treatment and boronizing on abrasive wear and corrosion of SAE 1010, SAE 1040, D2 and 304 steels," *Tribology International*, vol. 36, no. 3, pp. 155-161, 2003.
- [34] N. Zhong, X. Wang, L. Wang, and Y. Rong, "Enhancement of the mechanical properties of a Nb-microalloyed advanced high-strength steel treated by quenching–partitioning–tempering process," *Materials Science and Engineering: A*, vol. 506, no. 1-2, pp. 111-116, 2009.
- [35] I. Pashby, S. Barnes, and B. Bryden, "Surface hardening of steel using a high power diode laser," *Journal of Materials Processing Technology*, vol. 139, no. 1-3, pp. 585-588, 2003.
- [36] C. S. Montross, T. Wei, L. Ye, G. Clark, and Y.-W. Mai, "Laser shock processing and its effects on microstructure and properties of metal alloys: a review," *International journal of fatigue*, vol. 24, no. 10, pp. 1021-1036, 2002.
- [37] M. Bouklah, B. Hammouti, M. Lagrenee, and F. Bentiss, "Thermodynamic properties of 2, 5-bis (4-methoxyphenyl)-1, 3, 4-oxadiazole as a corrosion inhibitor for mild steel in normal sulfuric acid medium," *Corrosion science*, vol. 48, no. 9, pp. 2831-2842, 2006.

- [38] M. Lebrini, M. Lagrenée, H. Vezin, M. Traisnel, and F. Bentiss, "Experimental and theoretical study for corrosion inhibition of mild steel in normal hydrochloric acid solution by some new macrocyclic polyether compounds," *Corrosion Science*, vol. 49, no. 5, pp. 2254-2269, 2007.
- [39] M. Morad, "Inhibition of iron corrosion in acid solutions by Cefatrexyl: Behaviour near and at the corrosion potential," *Corrosion Science*, vol. 50, no. 2, pp. 436-448, 2008.
- [40] L. Herrag *et al.*, "Adsorption properties and inhibition of mild steel corrosion in hydrochloric solution by some newly synthesized diamine derivatives: experimental and theoretical investigations," *Corrosion Science*, vol. 52, no. 9, pp. 3042-3051, 2010.
- [41] N. Khalil, "Quantum chemical approach of corrosion inhibition," *Electrochimica Acta*, vol. 48, no. 18, pp. 2635-2640, 2003.
- [42] T. Chen, H. John, J. Xu, Q. Lu, J. Hawk, and X. Liu, "Influence of surface modifications on pitting corrosion behavior of nickel-base alloy 718. Part 1: Effect of machine hammer peening," *Corrosion Science*, vol. 77, pp. 230-245, 2013.
- [43] S. Habibzadeh, L. Li, D. Shum-Tim, E. C. Davis, and S. Omanovic, "Electrochemical polishing as a 316L stainless steel surface treatment method: towards the improvement of biocompatibility," *Corrosion Science*, vol. 87, pp. 89-100, 2014.
- [44] L. Song, X. Ma, Z. Chen, and B. Hou, "The role of UV illumination on the initial atmospheric corrosion of 09CuPCrNi weathering steel in the presence of NaCl particles," *Corrosion Science*, vol. 87, pp. 427-437, 2014.
- [45] U. Trdan and J. Grum, "SEM/EDS characterization of laser shock peening effect on localized corrosion of Al alloy in a near natural chloride environment," *Corrosion Science*, vol. 82, pp. 328-338, 2014.
- [46] H. Suzuki, S. Hamada, T. Okino, M. Kondo, Y. Yamagata, and T. Higuchi, "Ultraprecision finishing of micro-aspheric surface by ultrasonic two-axis vibration assisted polishing," *CIRP annals*, vol. 59, no. 1, pp. 347-350, 2010.
- [47] V. Jain and S. Adsul, "Experimental investigations into abrasive flow machining (AFM)," *International Journal of Machine Tools and Manufacture*, vol. 40, no. 7, pp. 1003-1021, 2000.
- [48] P. Peyre *et al.*, "Surface modifications induced in 316L steel by laser peening and shot-peening. Influence on pitting corrosion resistance," *Materials Science and Engineering: A*, vol. 280, no. 2, pp. 294-302, 2000.
- [49] N. Hosking, M. Ström, P. Shipway, and C. Rudd, "Corrosion resistance of zinc-magnesium coated steel," *Corrosion science*, vol. 49, no. 9, pp. 3669-3695, 2007.
- [50] J. Kim and H. W. Park, "Influence of a large pulsed electron beam (LPEB) on the corrosion resistance of Ti-6Al-7Nb alloys," *Corrosion Science*, vol. 90, pp. 153-160, 2015.
- [51] Y. Uno *et al.*, "A new polishing method of metal mold with large-area electron beam irradiation," *Journal of Materials processing technology*, vol. 187, pp. 77-80, 2007.

- [52] A. Okada *et al.*, "Surface finishing of stainless steels for orthopedic surgical tools by large-area electron beam irradiation," *CIRP Annals-Manufacturing Technology*, vol. 57, no. 1, pp. 223-226, 2008.
- [53] K. Zhang, J. Zou, T. Grosdidier, and C. Dong, "Formation and evolution of craters in carbon steels during low-energy high-current pulsed electron-beam treatment," *Journal of Vacuum Science & Technology A*, vol. 27, no. 5, pp. 1217-1226, 2009.
- [54] J. Zou, Y. Qin, C. Dong, X. Wang, A. Wu, and S. Hao, "Numerical simulation of the thermal-mechanical process of high current pulsed electron beam treatment," *Journal of Vacuum Science & Technology A: Vacuum, Surfaces, and Films*, vol. 22, no. 3, pp. 545-552, 2004.
- [55] A. Modinos, *Field, thermionic and secondary electron emission spectroscopy*. Springer Science & Business Media, 2013.
- [56] H. L. Skriver and N. Rosengaard, "Surface energy and work function of elemental metals," *Physical Review B*, vol. 46, no. 11, pp. 7157, 1992.
- [57] S. I. Molokovsky and A. D. Sushkov, *Intense electron and ion beams*. Springer Science & Business Media, 2005.
- [58] K. Abderrazak, S. Bannour, H. Mhiri, G. Lepalec, and M. Autric, "Numerical and experimental study of molten pool formation during continuous laser welding of AZ91 magnesium alloy," *Computational Materials Science*, vol. 44, no. 3, pp. 858-866, 2009.
- [59] A. Mackwood and R. Crafer, "Thermal modelling of laser welding and related processes: a literature review," *Optics & Laser Technology*, vol. 37, no. 2, pp. 99-115, 2005.
- [60] T. Eagar and N. Tsai, "Temperature fields produced by traveling distributed heat sources," *Welding journal*, vol. 62, no. 12, pp. 346-355, 1983.
- [61] J. Goldak, A. Chakravarti, and M. Bibby, "A new finite element model for welding heat sources," *Metallurgical transactions B*, vol. 15, no. 2, pp. 299-305, 1984.
- [62] V. Pavelic, R. Tanbakuchi, O. Uyehara, and P. Myers, "Experimental and computed temperature histories in gas tungsten-arc welding of thin plates," *WELD J*, vol. 48, no. 7, p. 295, 1969.
- [63] D. Rosenthal, "The Theory of Moving Sources of Heat and Its Application of Metal Treatments," *Transactions of ASME*, vol. 68, pp. 849-866, 1946.
- [64] N. Nguyen, A. Ohta, K. Matsuoka, N. Suzuki, and Y. Maeda, "Analytical solutions for transient temperature of semi-infinite body subjected to 3-D moving heat sources," *WELDING JOURNAL-NEW YORK-*, vol. 78, pp. 265-s, 1999.
- [65] Y. T. Cho and S. J. Na, "Numerical analysis of plasma in CO₂ laser and arc hybrid welding," *International Journal of Precision engineering and manufacturing*, vol. 16, no. 4, pp. 787-795, 2015.
- [66] V. Cosslett and R. Thomas, "Multiple scattering of 5-30 keV electrons in evaporated metal films: I. Total transmission and angular distribution," *British Journal of Applied Physics*, vol. 15, no.

- 8, pp. 883, 1964.
- [67] V. Cosslett and R. Thomas, "Multiple scattering of 5-30 keV electrons in evaporated metal films II: Range-energy relations," *British Journal of Applied Physics*, vol. 15, no. 11, pp. 1283, 1964.
- [68] V. Cosslett and R. Thomas, "Multiple scattering of 5-30 keV electrons in evaporated metal films III: Backscattering and absorption," *British Journal of Applied Physics*, vol. 16, no. 6, pp. 779, 1965.
- [69] P.-F. Staub, "Bulk target backscattering coefficient and energy distribution of 0.5-100 keV electrons: an empirical and synthetic study," *Journal of Physics D: Applied Physics*, vol. 27, no. 7, pp. 1533, 1994.
- [70] G. Neubert and S. Rogaschewski, "Backscattering coefficient measurements of 15 to 60 keV electrons for solids at various angles of incidence," *physica status solidi (a)*, vol. 59, no. 1, pp. 35-41, 1980.
- [71] J. Kim, W. J. Lee, H. W. Park, "Temperature Predictive model of the large pulsed electron beam (LPEB) irradiation on engineering alloys," *Applied Thermal Engineering*, vol. 128, pp. 151-158, 2018.
- [72] H. Niedrig, "Electron backscattering from thin films," *Journal of Applied Physics*, vol. 53, no. 4, pp. R15-R49, 1982.
- [73] L. Reimer, "Emission of backscattered and secondary electrons," in *Scanning Electron Microscopy*: Springer, 1998, pp. 135-169.
- [74] K. Kanaya and S. Ono, "The energy dependence of a diffusion model of an electron probe into solid targets," *Journal of Physics D: Applied Physics*, vol. 11, no. 11, pp. 1495, 1978.
- [75] A. Klassen, A. Bauereiß, and C. Körner, "Modelling of electron beam absorption in complex geometries," *Journal of Physics D: Applied Physics*, vol. 47, no. 6, pp. 065307, 2014.
- [76] R. Daneshkhah, M. Najafi, and H. Torabian, "Numerical simulation of weld pool shape during laser beam welding," *Int. J. Appl. Basic Sci*, vol. 3, no. 8, pp. 1624-1630, 2012.
- [77] H. S. Carslaw and J. C. Jaeger, "Conduction of heat in solids," *Oxford: Clarendon Press, 1959, 2nd ed.*, 1959.
- [78] J. Kim, S. S. Park, H. W. Park, "Corrosion inhibition and surface hardening of KP1 and KP4 mold steels using pulsed electron beam treatment," *Corrosion Science*, vol. 89, pp. 179-188, 2014.
- [79] C. Vasilescu, S. Drob, E. Neacsu, and J. M. Rosca, "Surface analysis and corrosion resistance of a new titanium base alloy in simulated body fluids," *Corrosion Science*, vol. 65, pp. 431-440, 2012.
- [80] C.-c. Li *et al.*, "Adsorption and corrosion inhibition of phytic acid calcium on the copper surface in 3 wt% NaCl solution," *Corrosion Science*, vol. 83, pp. 147-154, 2014.
- [81] T. Zhao and G. Mu, "The adsorption and corrosion inhibition of anion surfactants on aluminium

- surface in hydrochloric acid," *Corrosion Science*, vol. 41, no. 10, pp. 1937-1944, 1999.
- [82] M. Sheffer, A. Groysman, and D. Mandler, "Electrodeposition of sol-gel films on Al for corrosion protection," *Corrosion Science*, vol. 45, no. 12, pp. 2893-2904, 2003.
- [83] T. Hryniewicz, R. Rokicki, and K. Rokosz, "Corrosion characteristics of medical-grade AISI type 316L stainless steel surface after electropolishing in a magnetic field," *Corrosion*, vol. 64, no. 8, pp. 660-665, 2008.
- [84] K. Hashimoto, K. Asami, A. Kawashima, H. Habazaki, and E. Akiyama, "The role of corrosion-resistant alloying elements in passivity," *Corrosion Science*, vol. 49, no. 1, pp. 42-52, 2007.
- [85] B. Stellwag, "The mechanism of oxide film formation on austenitic stainless steels in high temperature water," *Corrosion science*, vol. 40, no. 2-3, pp. 337-370, 1998.
- [86] P. Gostin, A. Gebert, and L. Schultz, "Comparison of the corrosion of bulk amorphous steel with conventional steel," *Corrosion Science*, vol. 52, no. 1, pp. 273-281, 2010.
- [87] M. Escudero *et al.*, "Possibilities for improving the corrosion resistance of Fe-40Al intermetallic strip by prior oxide protection," *Scripta materialia*, vol. 48, no. 11, pp. 1549-1554, 2003.
- [88] R. Chen and W. Yeun, "Review of the high-temperature oxidation of iron and carbon steels in air or oxygen," *Oxidation of metals*, vol. 59, no. 5-6, pp. 433-468, 2003.
- [89] R. Avci, B. Davis, M. Wolfenden, I. Beech, K. Lucas, and D. Paul, "Mechanism of MnS-mediated pit initiation and propagation in carbon steel in an anaerobic sulfidogenic media," *Corrosion Science*, vol. 76, pp. 267-274, 2013.
- [90] Y. Tsutsumi, A. Nishikata, and T. Tsuru, "Pitting corrosion mechanism of Type 304 stainless steel under a droplet of chloride solutions," *Corrosion science*, vol. 49, no. 3, pp. 1394-1407, 2007.
- [91] C. Paik, H. White, and R. Alkire, "Scanning electrochemical microscopy detection of dissolved sulfur species from inclusions in stainless steel," *Journal of the electrochemical society*, vol. 147, no. 11, pp. 4120-4124, 2000.
- [92] J. Zou, K. Zhang, S. Hao, C. Dong, and T. Grosdidier, "Mechanisms of hardening, wear and corrosion improvement of 316L stainless steel by low energy high current pulsed electron beam surface treatment," *Thin Solid Films*, vol. 519, no. 4, pp. 1404-1415, 2010.
- [93] K. Zhang, J. Zou, B. Bolle, and T. Grosdidier, "Evolution of residual stress states in surface layers of an AISI D2 steel treated by low energy high current pulsed electron beam," *Vacuum*, vol. 87, pp. 60-68, 2013.
- [94] A. Pogrebnjak *et al.*, "A comparison of radiation damage and mechanical and tribological properties of α -Fe exposed to intense pulsed electron and ion beams," *Vacuum*, vol. 58, no. 1, pp. 45-52, 2000.
- [95] O. A. Olaseinde, J. Merwe, and L. Cornish, "Characterization and corrosion behaviour of

- selected duplex stainless steels in acidic and acidic-chloride solution," *Advances in Chemical Engineering and Science*, vol. 4, no. 1, pp. 89-93, 2014.
- [96] C.-H. Hsu and M.-L. Chen, "Corrosion behavior of nickel alloyed and austempered ductile irons in 3.5% sodium chloride," *Corrosion Science*, vol. 52, no. 9, pp. 2945-2949, 2010.
- [97] P. Bilmes, C. Llorente, C. Méndez, and C. Gervasi, "Microstructure, heat treatment and pitting corrosion of 13CrNiMo plate and weld metals," *Corrosion Science*, vol. 51, no. 4, pp. 876-881, 2009.
- [98] S. Rogers, D. Howie, S. Graves, M. Percy, and D. Haynes, "In vitro human monocyte response to wear particles of titanium alloy containing vanadium or niobium," *J Bone Joint Surg Br*, vol. 79, no. 2, pp. 311-315, 1997.
- [99] M. Palanuwech, "The fatigue resistance of commercially pure titanium (grade II), titanium alloy (Ti6Al7Nb) and conventional cobalt chromium cast clasps," 2003.
- [100] F. Mansfeld, "Tafel slopes and corrosion rates obtained in the pre-Tafel region of polarization curves," *Corrosion science*, vol. 47, no. 12, pp. 3178-3186, 2005.
- [101] X. Zhang, S. Hao, X. Li, C. Dong, and T. Grosdidier, "Surface modification of pure titanium by pulsed electron beam," *Applied Surface Science*, vol. 257, no. 13, pp. 5899-5902, 2011.
- [102] J. Petit, G. Chatainier, and F. Dabosi, "Inhibitors for the corrosion of reactive metals: Titanium and zirconium and their alloys in acid media," *Corrosion Science*, vol. 21, no. 4, pp. 279-299, 1981.
- [103] A. Kocijan, D. K. Merl, and M. Jenko, "The corrosion behaviour of austenitic and duplex stainless steels in artificial saliva with the addition of fluoride," *Corrosion Science*, vol. 53, no. 2, pp. 776-783, 2011.
- [104] V. Oliveira, C. Aguiar, A. Vazquez, A. Robin, and M. Barboza, "Improving corrosion resistance of Ti-6Al-4V alloy through plasma-assisted PVD deposited nitride coatings," *Corrosion Science*, vol. 88, pp. 317-327, 2014.
- [105] J. Chesnutt, C. Rhodes, and J. Williams, "Relationship between mechanical properties, microstructure, and fracture topography in $\alpha + \beta$ titanium alloys," in *Fractography—Microscopic Cracking Processes*: ASTM International, 1976.
- [106] K. i. Yokoyama, T. Ogawa, K. Asaoka, and J. i. Sakai, "Susceptibility to delayed fracture of alpha-beta titanium alloy in fluoride solutions," *Corrosion science*, vol. 47, no. 7, pp. 1778-1793, 2005.
- [107] G.-L. Song, "The Grand Challenges in Electrochemical Corrosion Research," (in English), *Frontiers in Materials*, Specialty Grand Challenge vol. 1, 2014-March-10 2014.
- [108] C.-D. Gu, J.-L. Zhang, W.-Q. Bai, Y.-Y. Tong, X.-L. Wang, and J.-P. Tu, "Electro-brush plating from deep eutectic solvent: a case of nanocrystalline Ni coatings with superior mechanical property and corrosion resistance," *Journal of The Electrochemical Society*, vol. 162, no. 4, pp.

- D159-D165, 2015.
- [109] E. Zalnezhad, A. A. Sarhan, and M. Hamdi, "Investigating the fretting fatigue life of thin film titanium nitride coated aerospace Al7075-T6 alloy," *Materials Science and Engineering: A*, vol. 559, pp. 436-446, 2013.
- [110] J. Kim, W. J. Lee, H. W. Park, "Mechanical properties and corrosion behavior of the nitriding surface layer of Ti-6Al-7Nb using large pulsed electron beam (LPEB)," *Journal of Alloys and Compounds*, vol. 679, pp. 138-148, 2016.
- [111] L. Thair, U. K. Mudali, S. Rajagopalan, R. Asokamani, and B. Raj, "Surface characterization of passive film formed on nitrogen ion implanted Ti-6Al-4V and Ti-6Al-7Nb alloys using SIMS," *Corrosion science*, vol. 45, no. 9, pp. 1951-1967, 2003.
- [112] E.-S. M. Sherif, H. S. Abdo, K. A. Khalil, and A. M. Nabawy, "Corrosion properties in sodium chloride solutions of Al-TiC composites in situ synthesized by HFIHF," *Metals*, vol. 5, no. 4, pp. 1799-1811, 2015.
- [113] S. M. Yi, S. H. Jin, J. D. Lee, and C. N. Chu, "Fabrication of a high-aspect-ratio stainless steel shadow mask and its application to pentacene thin-film transistors," *Journal of Micromechanics and microengineering*, vol. 15, no. 2, p. 263, 2005.
- [114] B. Niu, J. Chen, and F. Liu, "Optimization on the fiber laser micro-cutting of thin stainless steel sheet by artificial neural networks," *Advanced Science Letters*, vol. 4, no. 3, pp. 810-813, 2011.
- [115] C. Hayden and C. Dalton, "Direct patterning of microelectrode arrays using femtosecond laser micromachining," *Applied Surface Science*, vol. 256, no. 12, pp. 3761-3766, 2010.
- [116] H. S. Shin, M. S. Park, and C. N. Chu, "Analysis of machining characteristics in electrochemical etching using laser masking," *Applied surface science*, vol. 258, no. 5, pp. 1689-1698, 2011.
- [117] T. Purtonen and A. Salminen, "A study on the effect of cutting position on performance of fiber laser cutting of stainless steel tubes," *Welding in the World*, vol. 58, no. 2, pp. 193-204, 2014.
- [118] J. Zhao *et al.*, "Morphology and crystalline phase characteristics of α -GST films irradiated by a picosecond laser," *Applied Surface Science*, vol. 289, pp. 160-166, 2014.
- [119] S. A. Niknam, Y. Zedan, and V. Songmene, "Machining Burrs Formation & Deburring of Aluminium Alloys," 2014.
- [120] J. Kim, H. W. Park, "Hybrid deburring process assisted by a large pulsed electron beam (LPEB) for laser-fabricated patterned metal masks," *Applied Surface Science*, vol. 357, pp. 1676-1683, 2015.
- [121] N. K. Mk, C. H. Ch, A. Jaharah, and N. A. AKM, "Tool wear and surface roughness on milling carbon fiber-reinforced plastic using chilled air," *Journal of Asian Scientific Research*, vol. 2, no. 11, p. 593, 2012.
- [122] S. T. Kumaran, T. J. Ko, C. Li, Z. Yu, and M. Uthayakumar, "Rotary ultrasonic machining of woven CFRP composite in a cryogenic environment," *Journal of Alloys and Compounds*, vol.

- 698, pp. 984-993, 2017.
- [123] K. X. Qiu, C. D. Wang, Q. L. An, and M. Chen, "Defects Study on Drilling of Carbon Fiber Reinforced Polymer (CFRP) Laminates," in *Materials Science Forum*, 2014, vol. 800, pp. 61-65: Trans Tech Publ.
- [124] A. Riveiro *et al.*, "Experimental study on the CO₂ laser cutting of carbon fiber reinforced plastic composite," *Composites Part A: Applied Science and Manufacturing*, vol. 43, no. 8, pp. 1400-1409, 2012.
- [125] M. M. Islam, C. P. Li, S. J. Won, and T. J. Ko, "A deburring strategy in drilled hole of CFRP composites using EDM process," *Journal of Alloys and Compounds*, vol. 703, pp. 477-485, 2017.
- [126] L. K. Gillespie, *Deburring and edge finishing handbook*. Society of Manufacturing Engineers, 1999.
- [127] W. Ji, Y. W. Wang, Y. Li, F. Yan, and X. Liu, "Study of Exit Burr Formation of CFRP," in *Advanced Materials Research*, 2011, vol. 188, pp. 154-157: Trans Tech Publ.
- [128] J. Maitra and V. K. Shukla, "Cross-linking in hydrogels-a review," *American Journal of Polymer Science*, vol. 4, no. 2, pp. 25-31, 2014.
- [129] S. G. Miller *et al.*, "Increased tensile strength of carbon nanotube yarns and sheets through chemical modification and electron beam irradiation," *ACS applied materials & interfaces*, vol. 6, no. 9, pp. 6120-6126, 2014.
- [130] K. Liu, X. Yao, and L. Jiang, "Recent developments in bio-inspired special wettability," *Chemical Society Reviews*, vol. 39, no. 8, pp. 3240-3255, 2010.
- [131] Y. Liu, X. Yin, J. Zhang, S. Yu, Z. Han, and L. Ren, "A electro-deposition process for fabrication of biomimetic super-hydrophobic surface and its corrosion resistance on magnesium alloy," *Electrochimica Acta*, vol. 125, pp. 395-403, 2014.
- [132] X. Dai, B. B. Stogin, S. Yang, and T.-S. Wong, "Slippery Wenzel State," *ACS nano*, vol. 9, no. 9, pp. 9260-9267, 2015.
- [133] Q. He, C. Ma, X. Hu, and H. Chen, "Method for fabrication of paper-based microfluidic devices by alkylsilane self-assembling and UV/O₃-patterning," *Analytical chemistry*, vol. 85, no. 3, pp. 1327-1331, 2013.
- [134] M. H. Kwon, H. S. Shin, and C. N. Chu, "Fabrication of a super-hydrophobic surface on metal using laser ablation and electrodeposition," *Applied Surface Science*, vol. 288, pp. 222-228, 2014.
- [135] M. H. Kwon, W. Y. Jee, and C. N. Chu, "Fabrication of hydrophobic surfaces using copper electrodeposition and oxidation," *International Journal of Precision Engineering and Manufacturing*, vol. 16, no. 5, pp. 877-882, 2015.
- [136] W.-G. Bae, D. Kim, K. Y. Song, H. E. Jeong, and C. N. Chu, "Engineering stainless steel surface

- via wire electrical discharge machining for controlling the wettability," *Surface and Coatings Technology*, 2015.
- [137] M. Liang, Y. Wei, L. Hou, H. Wang, Y. Li, and C. Guo, "Fabrication of a super-hydrophobic surface on a magnesium alloy by a simple method," *Journal of Alloys and Compounds*, vol. 656, pp. 311-317, 2016.
- [138] T. Matsumura, F. Iida, T. Hirose, and M. Yoshino, "Micro machining for control of wettability with surface topography," *Journal of Materials Processing Technology*, vol. 212, no. 12, pp. 2669-2677, 2012.
- [139] J. Kim, S. O. Sim, H. W. Park, "Fabrication of durable hydrophobic micropatterns on stainless steel using a hybrid irradiation process," *Surface & Coatings Technology*, vol. 302, pp. 535-542, 2016.
- [140] K. Kubiak, M. Wilson, T. Mathia, and P. Carval, "Wettability versus roughness of engineering surfaces," *Wear*, vol. 271, no. 3-4, pp. 523-528, 2011.
- [141] M. Reyssat, J. Yeomans, and D. Quéré, "Impalement of fakir drops," *EPL (Europhysics Letters)*, vol. 81, no. 2, p. 26006, 2008.
- [142] D. Quéré, "Wetting and roughness," *Annu. Rev. Mater. Res.*, vol. 38, pp. 71-99, 2008.
- [143] R. N. Wenzel, "Resistance of solid surfaces to wetting by water," *Industrial & Engineering Chemistry*, vol. 28, no. 8, pp. 988-994, 1936.
- [144] R. M. Silverstein, F. X. Webster, D. J. Kiemle, and D. L. Bryce, *Spectrometric identification of organic compounds*. John Wiley & Sons, 2014.
- [145] Z. Li *et al.*, "Effect of airborne contaminants on the wettability of supported graphene and graphite," *Nature materials*, vol. 12, no. 10, p. 925, 2013.
- [146] P. Liu, L. Cao, W. Zhao, Y. Xia, W. Huang, and Z. Li, "Insights into the superhydrophobicity of metallic surfaces prepared by electrodeposition involving spontaneous adsorption of airborne hydrocarbons," *Applied Surface Science*, vol. 324, pp. 576-583, 2015.
- [147] L. Hu, H. S. Kim, J.-Y. Lee, P. Peumans, and Y. Cui, "Scalable coating and properties of transparent, flexible, silver nanowire electrodes," *ACS nano*, vol. 4, no. 5, pp. 2955-2963, 2010.
- [148] J. Liang, L. Li, X. Niu, Z. Yu, and Q. Pei, "Elastomeric polymer light-emitting devices and displays," *Nature Photonics*, vol. 7, no. 10, pp. 817-824, 2013.
- [149] J. Kim, Y. S. Nam, M. H. Song, H. W. Park, "Large pulsed electron beam welded percolation networks of silver nanowires for transparent and flexible electrodes," *ACS Applied Materials & Interfaces*, vol. 8, pp. 20938-20945, 2016.
- [150] D. A. Porter, K. E. Easterling, and M. Sherif, *Phase Transformations in Metals and Alloys, (Revised Reprint)*. CRC press, 2009.
- [151] P. Scherrer, "Determination of the size and internal structure of colloidal particles using X-rays," *Nachr. Ges. Wiss. Göttingen*, vol. 2, pp. 98-100, 1918.

- [152] L. Wei, Z. Lin-Li, and Z. Xiao-Jing, "Grain size effect on electrical conductivity and giant magnetoresistance of bulk magnetic polycrystals," *Chinese Physics Letters*, vol. 26, no. 11, pp. 117502, 2009.

Acknowledgement

First of all, I would like to appreciate Prof. Hyung Wook Park who was the advisor of my Ph.D course as well as the mentor of my life. Prof. Hyung Wook Park not only taught me how to become a good researcher through academic guidance, but also how to become a little better human being. It was a great luck for me to be able to receive a guidance from Prof. Hyung Wook Park during the last decade of my undergraduate, master's, and doctoral courses. I am confident that I would not have completed this tough course if I had not been in MHM Lab. with my advisor. Regardless of where I will be, what I have learned in my graduate school will help me overcome any types of adversities in the future.

In addition, I would like to thank the committee members, Prof. Myoung Hoon Song, Prof. Namhun Kim, Prof. Hae-Jin Choi, and Prof. Yongho Jeon, who participated in the review of the dissertation from preliminary defense to final defense so that I could bring it to a successful end. Their guidance on my dissertation greatly improved the quality of it.

I sincerely thank members of MHM Lab. The footsteps of seniors, Dr. Eunju Park, Dr. Kyungil Kong, Dr. Dong Min Kim, and Mr. Hyun-Myung Kim, who have graduated now are a perfect guide for following juniors. I especially thank Dr. Dong Min Kim being with me in every hard times of my life.

I also thank my friends. Thank you to all the members of "Earthcops", the football club that was one of majorities of my school life. Besides playing soccer, the members were strong supporters who stood by me in various research fields. I would like to express my gratitude to Dr. Minsu Gu who reviewed and revised my research like his own work.

I would like to say thank you to my friends, Jae-Wu Seo, Kyubo Shin, Jaehyung Hong, Hansol Kim, Yun Suk Nam, and Won Bae Kim, who were good friends both in joy and in sorrow while studying at the graduate school. I think they are probably the most valuable achievement I have gained in my degree.

I would also like to thank all the members of the various institutes, companies, and schools that have participated in my research.

Most importantly, I would like to tell my parents and sister that I love you. They were the most powerful supporters for my life and I could finish my course thanks to their dedicated efforts. In particular, I will pay my life to my parents who have inherited my legacy of precious patience more than any other heritage.

Someone said that people achieve master's degree when they realize "I did not know anything", and achieve doctoral degree when they realize "Others also do not know what I do not know". I will try hard to be a researcher who can be a pioneer in the field that everyone does not know.

